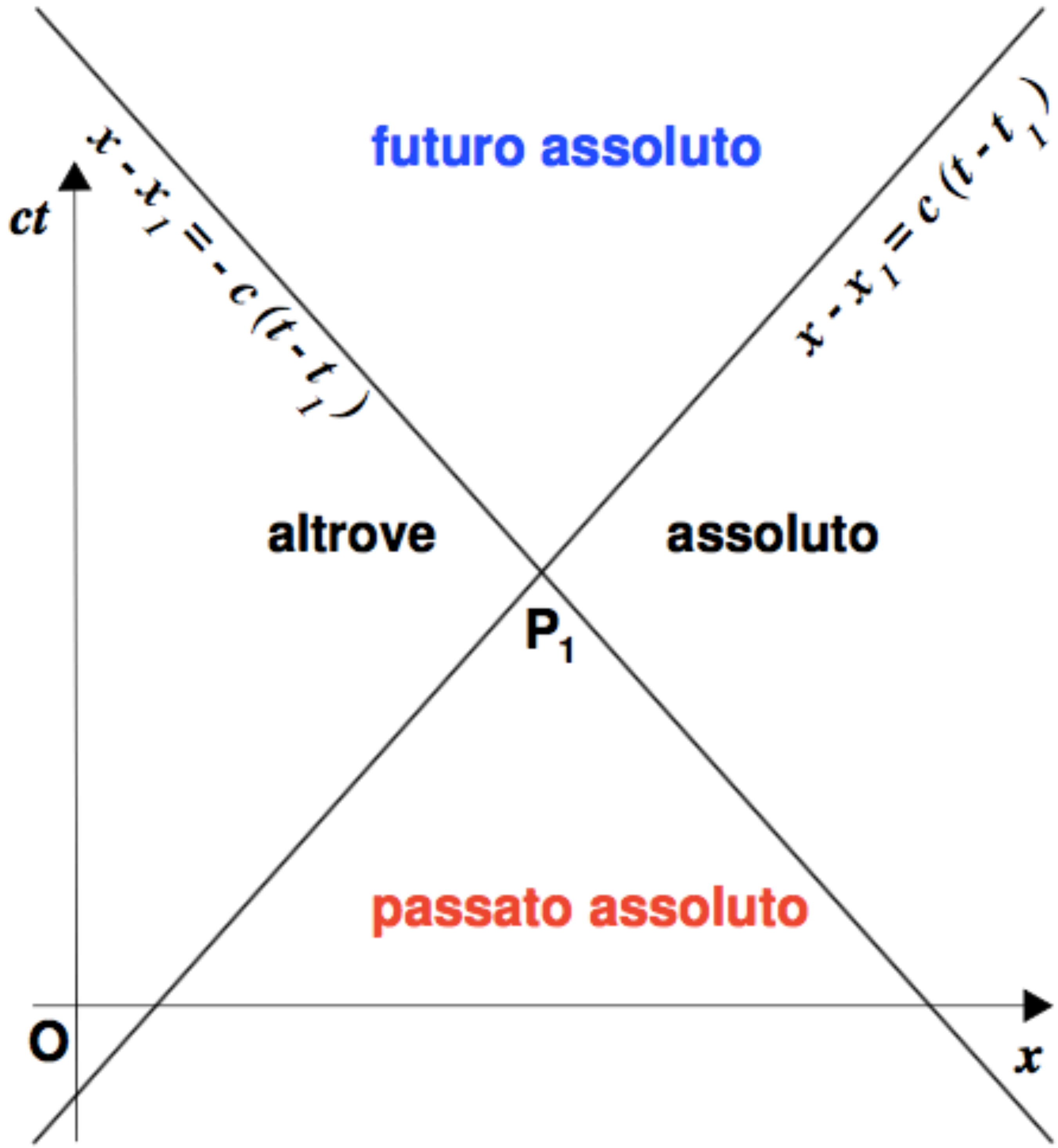

Figura 1.1: Lo spazio-tempo relativamente all'evento P_1.

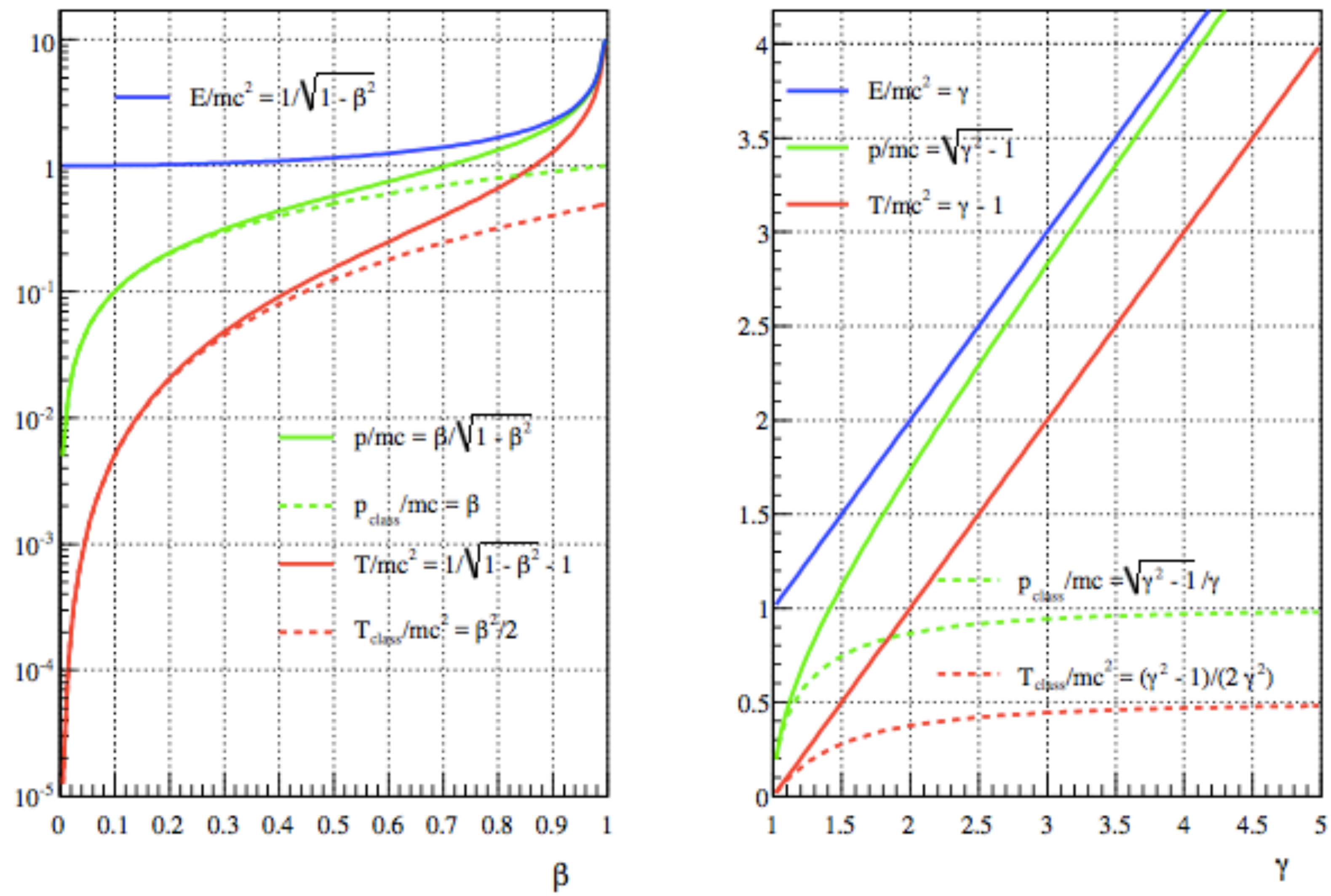

Figura 1.2: L'energia totale, l'energia cinetica e l'impulso come finzioni di β e γ. Anche i limiti classici ($\beta \to 0$) sono mostrati in figura.

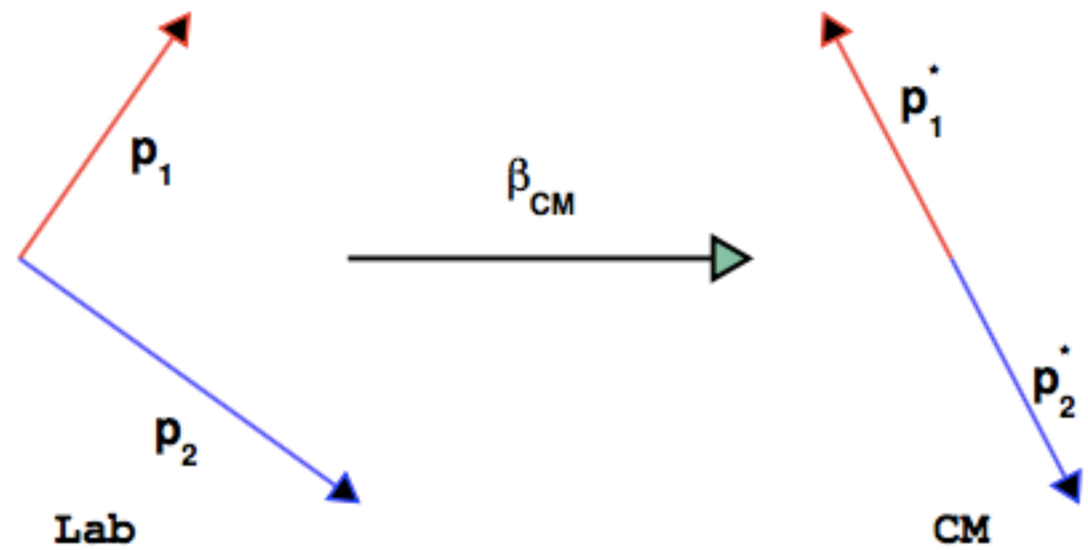

Figura 1.3: Illustrazione della trasformazione dal **Lab** al **CM**.

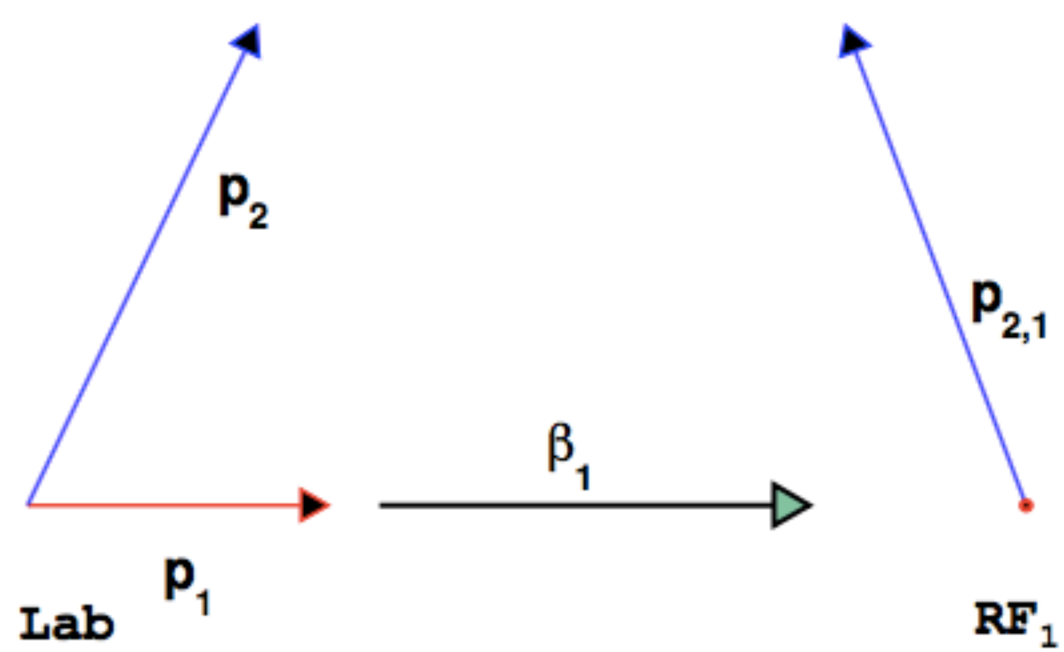

Figura 1.4: Trasformazione dal **Lab** al sistema di riposo della particella 1 $\mathbf{RF}_1$.

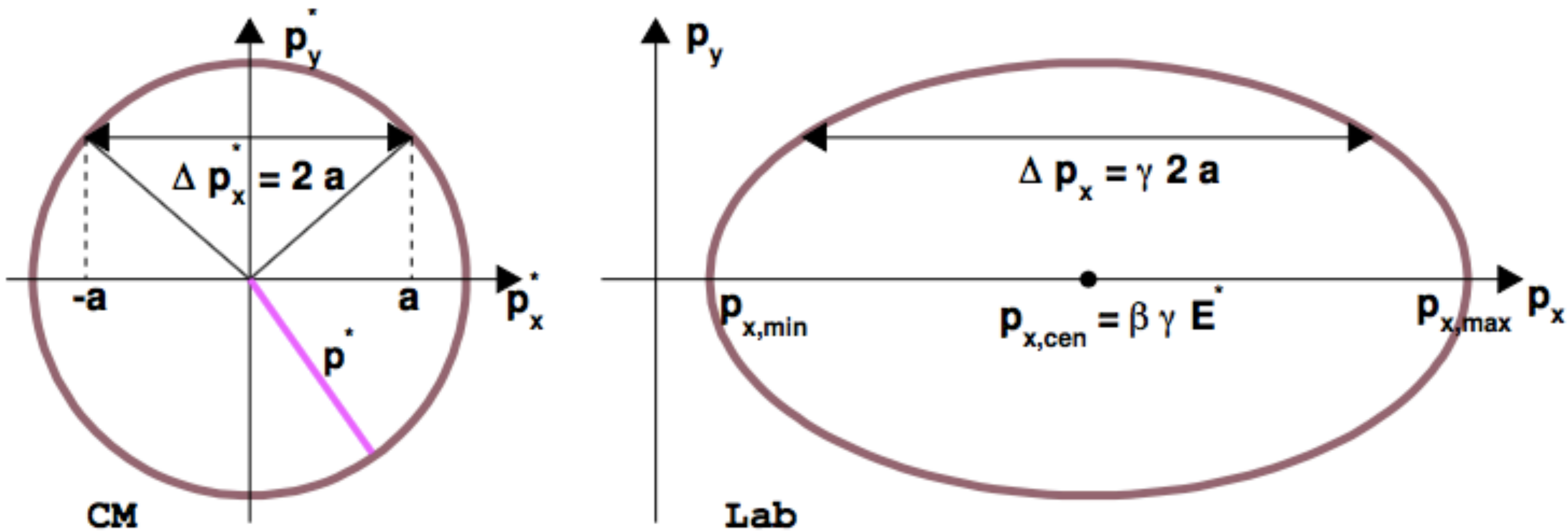

Figura 1.5: Trasformazione degli impulsi dal **CM** al **Lab**.

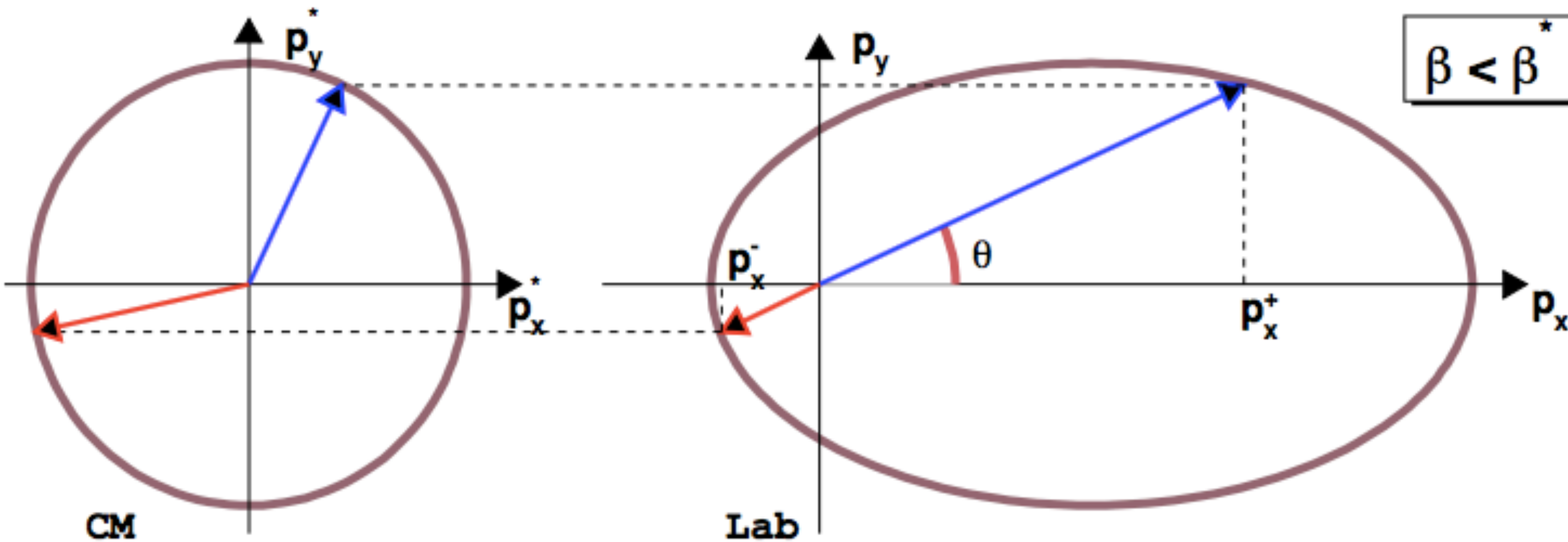

Figura 1.6: Trasformazione degli impulsi dal **CM** al **Lab**. Caso $\beta < \beta^*$.

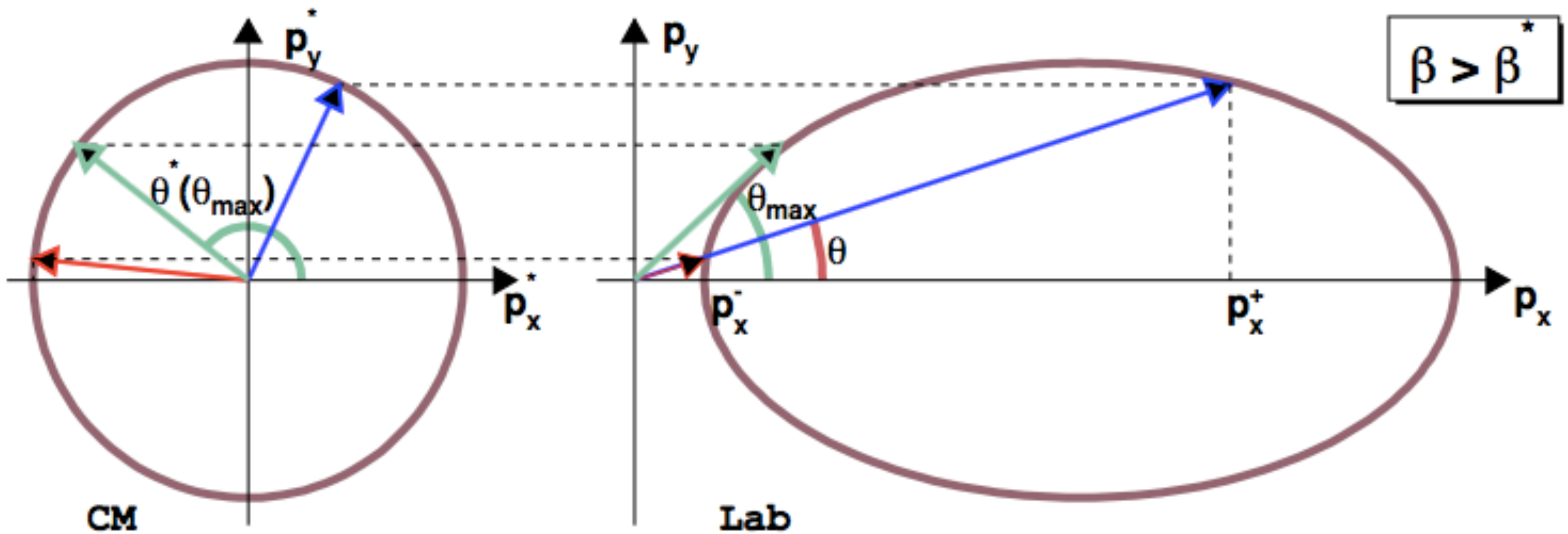

Figura 1.7: Trasformazione degli impulsi dal **CM** al **Lab**. Caso $\beta > \beta^*$. Si noti l'angolo limite θ_{max} nel **Lab**.

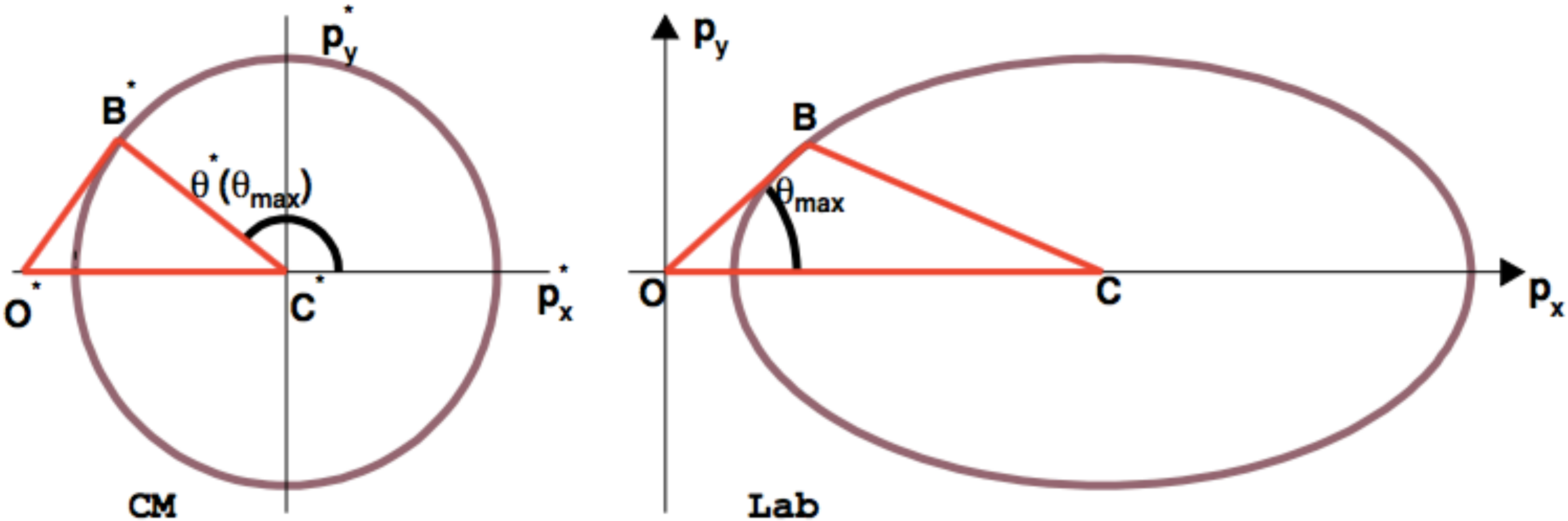

Figura 1.8: Corrispondenza tra **CM** e **Lab** nel calcolo di $\theta^*(\theta_{max})$ con il metodo delle ellissi.

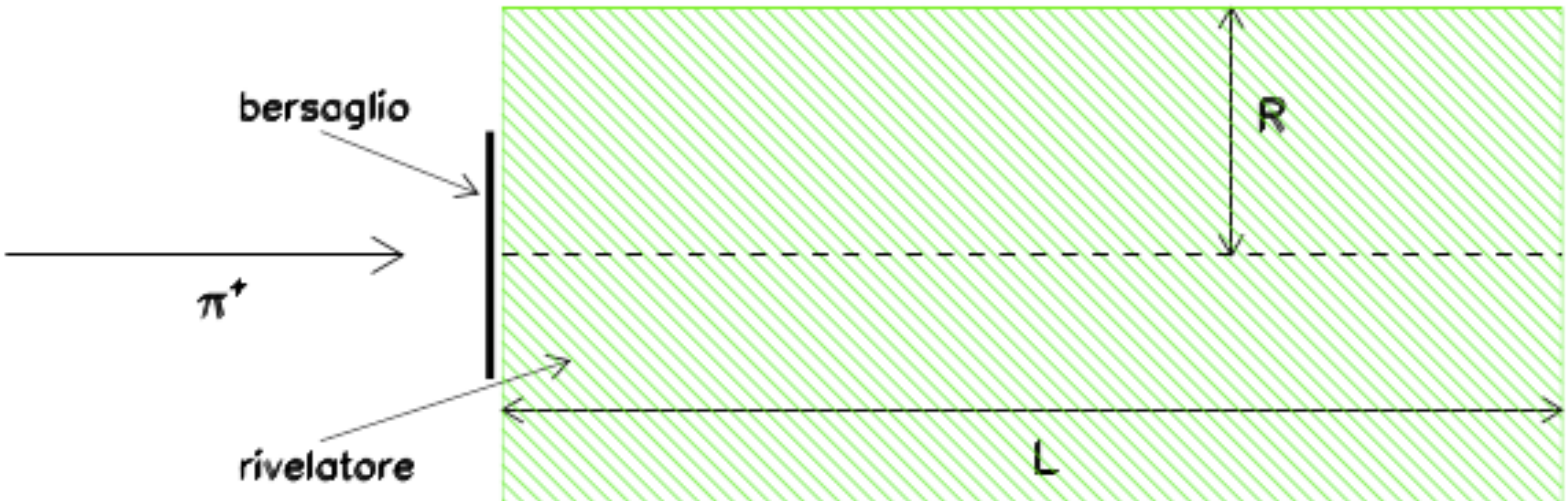
bersaglio
R
π+
rivelatore
L

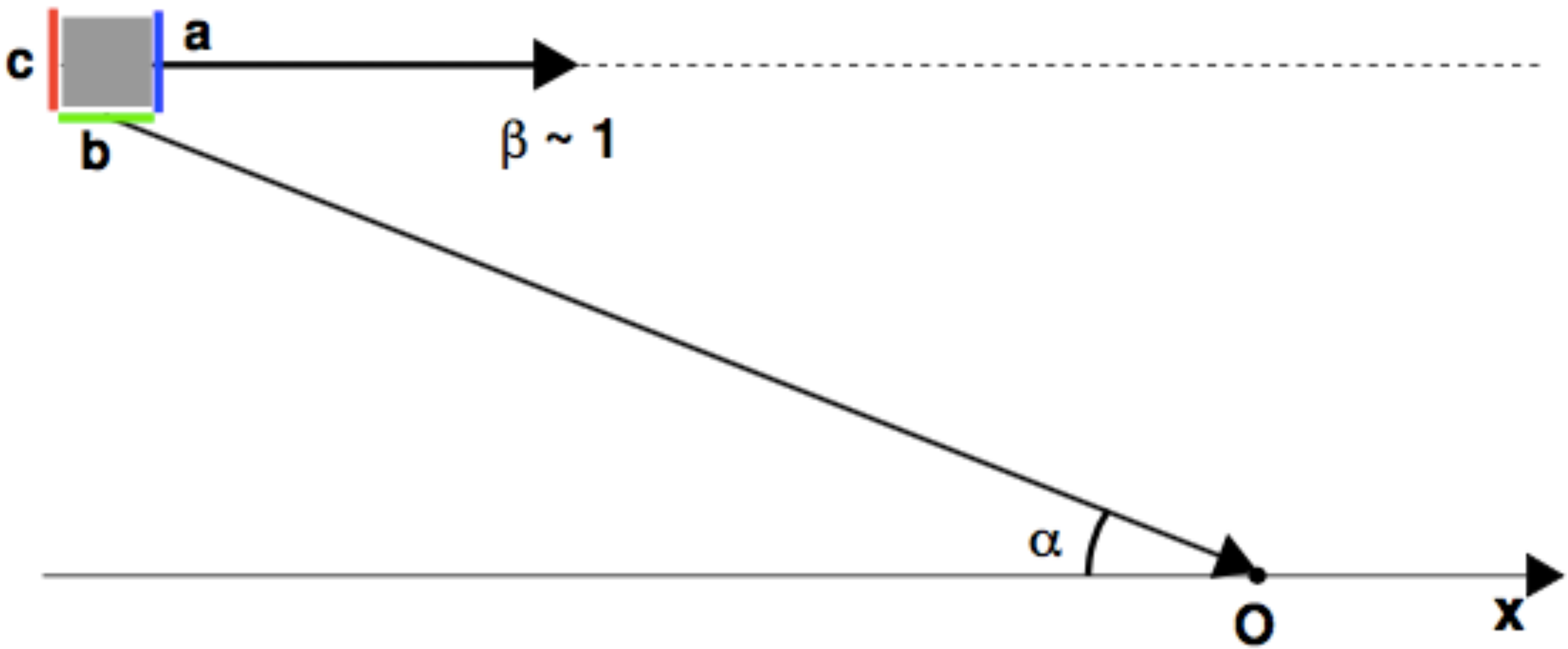

Figura 1.9: Oggetto in movimento veloce. α è l'angolo di vista.

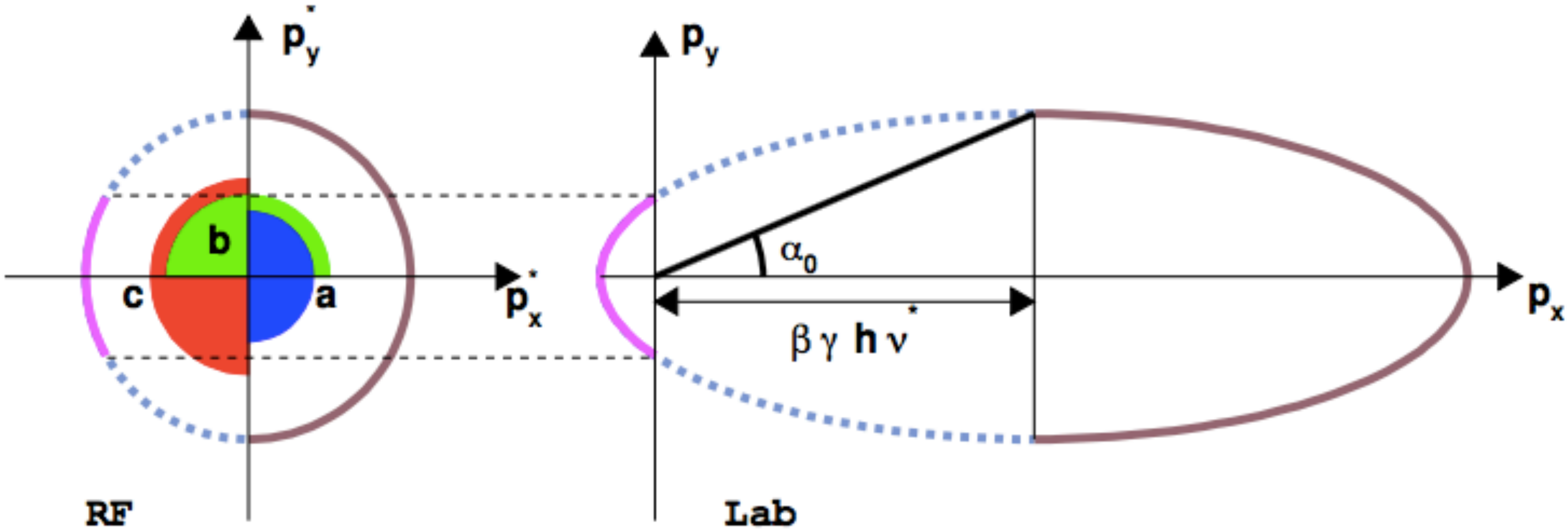

Figura 1.10: Metodo delle ellissi applicato al caso dell'oggetto in movimento veloce.

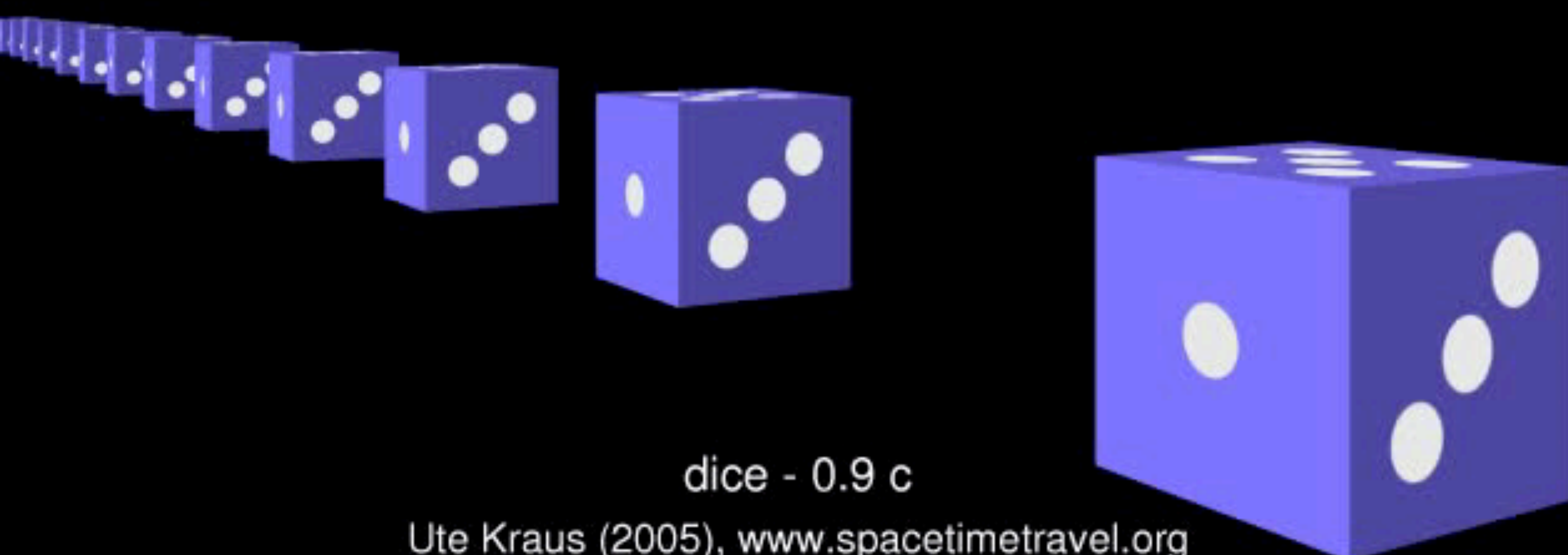

dice - 0.9 c

Ute Kraus (2005), www.spacetimetravel.org

Perdita di energia per Ionizzazione

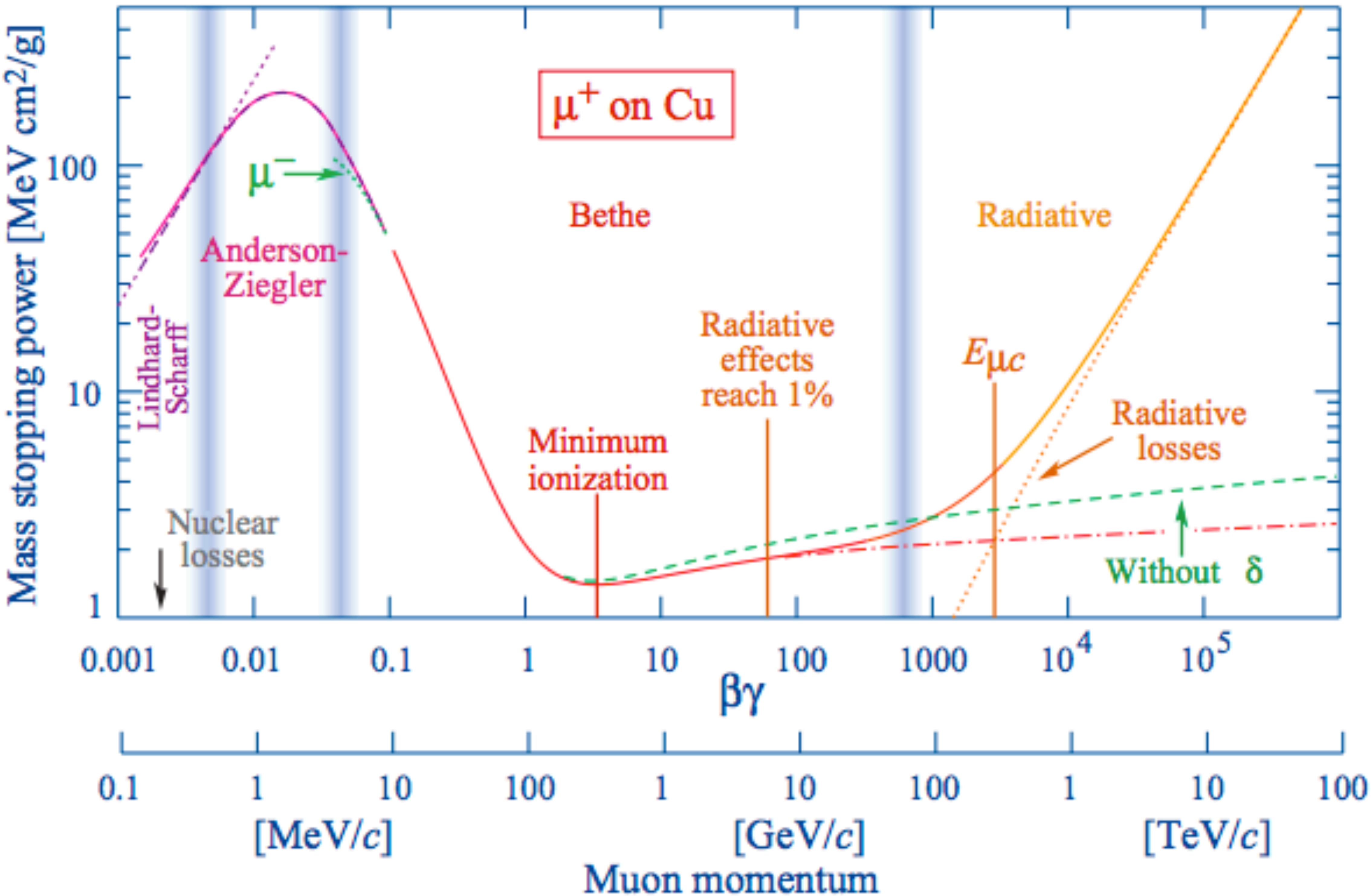

Perdita di energia per Ionizzazione

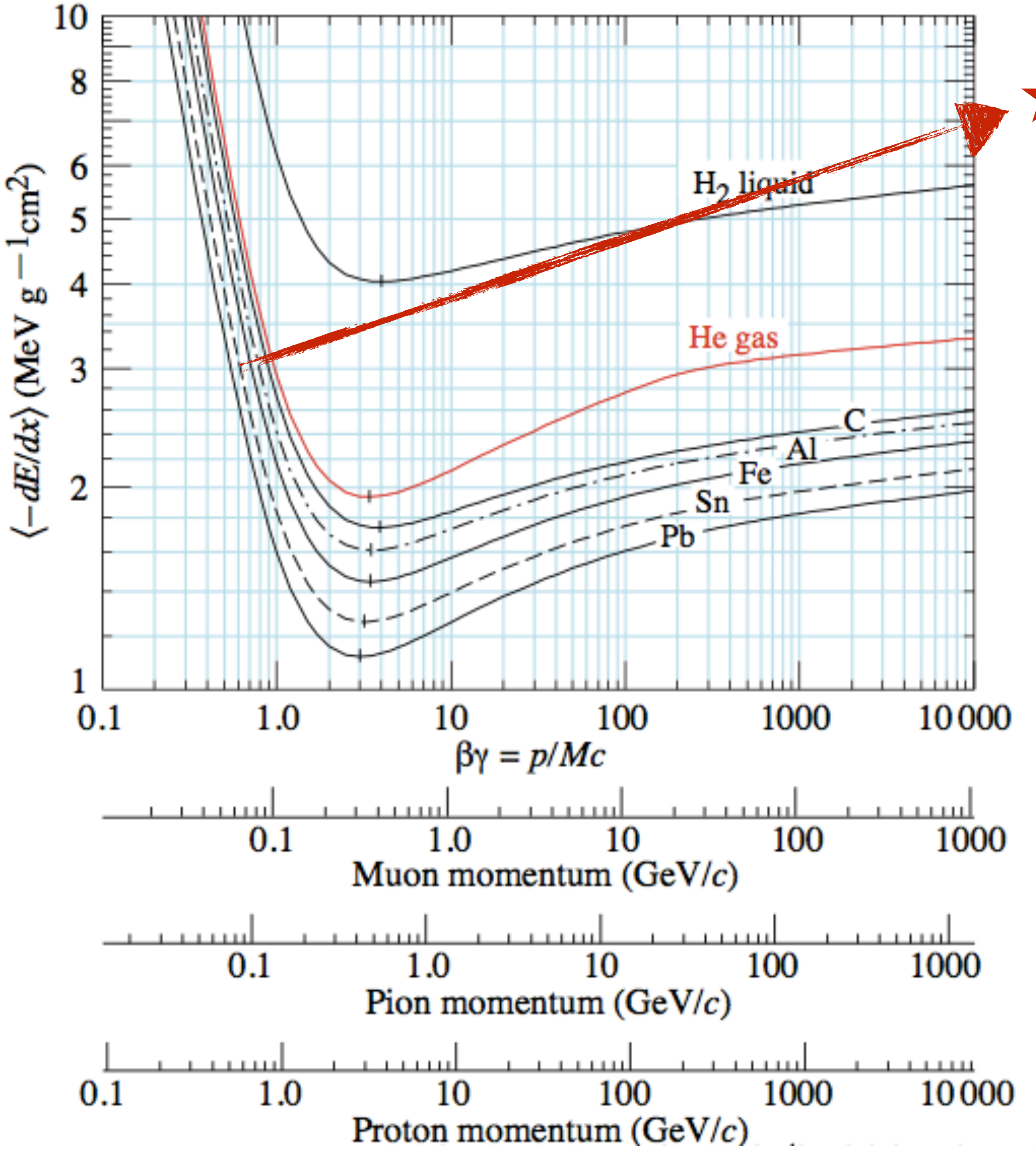

★ A bassi $\beta\gamma$ la perdita di energia decresce andamento come $1/\beta^2$

Perdita di energia per Ionizzazione

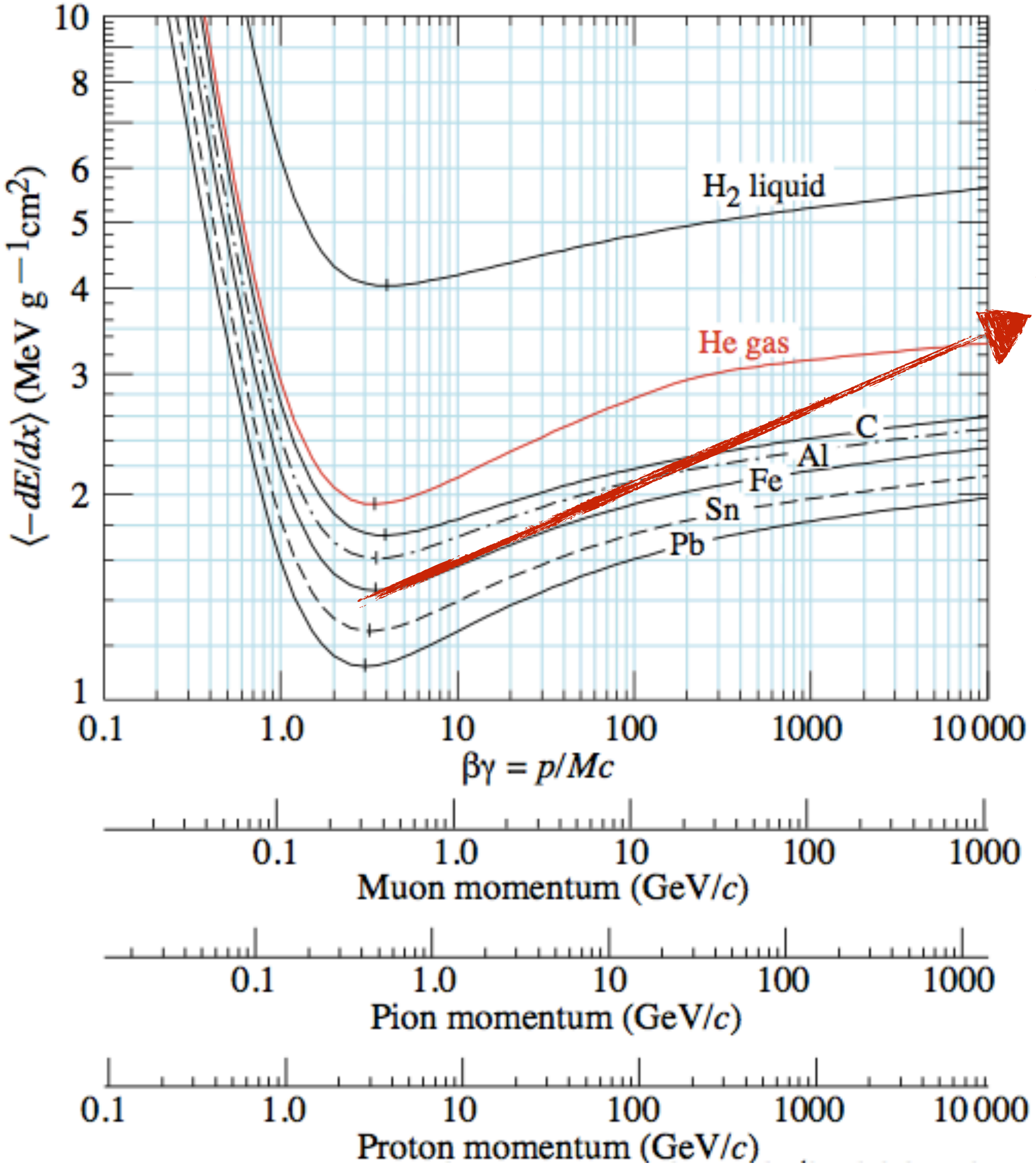

- ★ A bassi $\beta\gamma$ la perdita di energia decresce andamento come $1/\beta^2$
- ★ Si ha un minimo per $3<\beta\gamma<4$ e varia poco con il materiale 1-2 MeV/(g/cm^2)

Perdita di energia per Ionizzazione

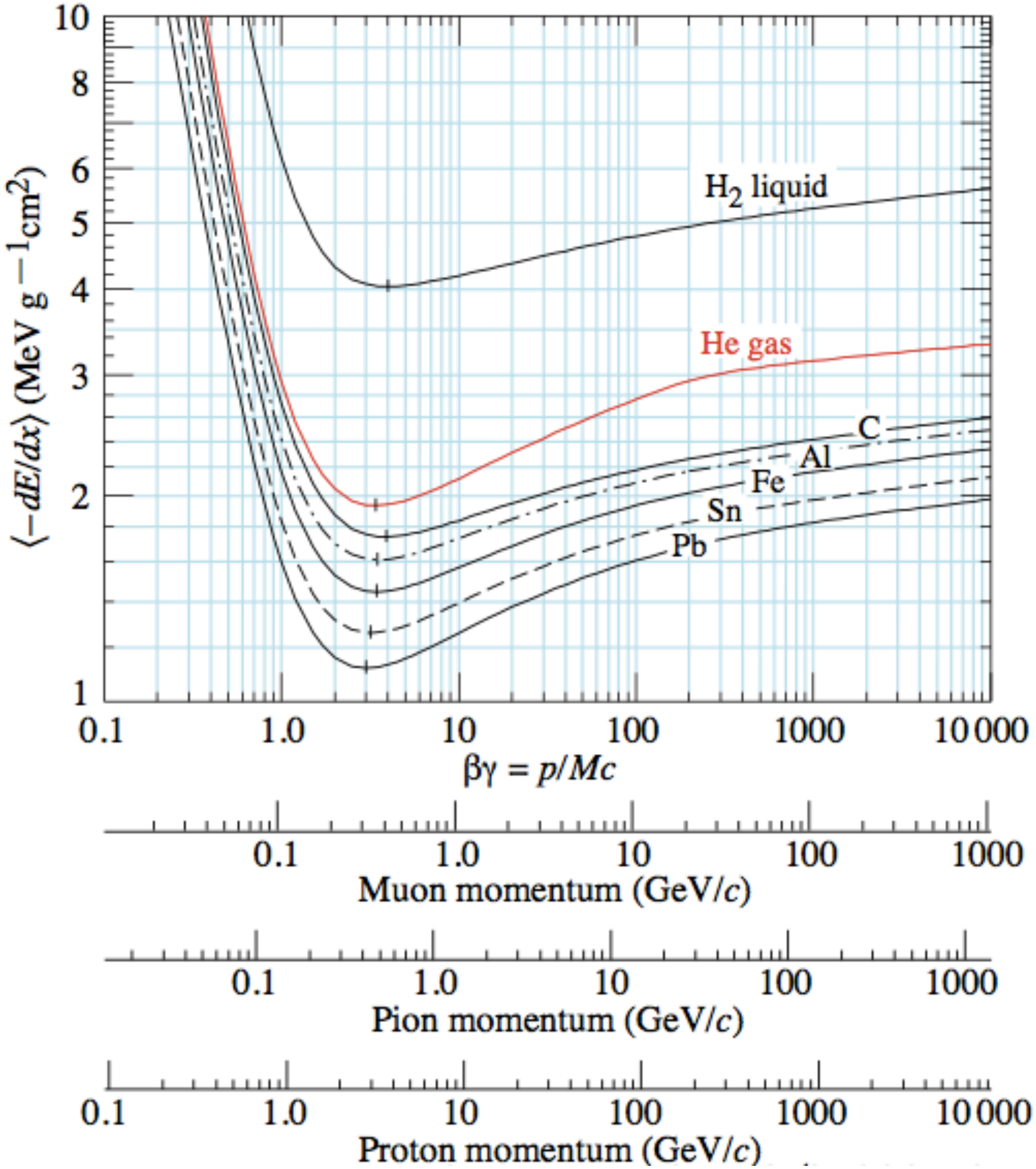

- A bassi $\beta\gamma$ la perdita di energia decresce andamento come $1/\beta^2$
- Si ha un minimo per $3<\beta\gamma<4$ e varia poco con il materiale 1-2 MeV/(g/cm^2)
- L'effetto Z/A presente nella formula si vede nella spaziatura delle varie curve

H_2 -> Z/A = 1 Emin =4
C -> Z/A = 0.5 Emin = 1.8
<u>circa un fattore 2</u>

Perdita di energia per Ionizzazione

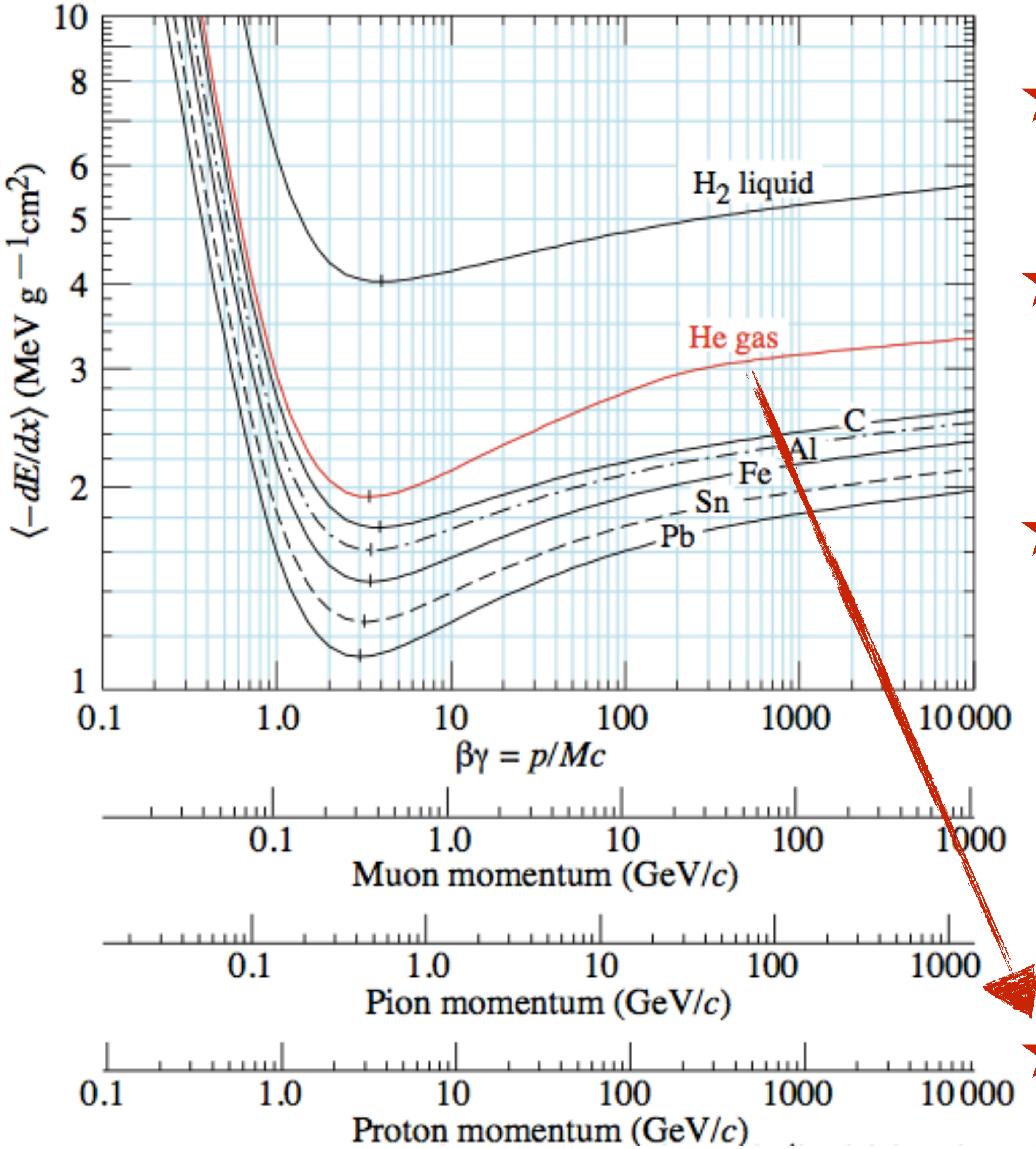

- A bassi $\beta\gamma$ la perdita di energia decresce andamento come $1/\beta^2$
- Si ha un minimo per $3<\beta\gamma<4$ e varia poco con il materiale 1-2 MeV/(g/cm^2)
- L'effetto Z/A presente nella formula si vede nella spaziatura delle varie curve

H_2 -> Z/A = 1 Emin =4
C -> Z/A = 0.5 Emin = 1.8
<u>circa un fattore 2</u>

- effetto di saturazione ad alte energie, diverso per i gas

Fluttuazioni nella perdita di energia per Ionizzazione

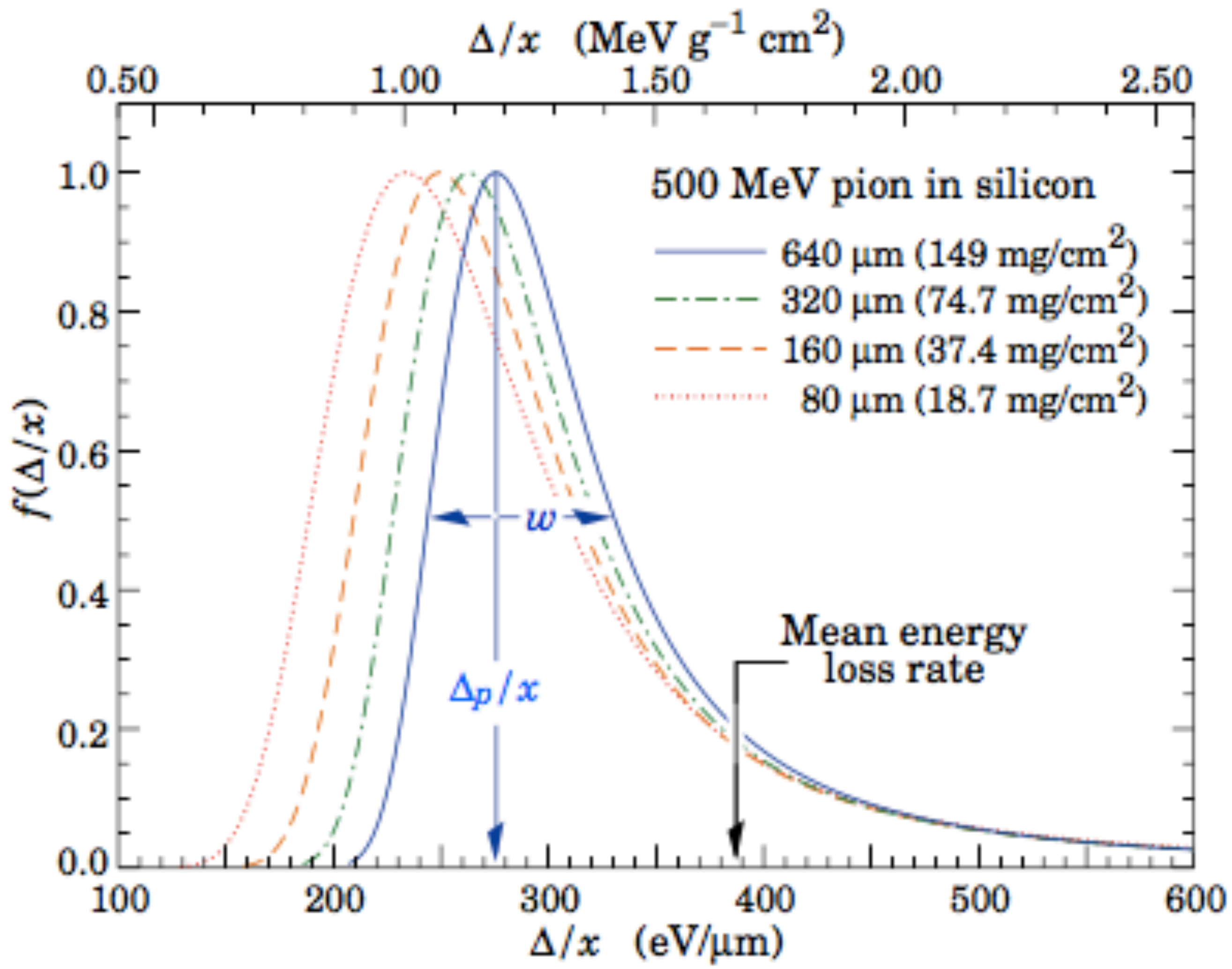

Figure 1.44: Distribuzione del rapporto Δ/x in diversi spessori di Silicio (S.Eidelman *et al.*, Physics Letters B592, 1, 2004)

Fluttuazioni nella perdita di energia per Ionizzazione

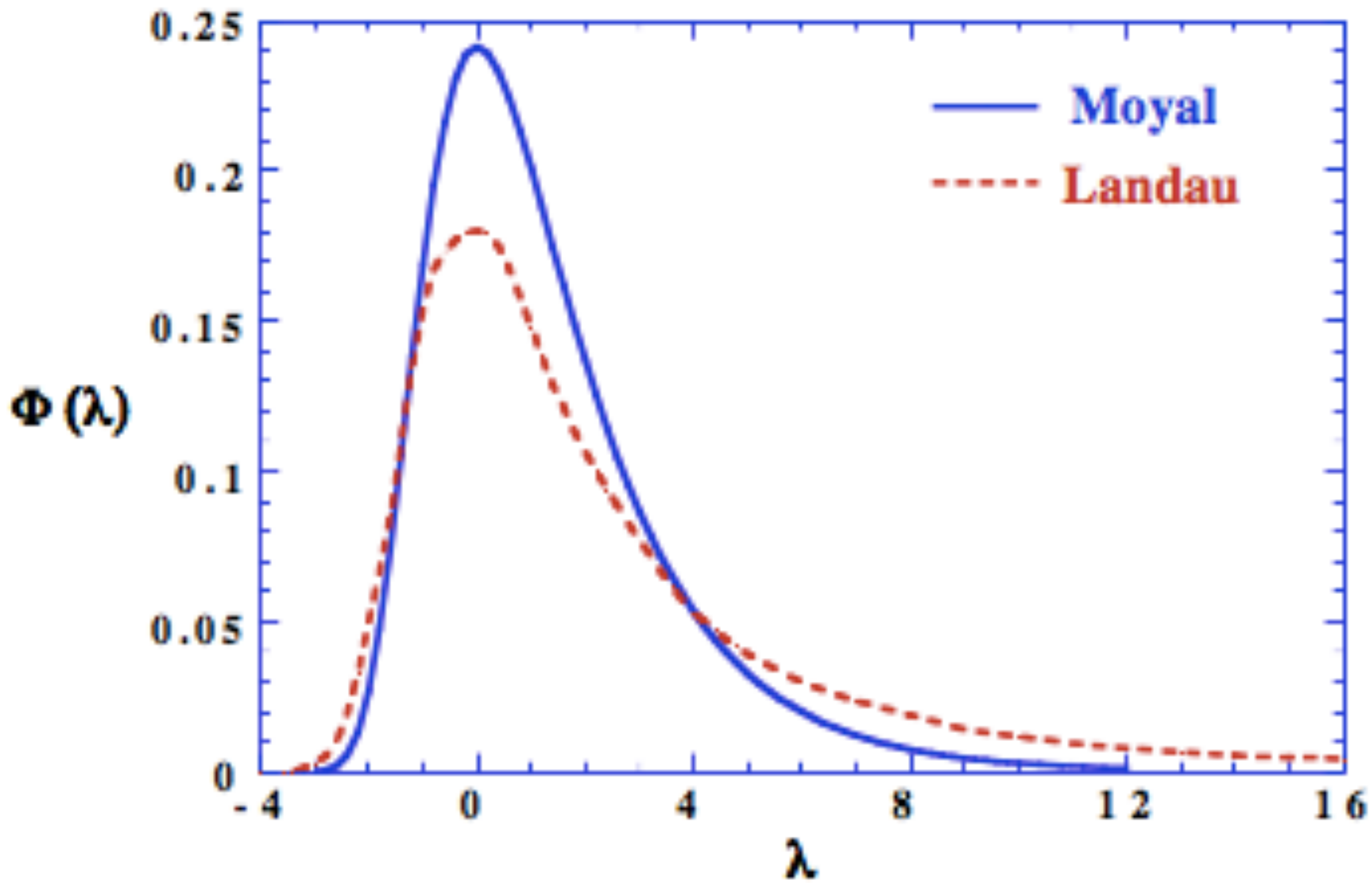

Figure 1.45: Distribuzioni di Landau e di Moyal

Range

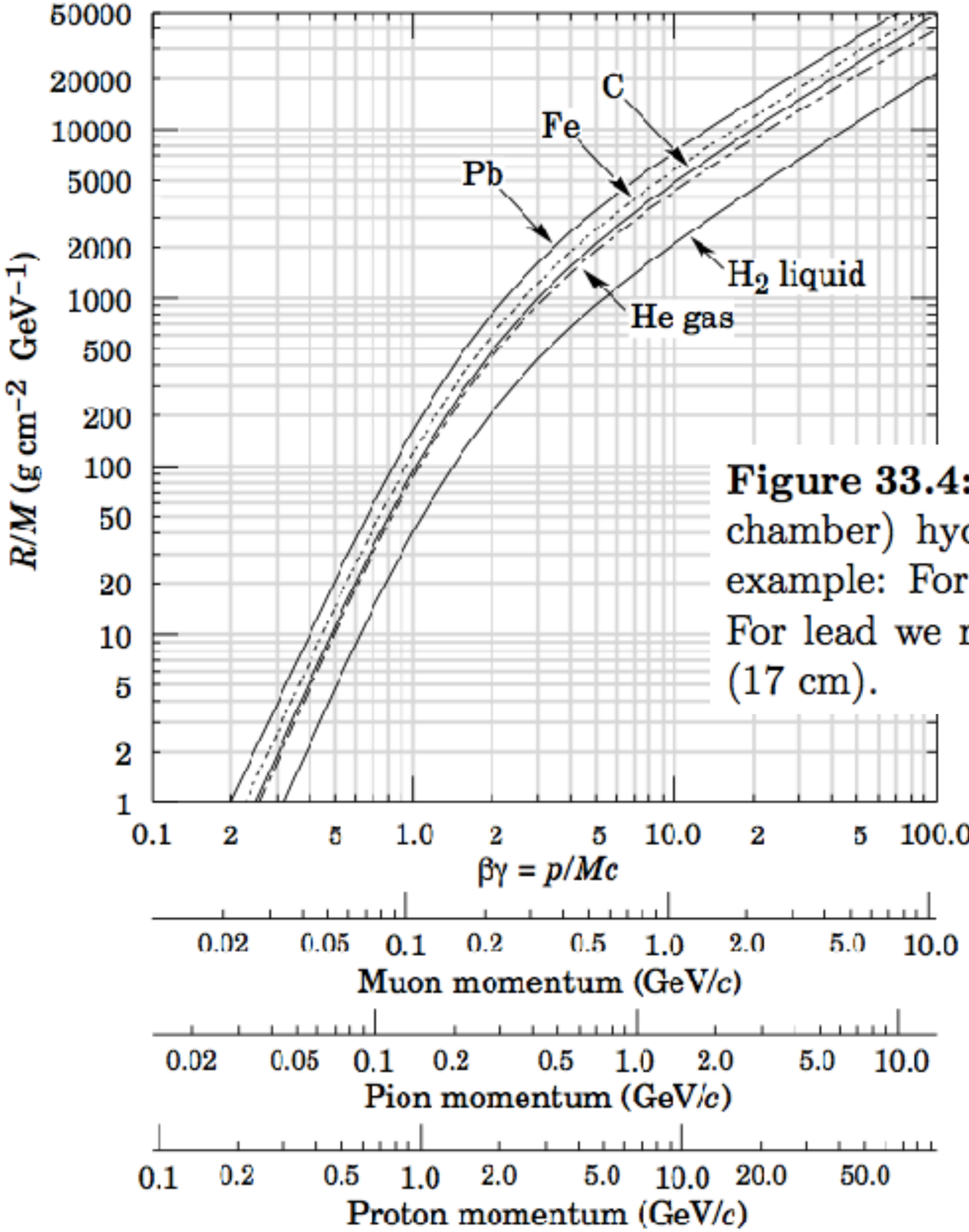

Figure 33.4: Range of heavy charged particles in liquid (bubble chamber) hydrogen, helium gas, carbon, iron, and lead. For example: For a K^+ whose momentum is 700 MeV/c, $\beta\gamma = 1.42$. For lead we read $R/M \approx 396$, and so the range is 195 g cm^{-2} (17 cm).

Radiazione Čerenkov

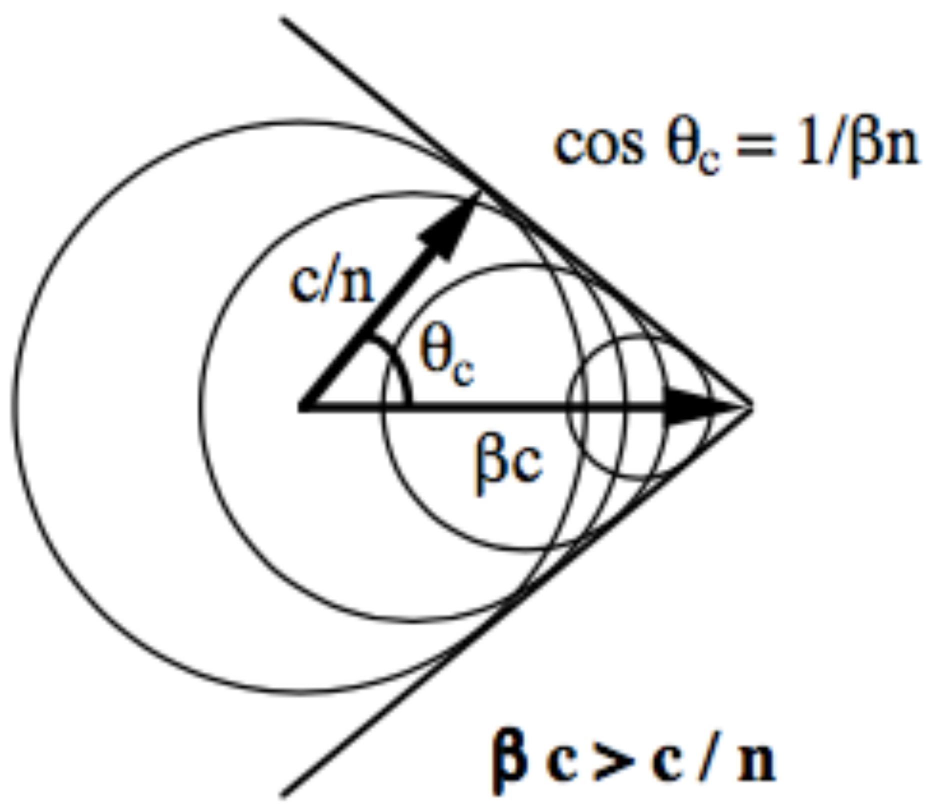

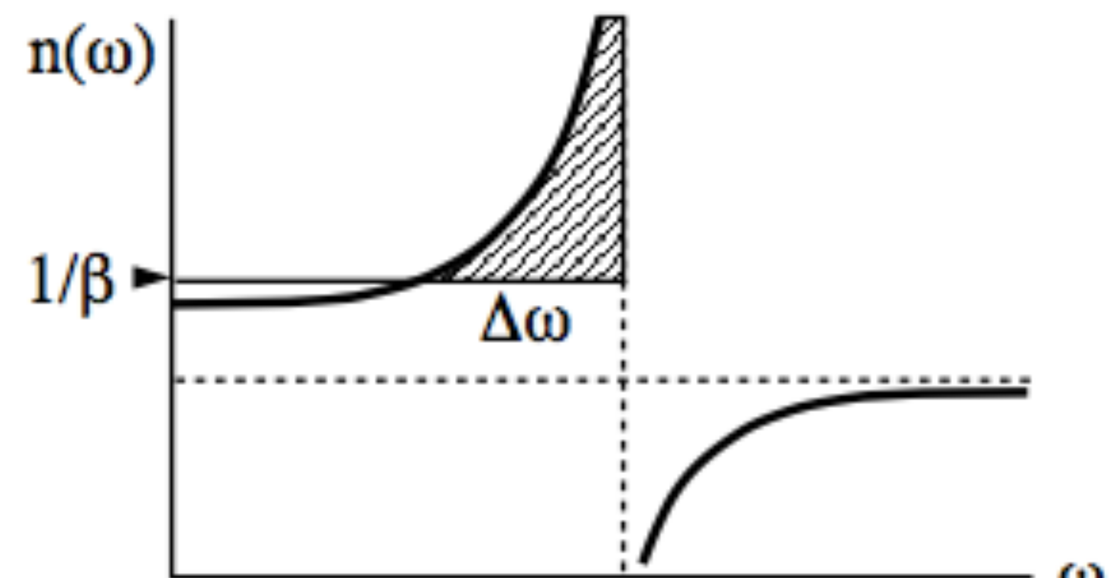

Figure 1.47: Effetto Čerenkov

Radiazione Čerenkov

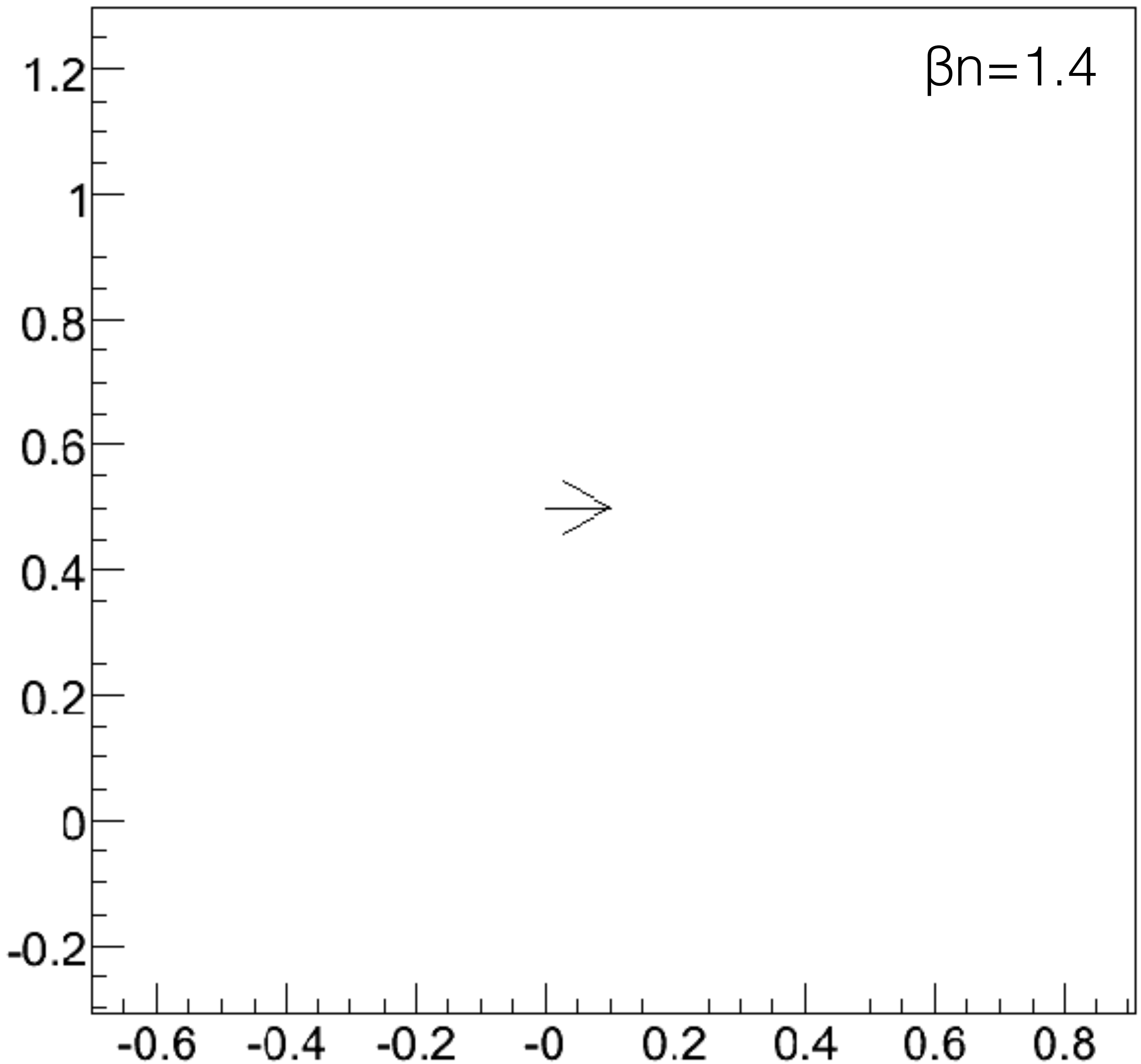

SilEye experiment

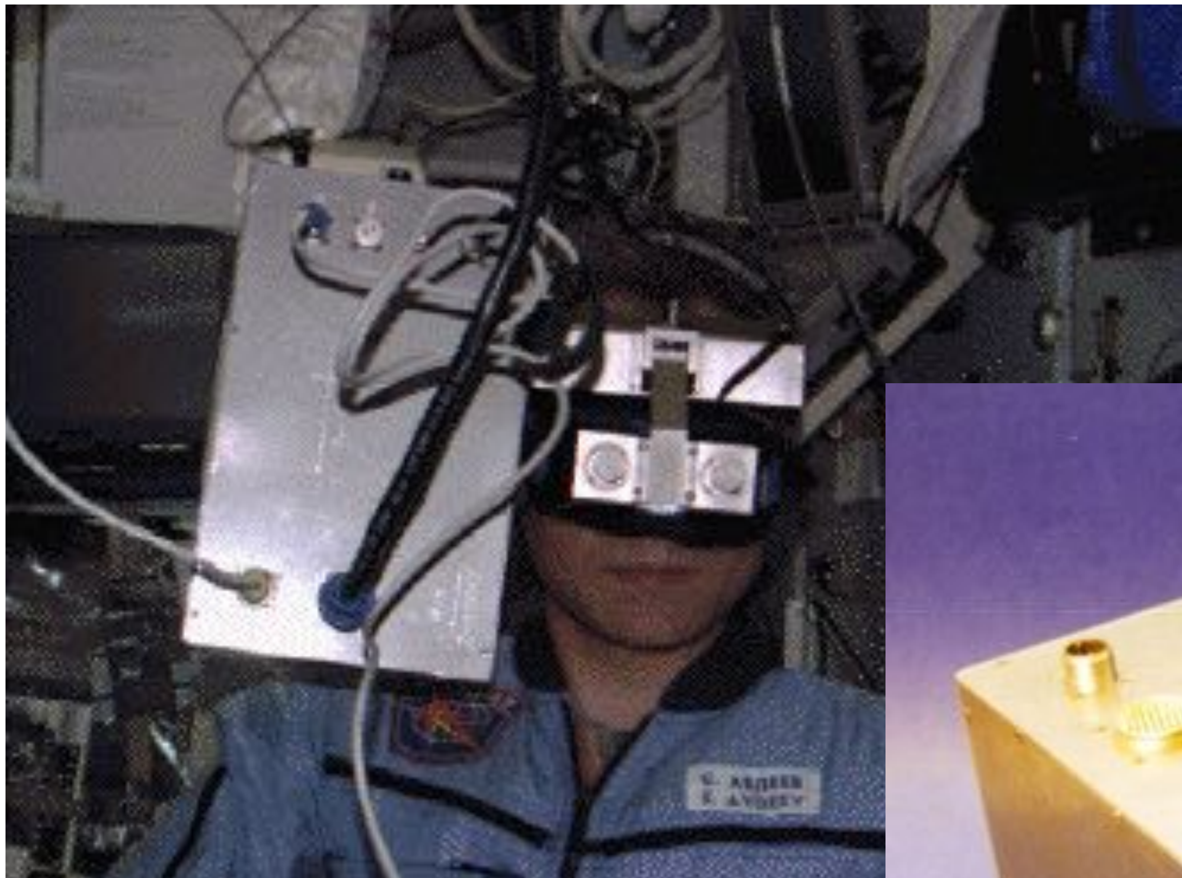

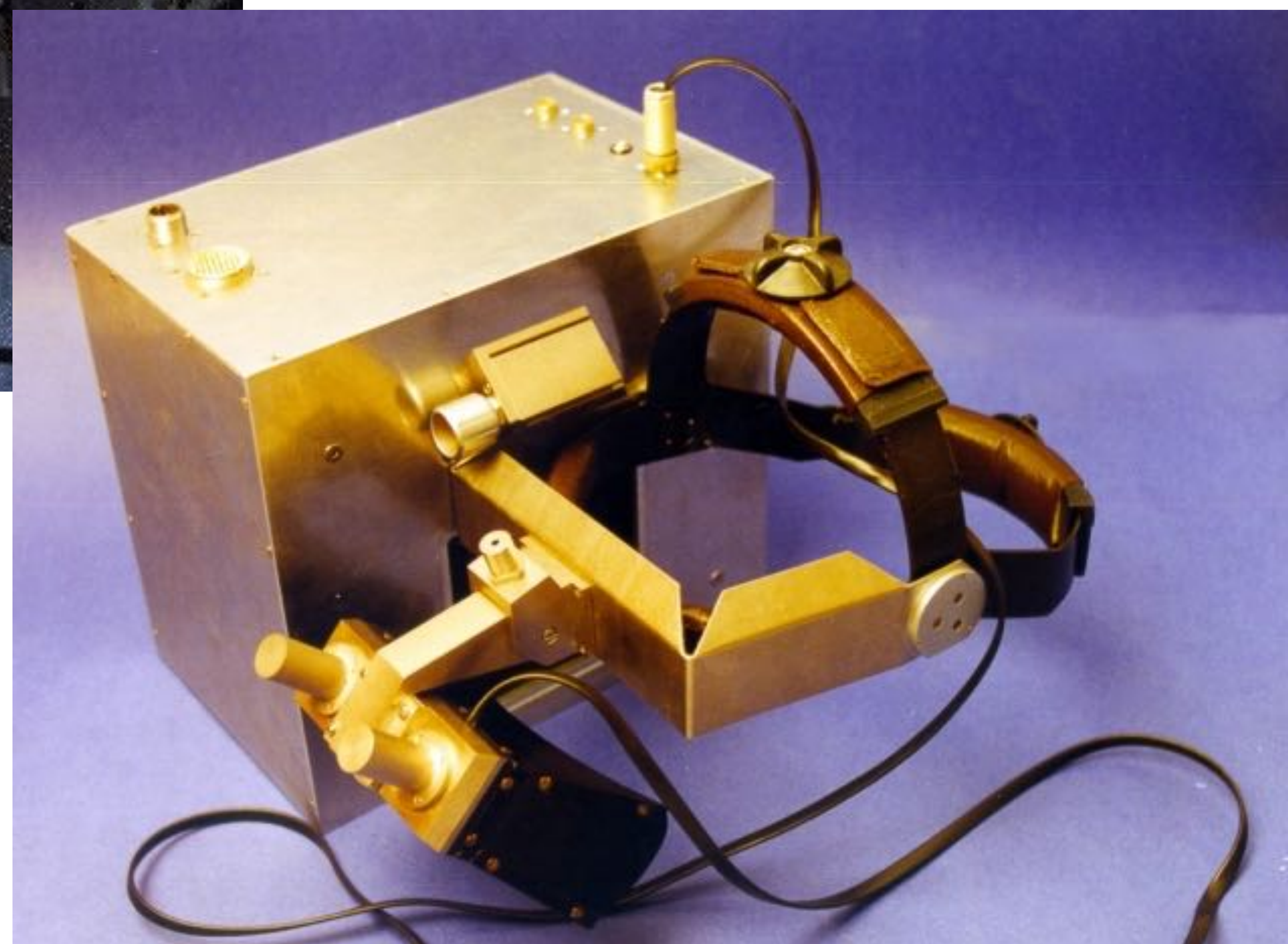

Diffusione Coulombiana multipla

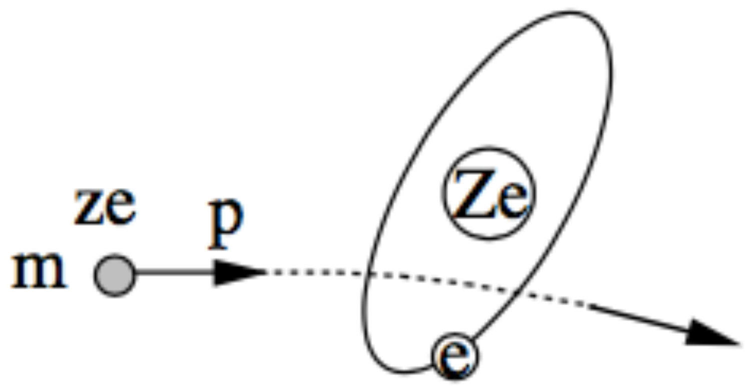

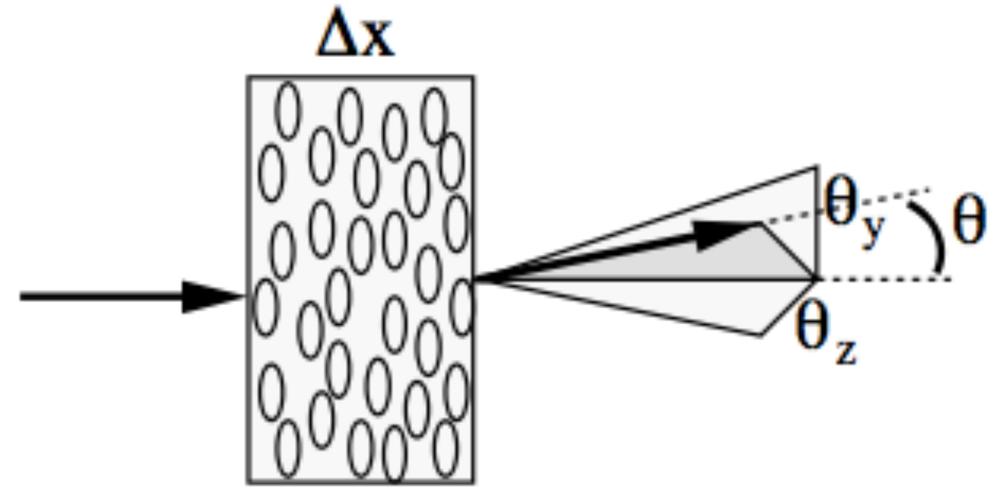

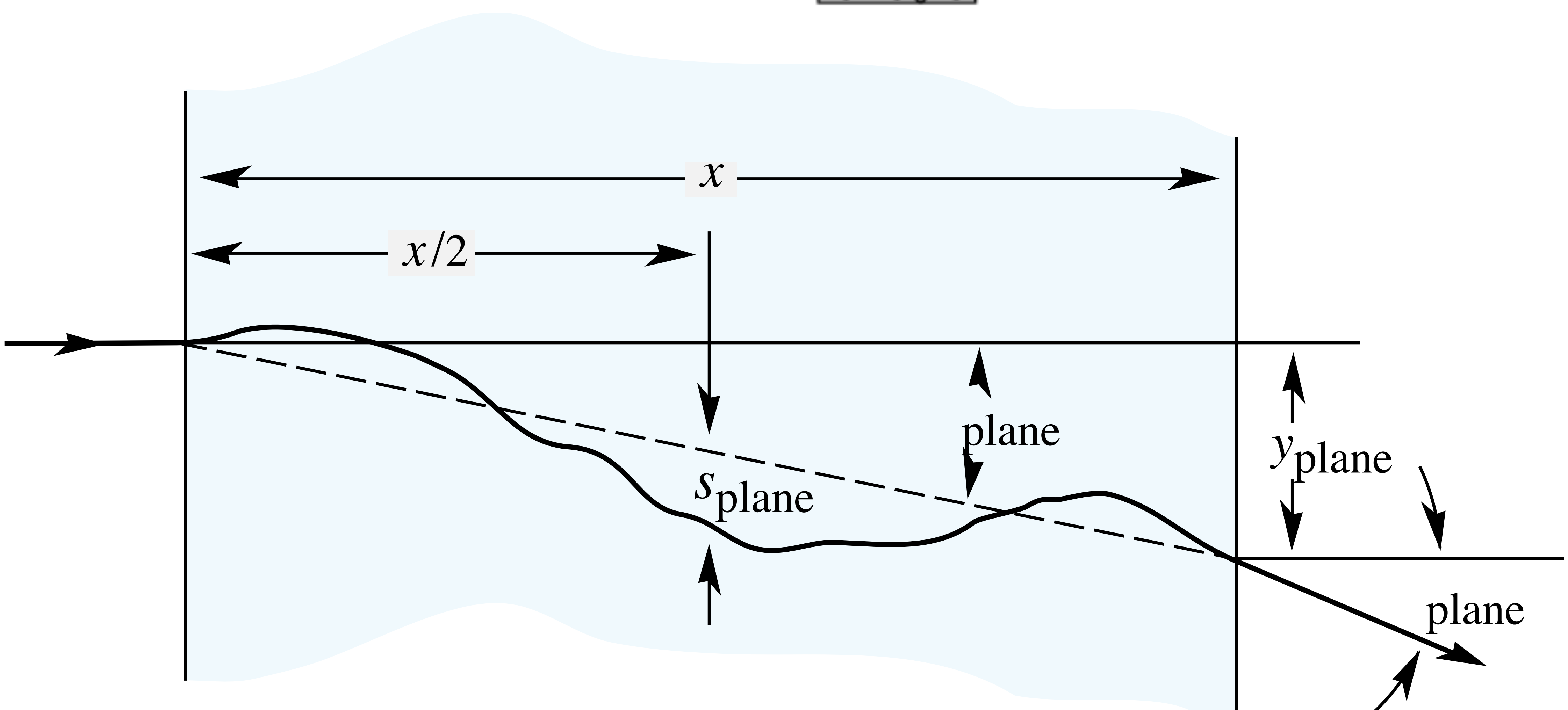

Irraggiamento - Bremsstrahlung

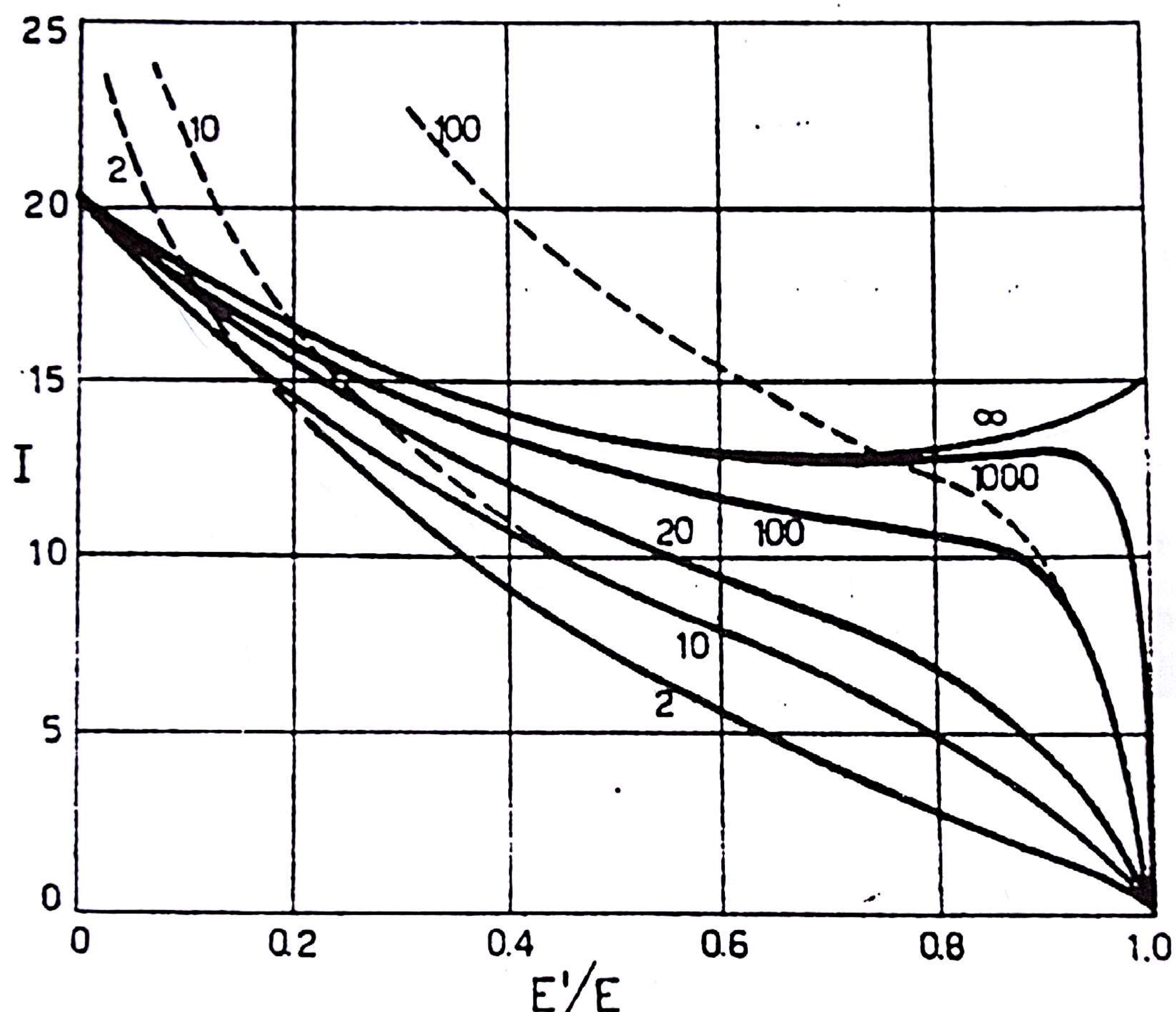

Fig.9 – Distribuzione in energia dei fotoni irraggiati, per cammino di radiazione, da un elettrone avente l'energia indicata, con un numero che la esprime in unità $mc^2 = 0{,}511$ MeV, accanto a ciascuna curva. Le curve a tratto continuo tengono conto dell'effetto di schermo; quelle tratteggiate non includono invece la correzione per tale effetto che, come si vede, è tanto più importante quanto maggiore è l'energia E dell'elettrone e quanto più piccola è la frazione E'/E di energia irraggiata. [cfr. (Be 34)].

Irraggiamento - Bremsstrahlung

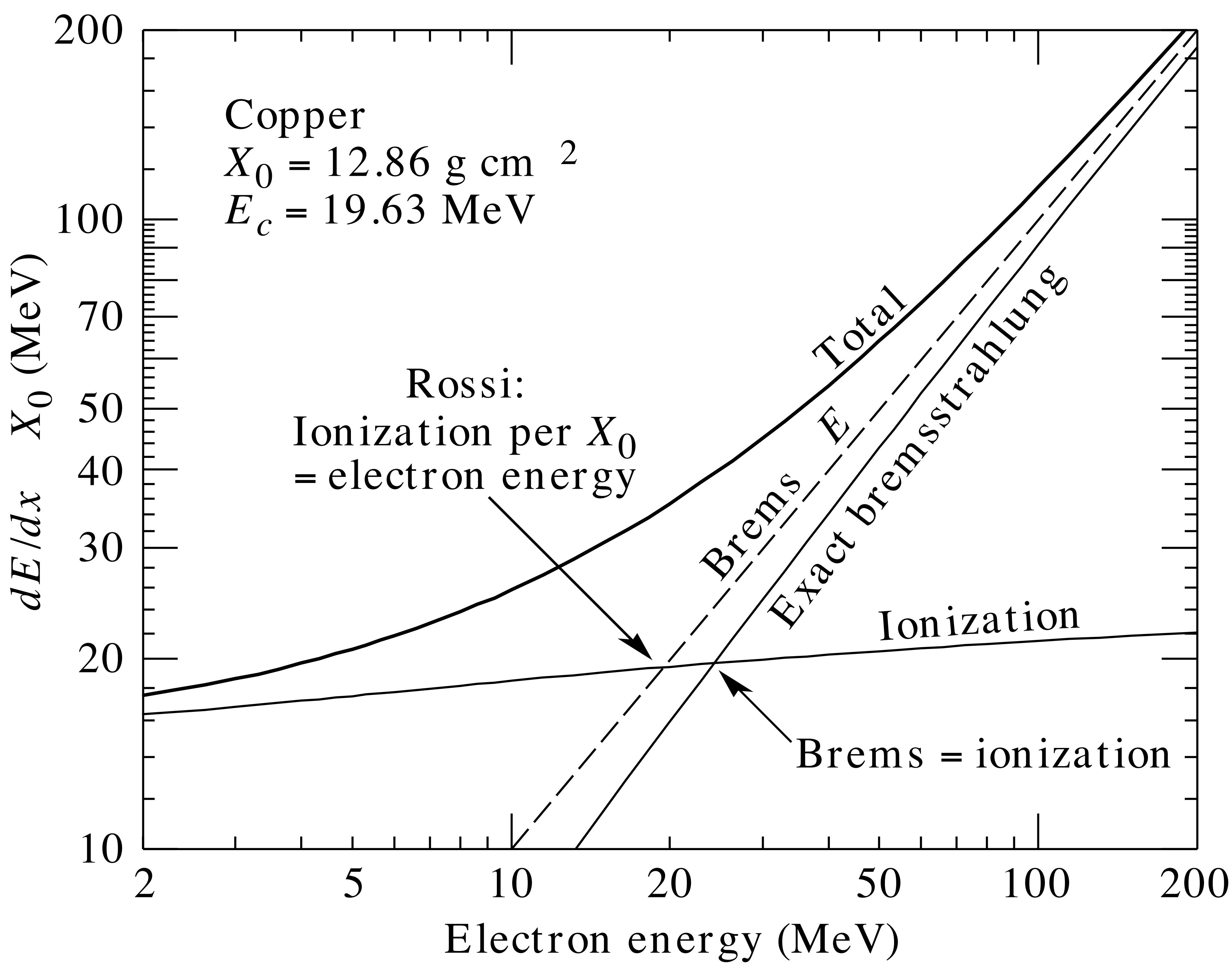

Produzione di coppie

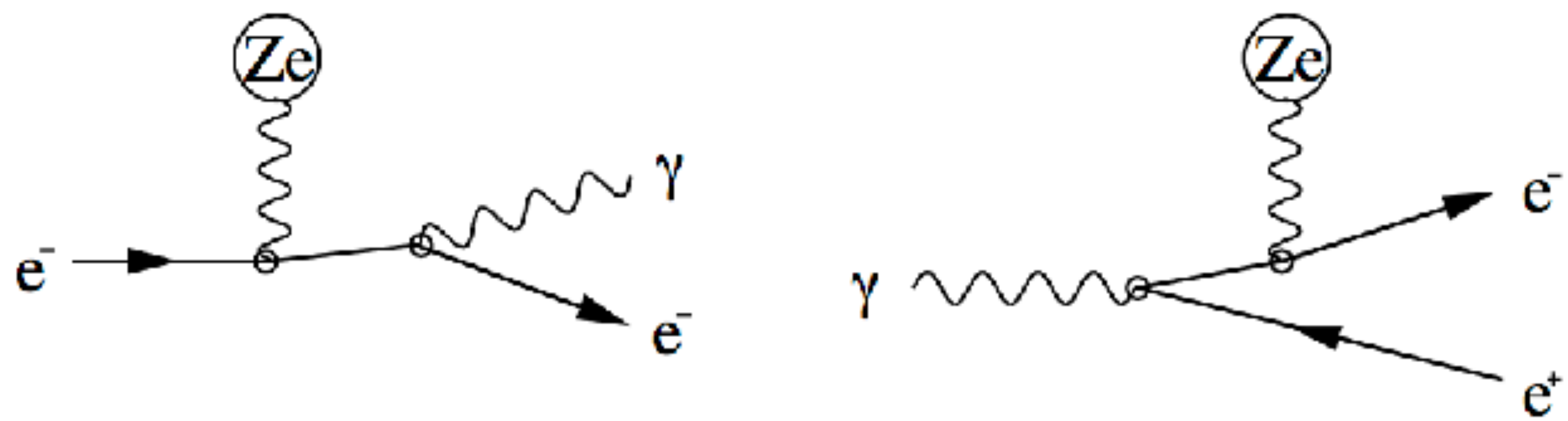

Figure 1.51: Irraggiamento e produzione di coppie elettrone-positrone nel campo di un nucleo

Interazione dei fotoni

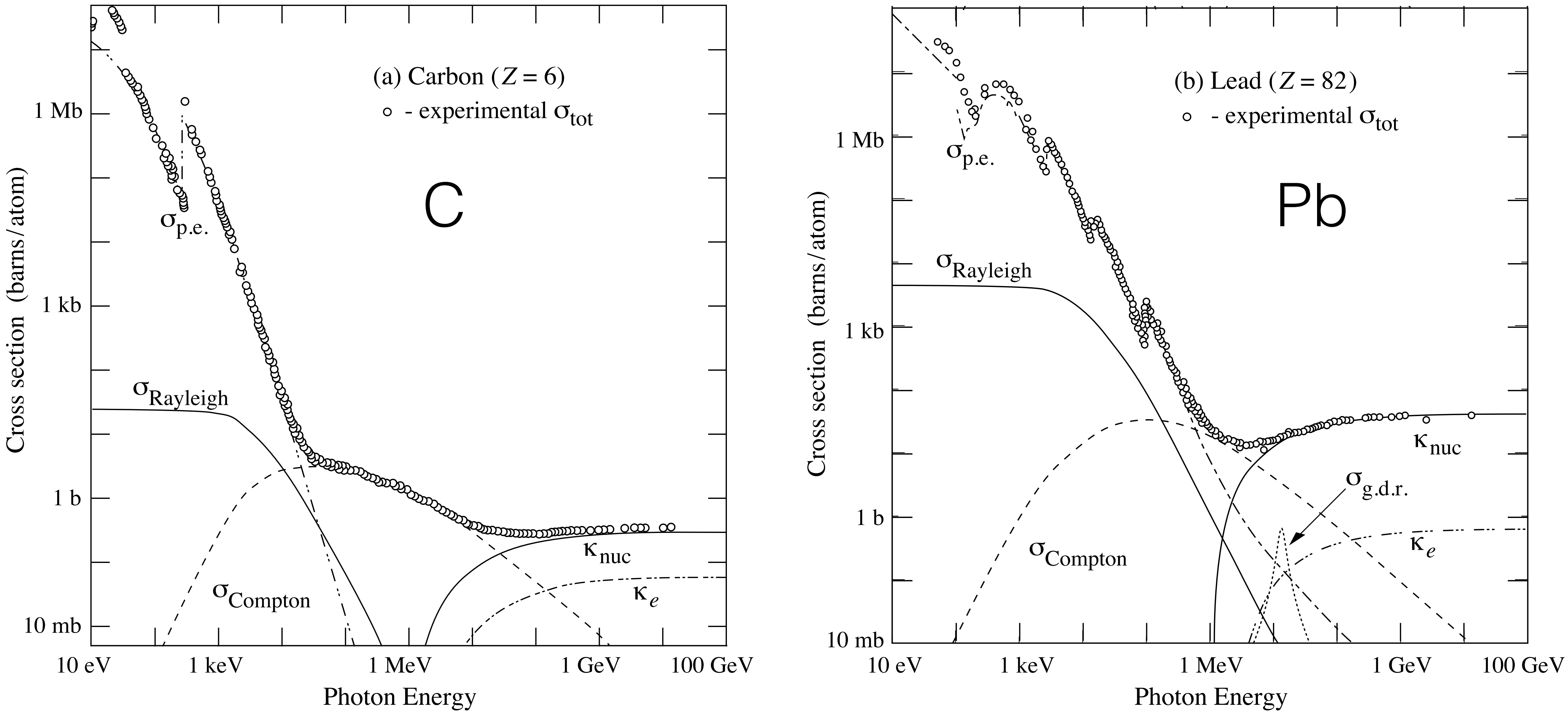

$\sigma_{\text{p.e.}}$ = Atomic photoelectric effect (electron ejection, photon absorption)

σ_{Rayleigh} = Rayleigh (coherent) scattering–atom neither ionized nor excited

σ_{Compton} = Incoherent scattering (Compton scattering off an electron)

κ_{nuc} = Pair production, nuclear field

κ_e = Pair production, electron field

$\sigma_{\text{g.d.r.}}$ = Photonuclear interactions, most notably the Giant Dipole Resonance [52]. In these interactions, the target nucleus is broken up.

Interazione dei fotoni

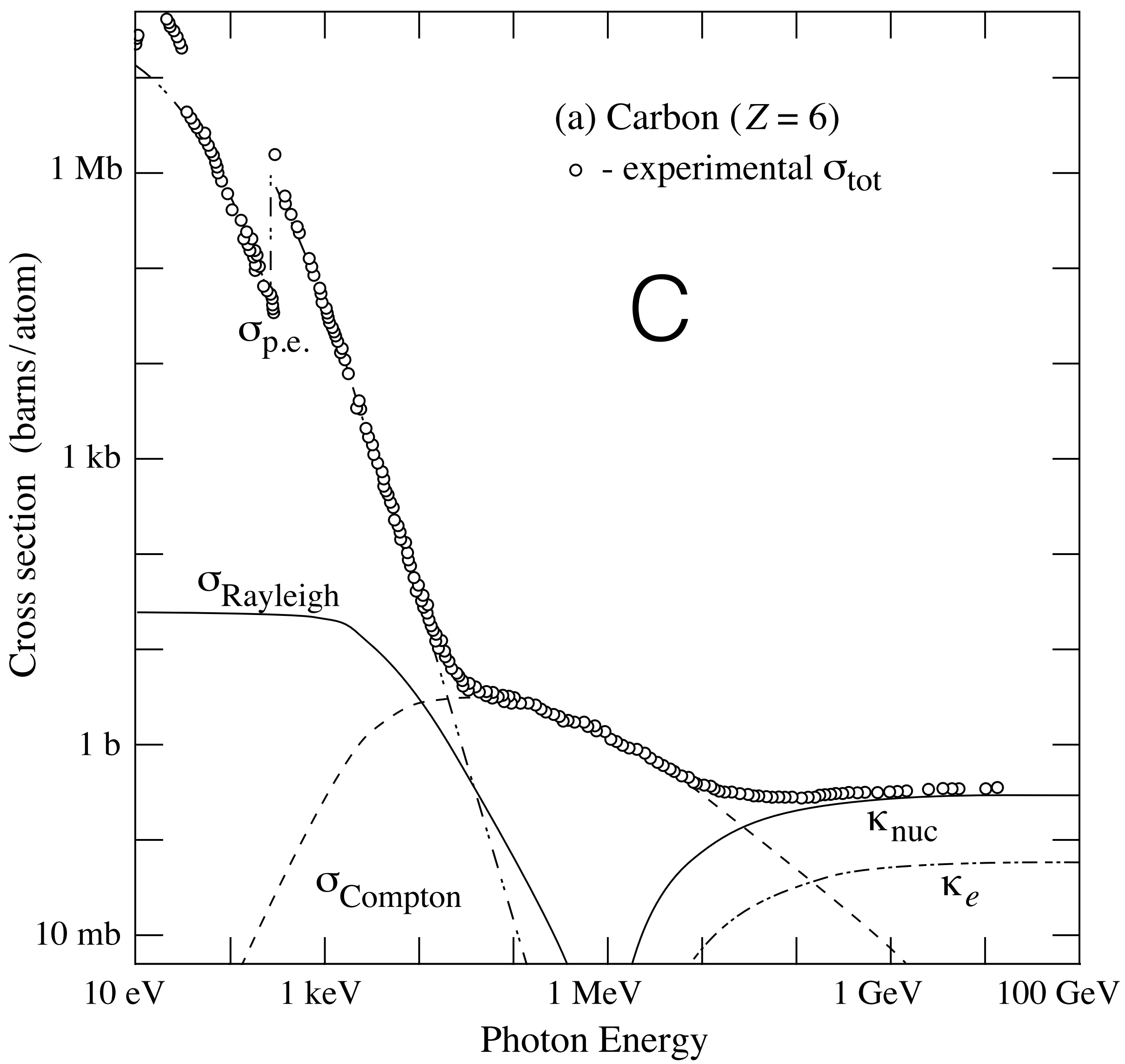

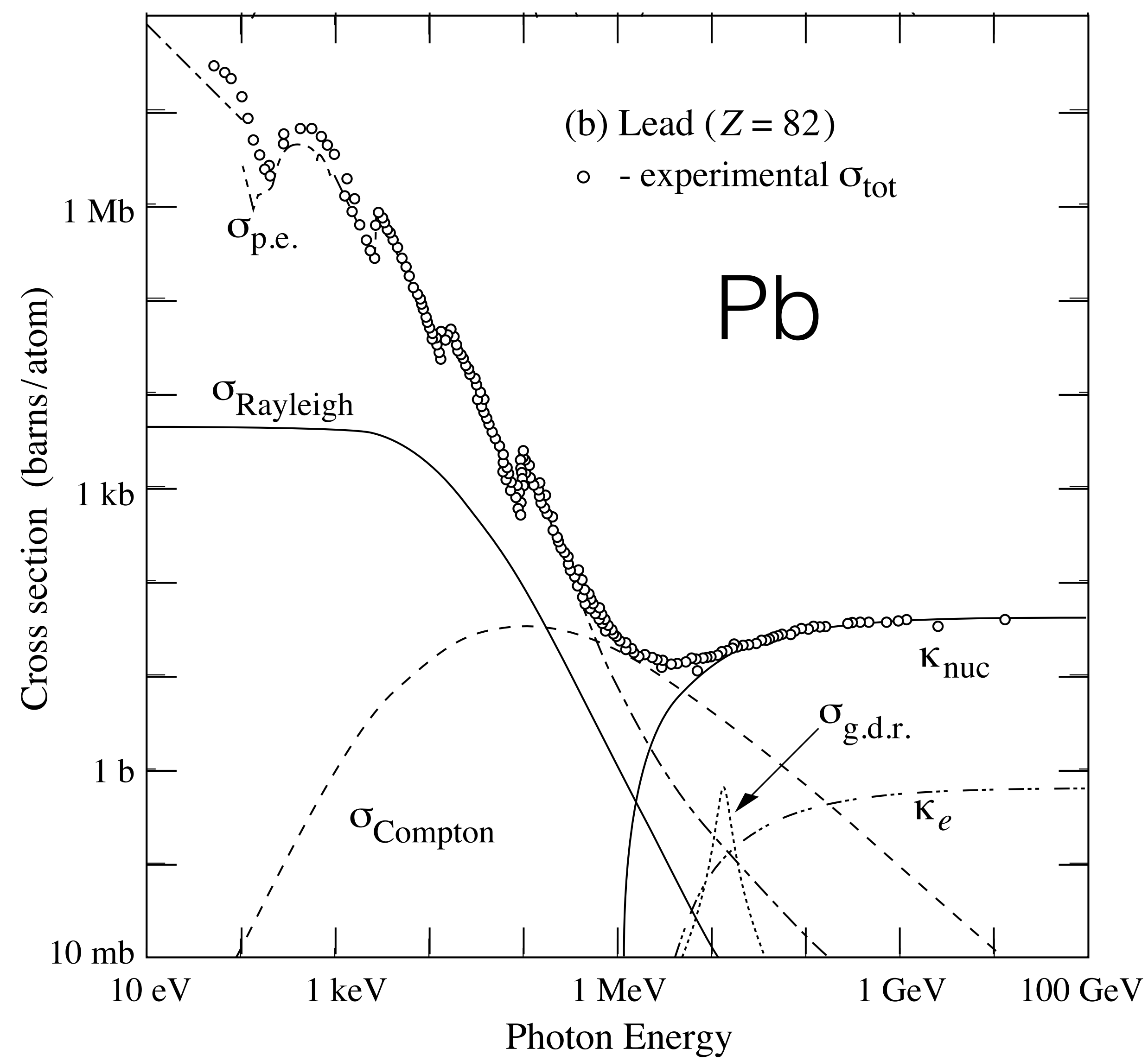

La sezione d'urto dei diversi processi con cui i fotoni interagiscono con gli atomi o con i nuclei (effetto fotoelettrico, effetto Compton e produzione di coppie) dipende dall'energia del fotone incidente e dalle proprietà dei materiali (densità, numero di massa, numero atomico).

In figura d'urto totale (risultati sperimentali) e il risultato del calcolo dei diversi contributi alla sezione d'urto in funzione dell'energia in Carbonio e Piombo.

Interazione dei fotoni

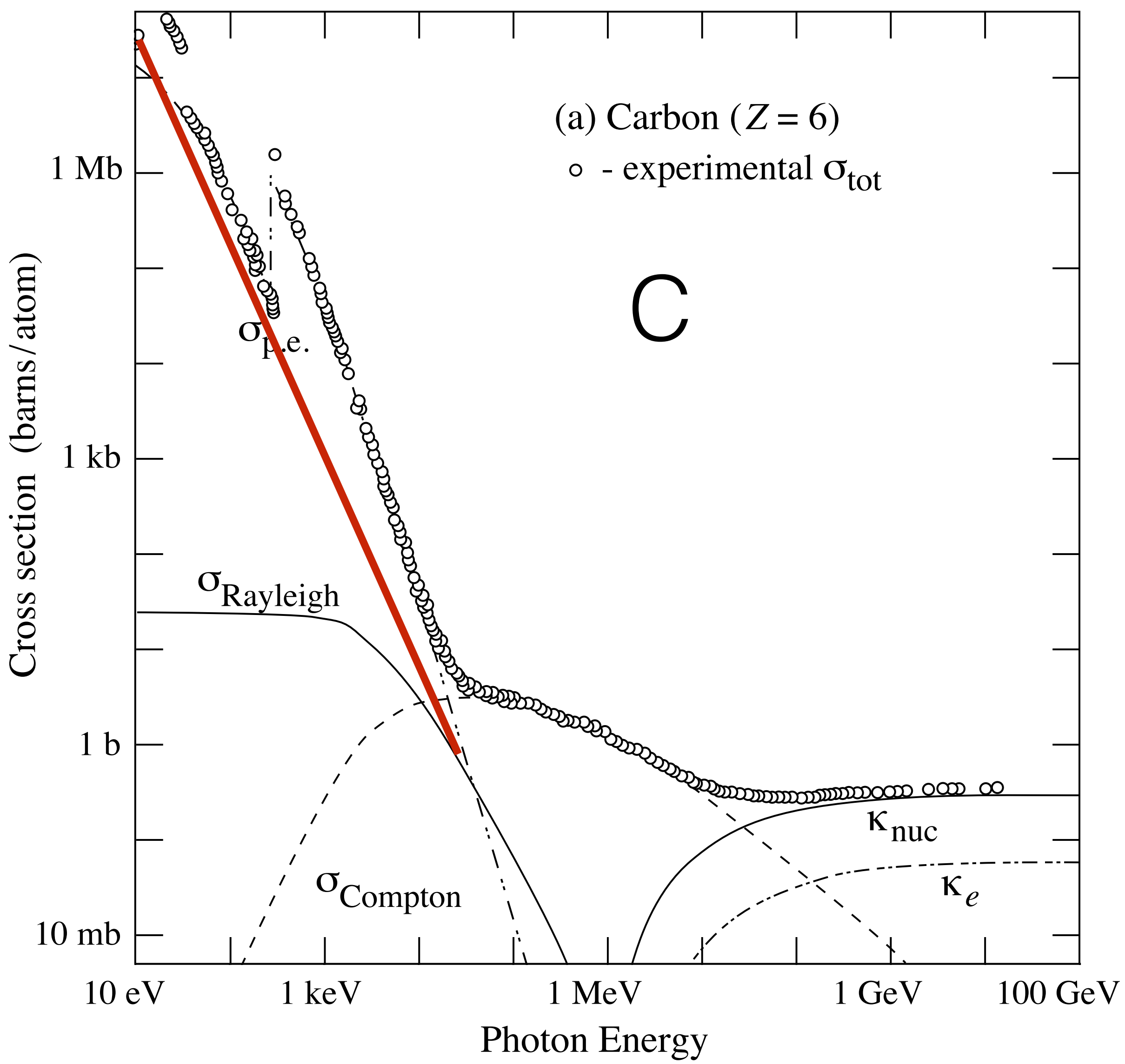

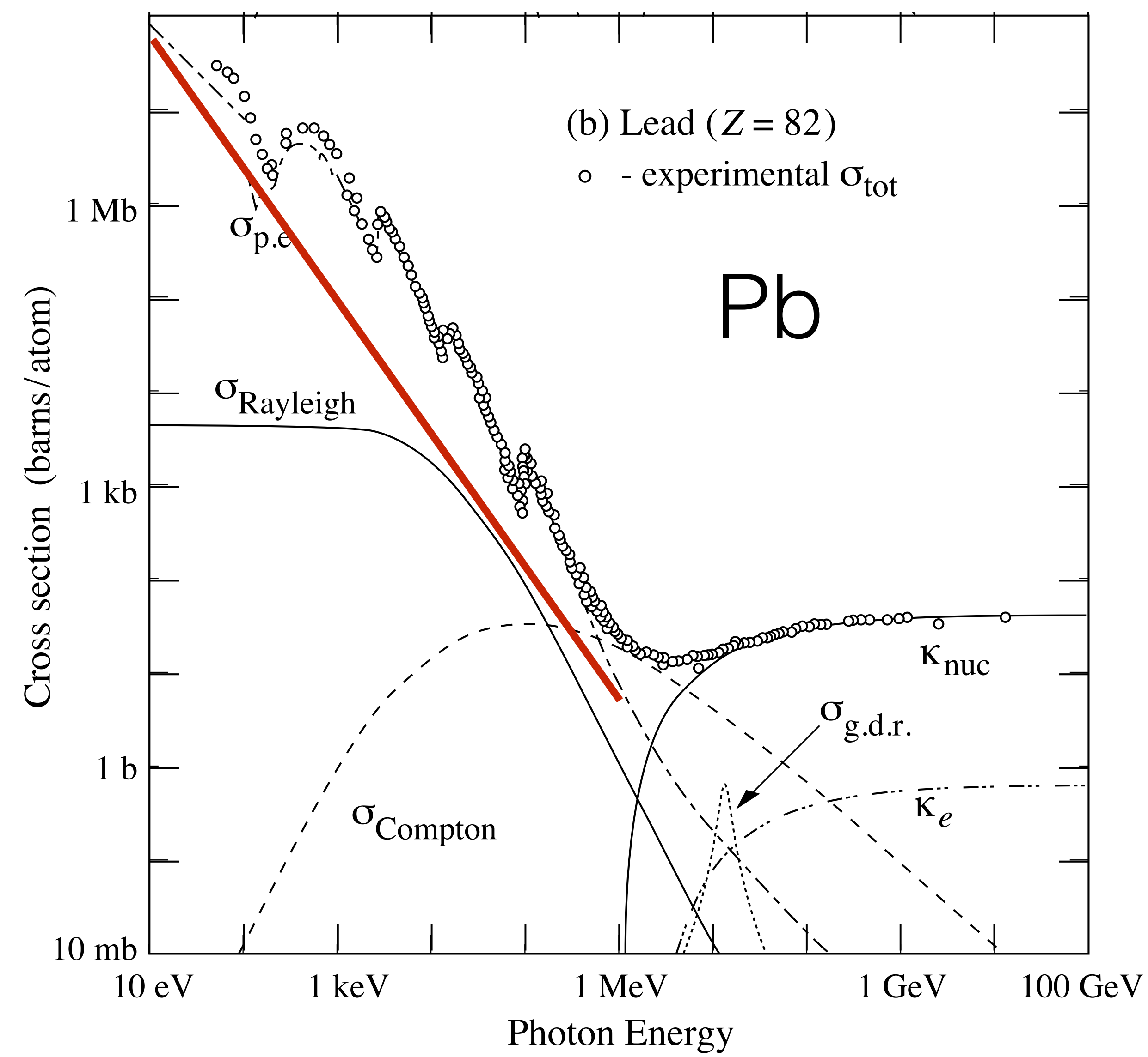

La sezione d'urto per effetto fotoelettrico decresce rapidamente con l'aumentare dell'energia

Interazione dei fotoni

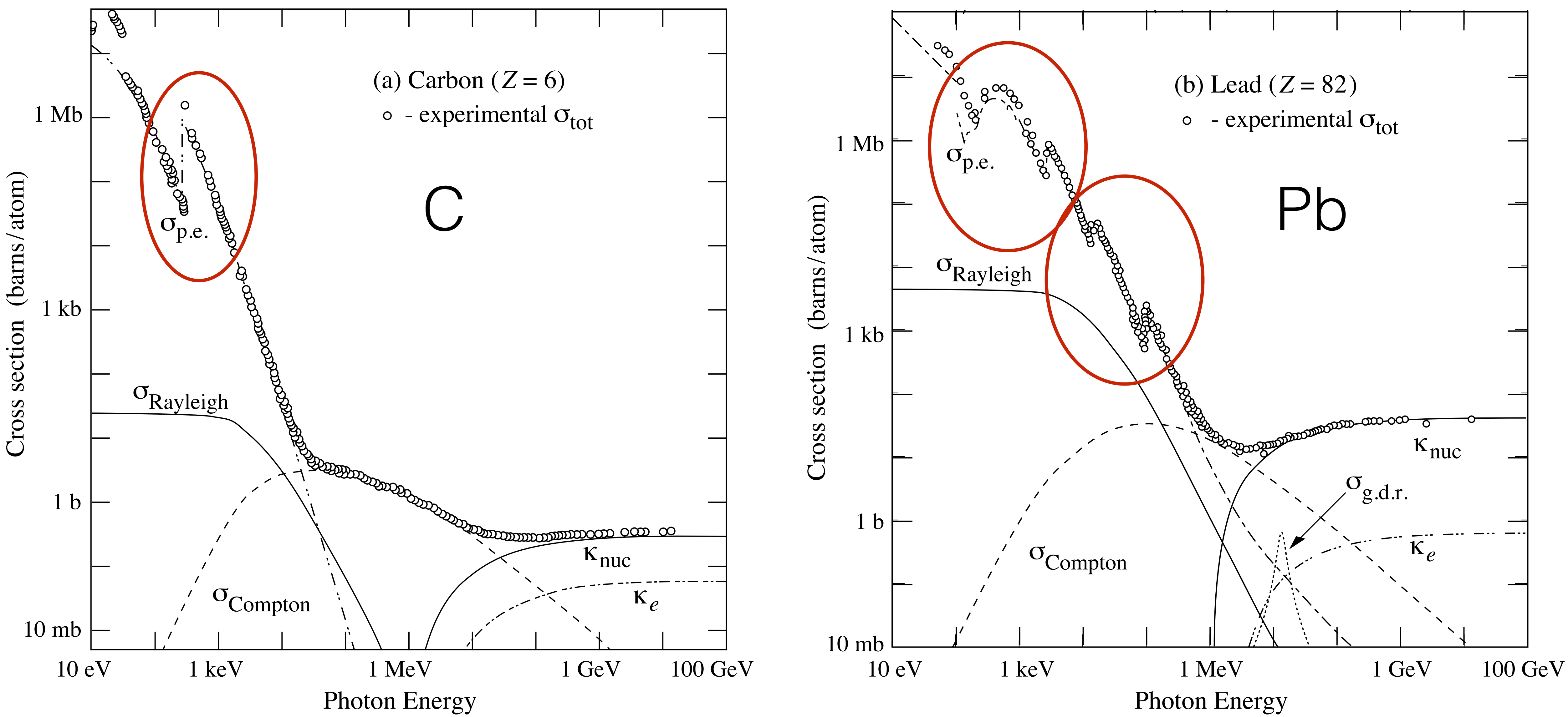

Si osservano le soglie di eccitazione degli elettroni dei diversi orbitali atomici (maggiori per i nuclei più pesanti)

Interazione dei fotoni

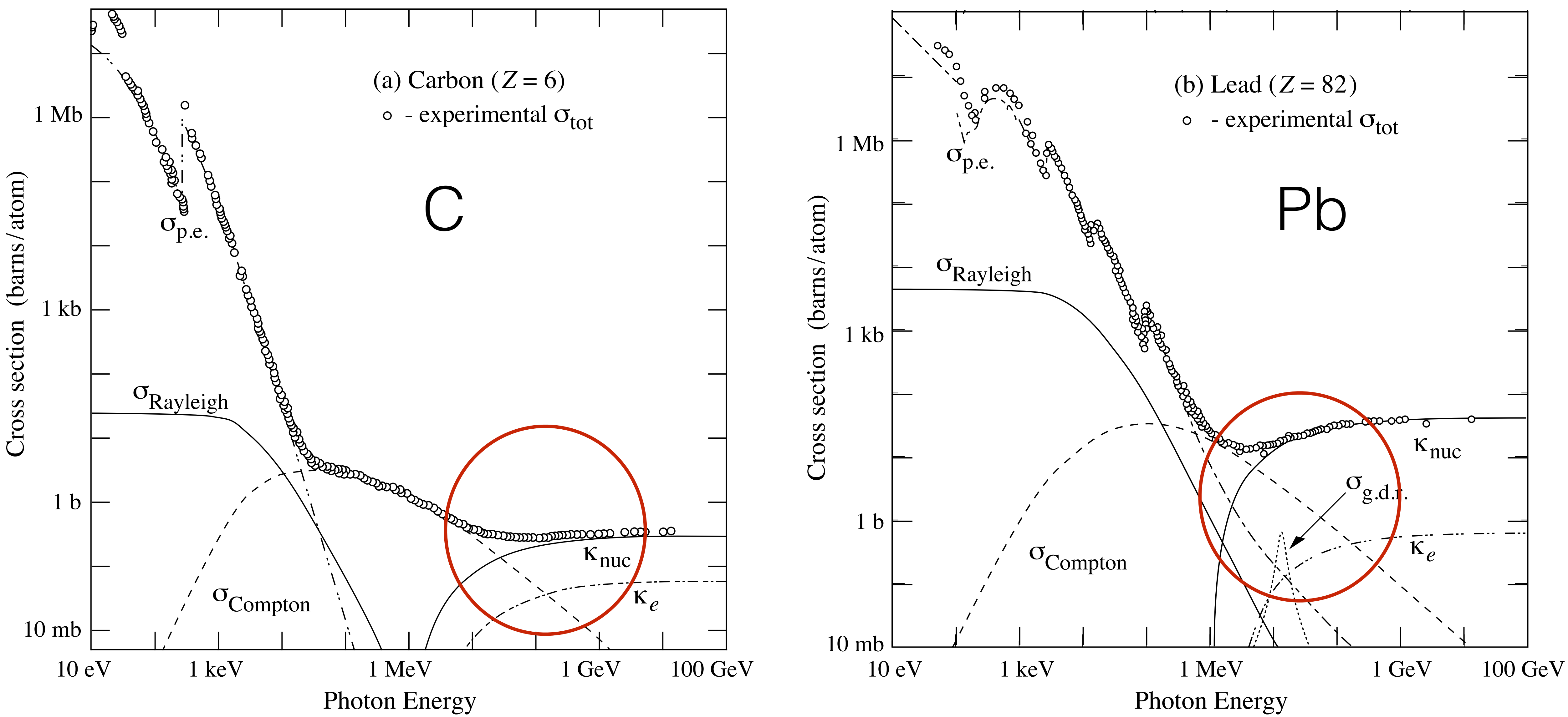

La sezione d'urto per produzione di coppie e^+e^- aumenta rapidamente dopo la soglia ($E_\gamma > 2m_e$) e poi diventa approssimativamente costante

Interazione dei fotoni

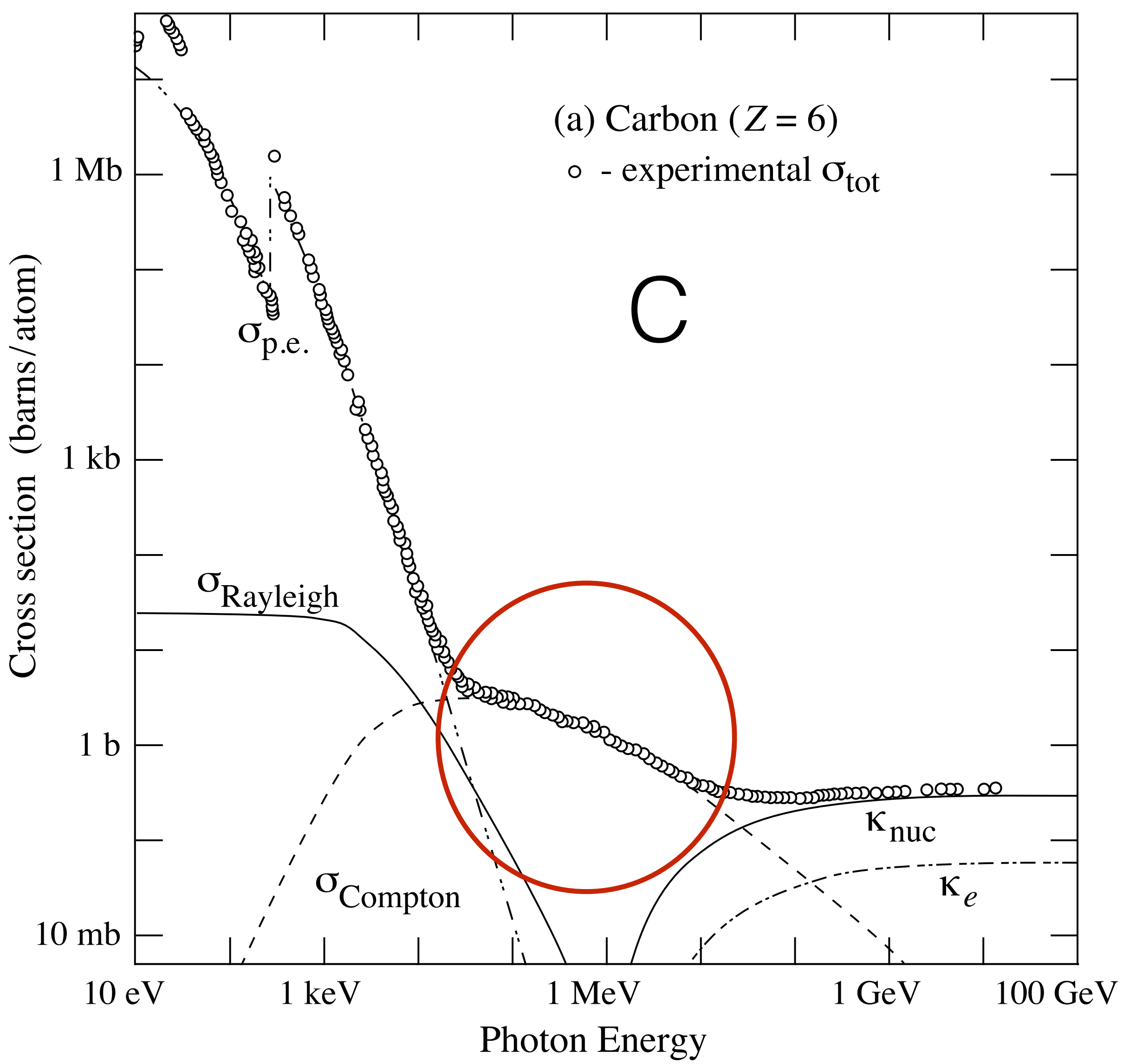

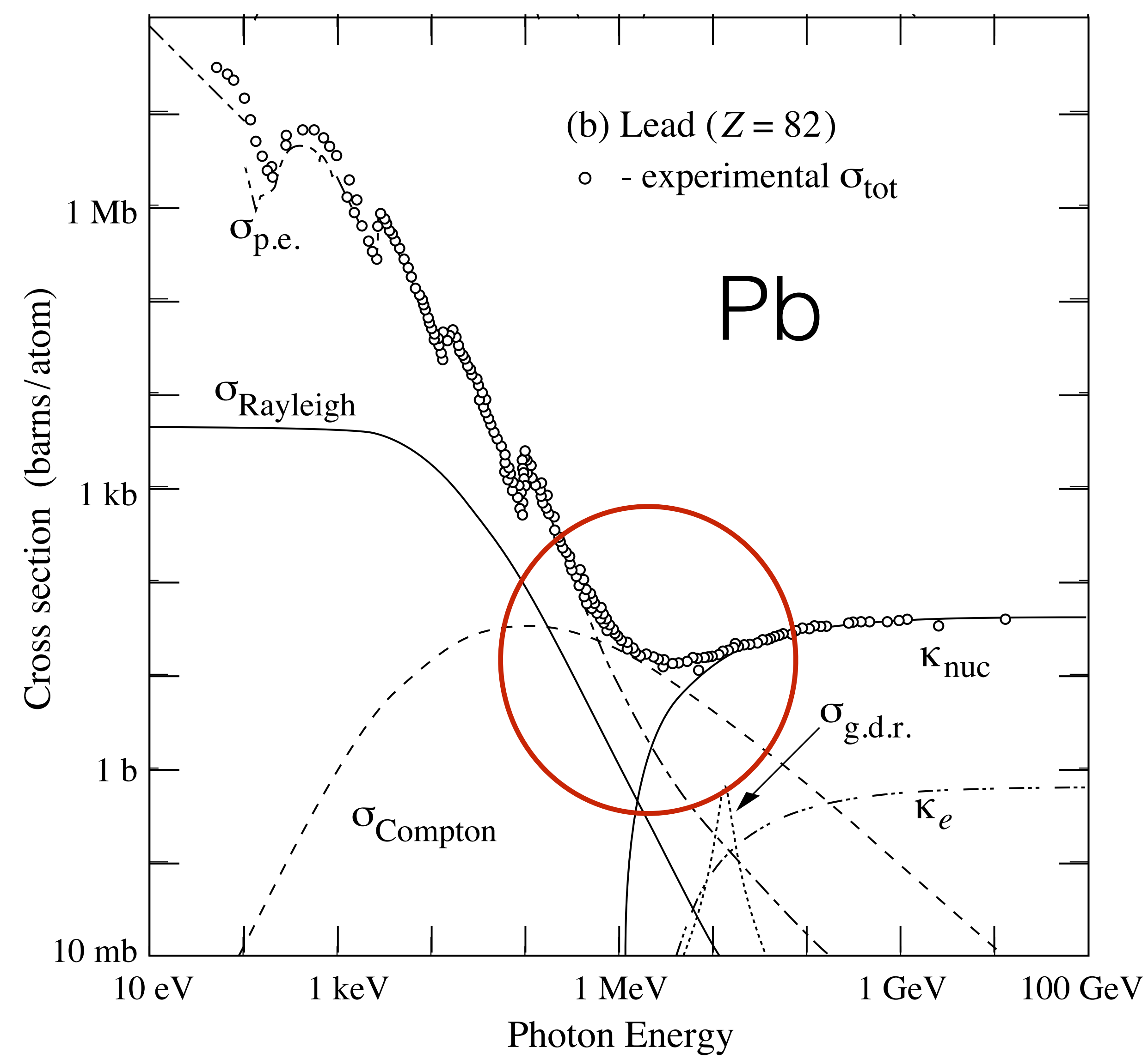

Il contributo dell'effetto Compton è più importante per energie intermedie (E_γ = 100 keV ÷ 10 MeV).

Coefficiente di assorbimento

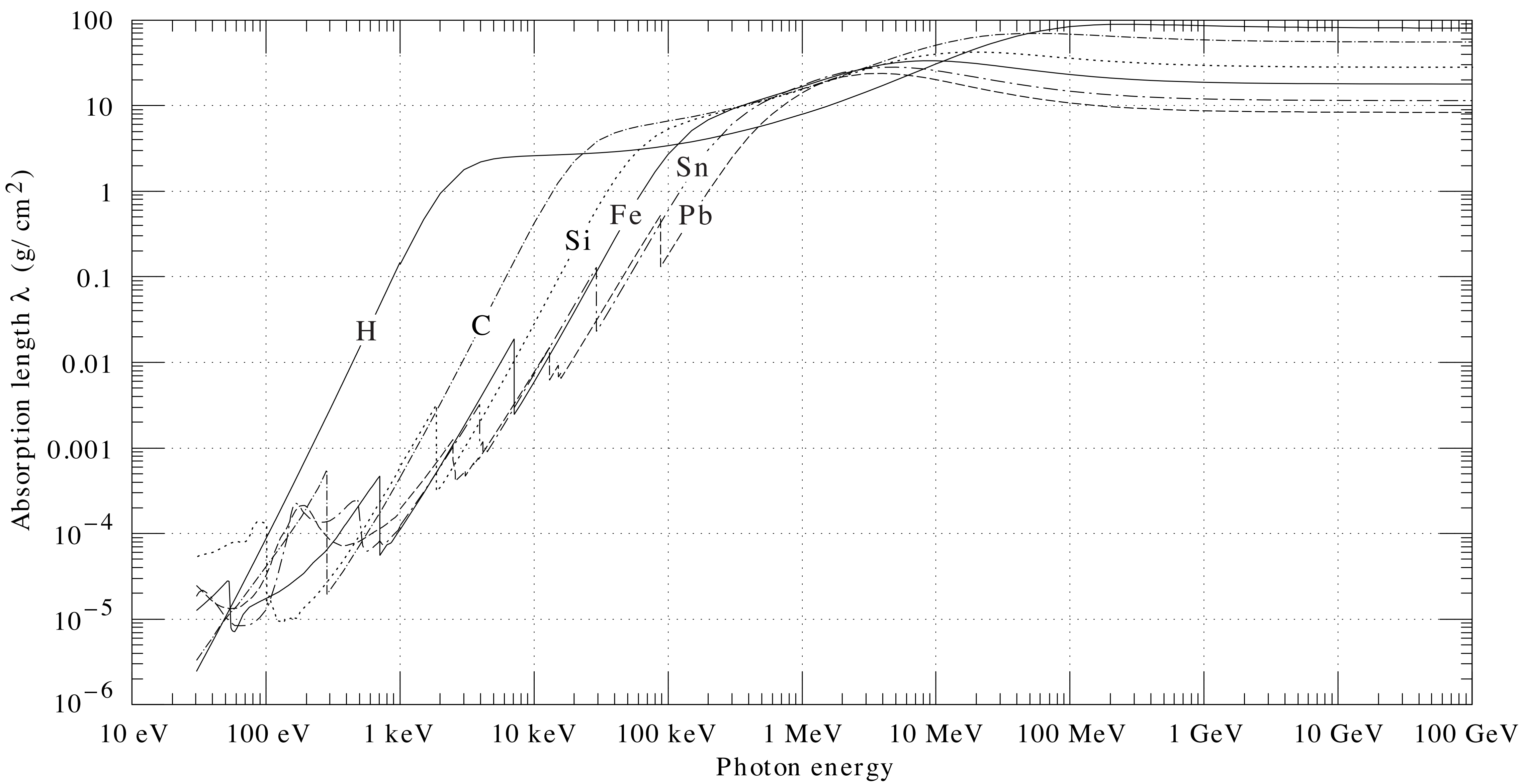

Il coefficiente di assorbimento dei fotoni è la somma dei vari contributi

$\mu_\gamma = \mu_{p.e} + \mu_C + \mu_{p.p.}$

In figura è mostrata la lunghezza di attenuazione $\lambda = 1/\mu$ in g/cm^2 in funzione dell'energia per diversi elementi.

Lunghezza di Radiazione ed Energia Critica

Nucleo	Z	X_0 ($g\ cm^{-2}$)	E_c (MeV)
H	1	63.1	340
He	2	94.3	220
C	6	42.7	103
Al	11	24.0	47
Fe	26	6.4	24
Pb	82	6.4	6.9

Diffusione di Particelle

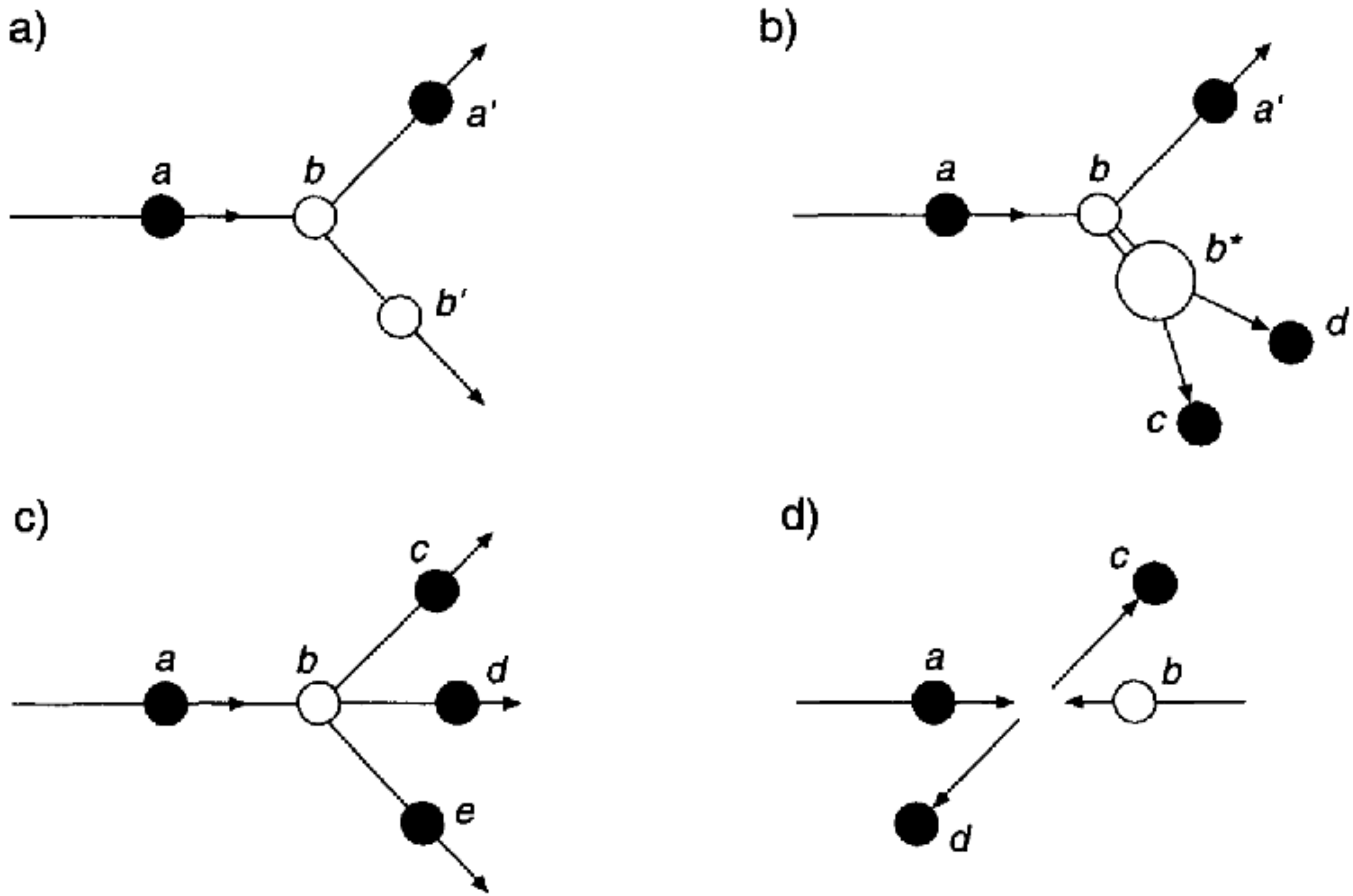

Fig. 4.1. Scattering processes: (**a**) elastic scattering; (**b**) inelastic scattering – production of an excited state which then decays into two particles; (**c**) inelastic production of new particles; (**d**) reaction of colliding beams.

Sezione d'urto

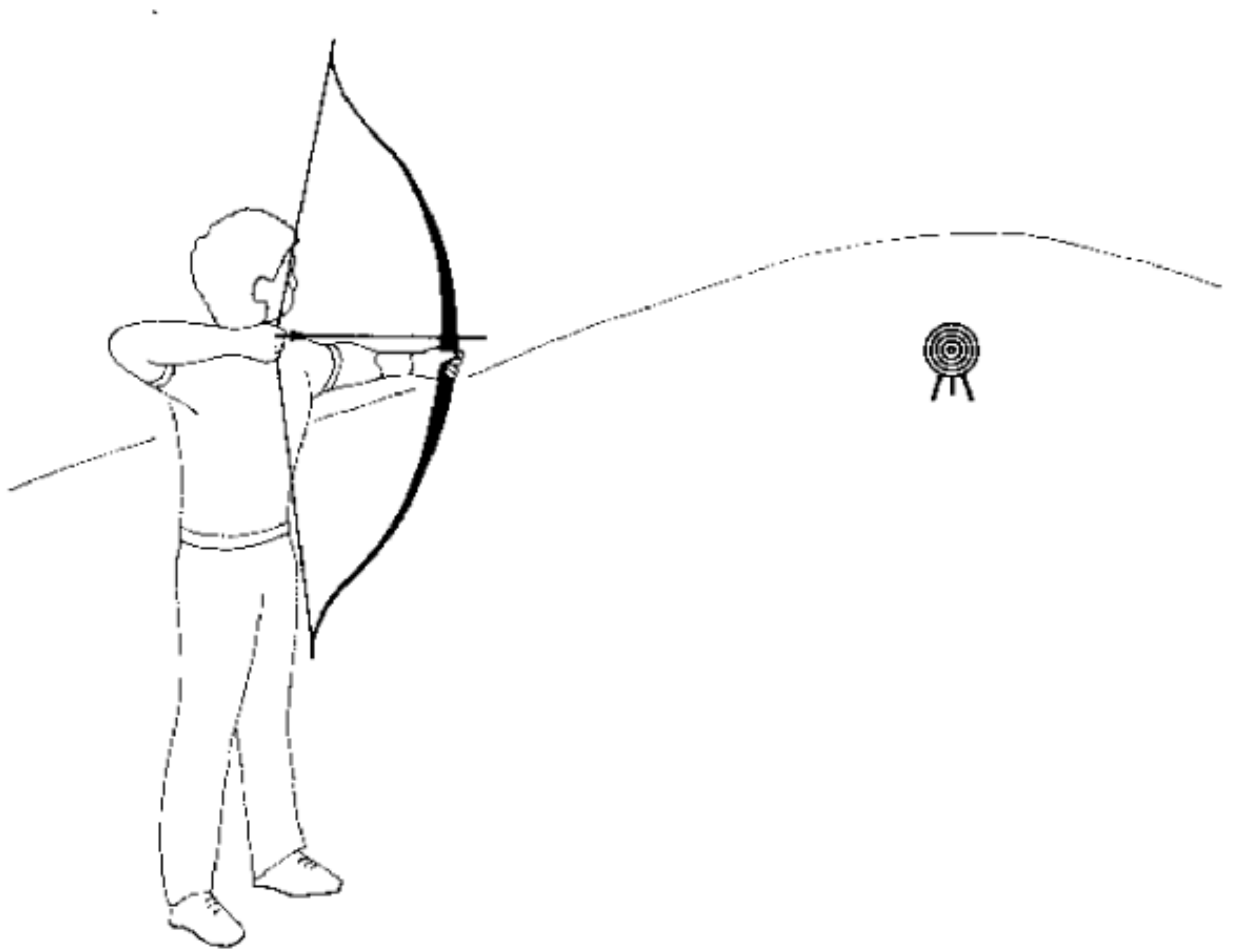

Fig. 2.8 Collisions in atomic and subatomic physics cannot be arranged in the same way as an archer tries to score a bull's-eye on the target. Instead the situation is more like that in Fig. 2.9.

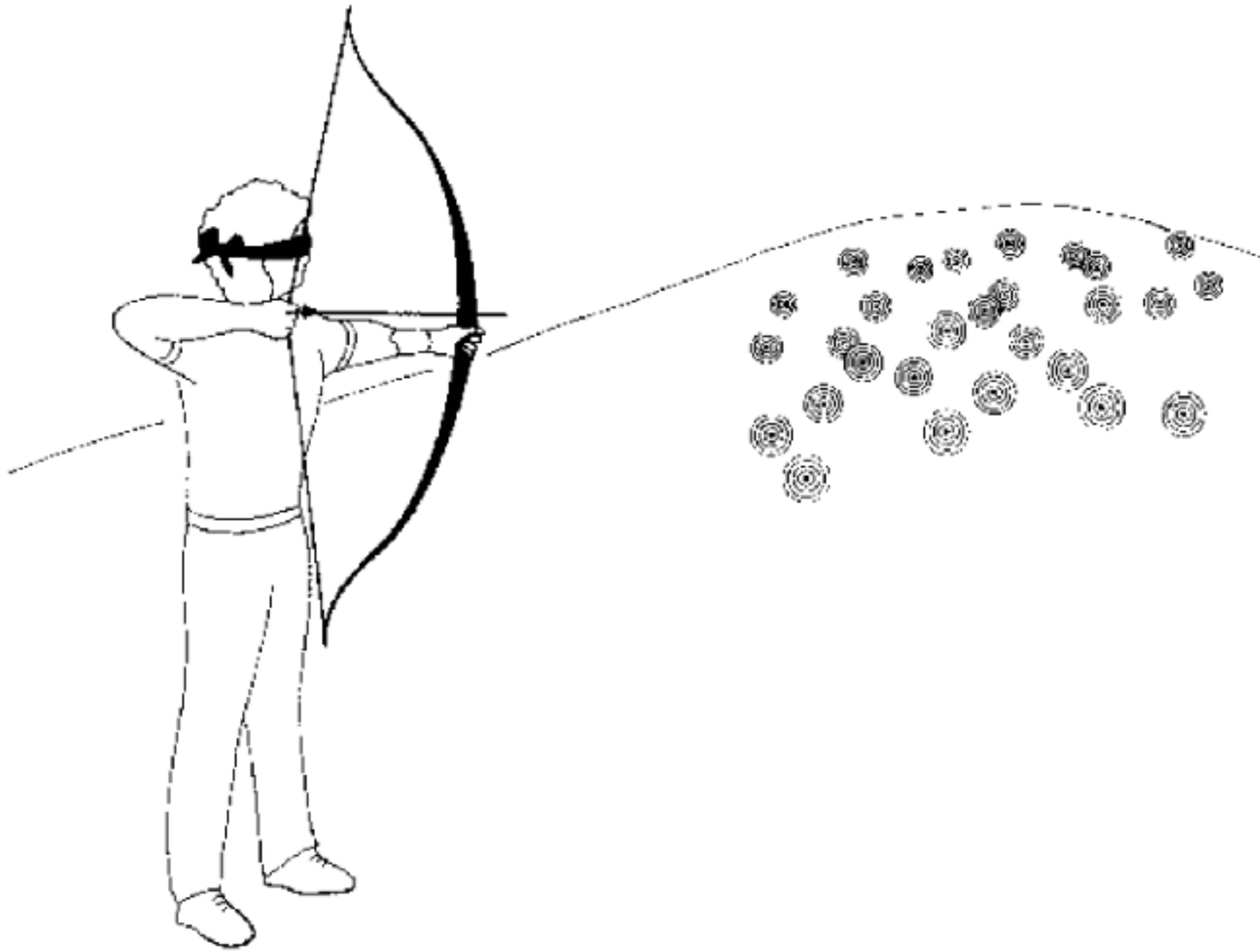

Fig. 2.9 Clearly the chance that the blindfolded archer hits any target is proportional to the density of targets and to the area (cross-section) presented by each, and to the number of arrows that he fires if he has more than one attempt, provided, of course, that he is firing into the region of the assembly of targets. When an arrow does strike the target the archer will score depending on which ring of the target is struck. The probability of a given single score for the blind archer will be proportional to that partial area of the whole target which yields that score. In atomic and nuclear collisions the total cross-section gives the probability that a collision will occur and a partial cross-section gives the probability that the collision has a given outcome.

Sezione d'urto

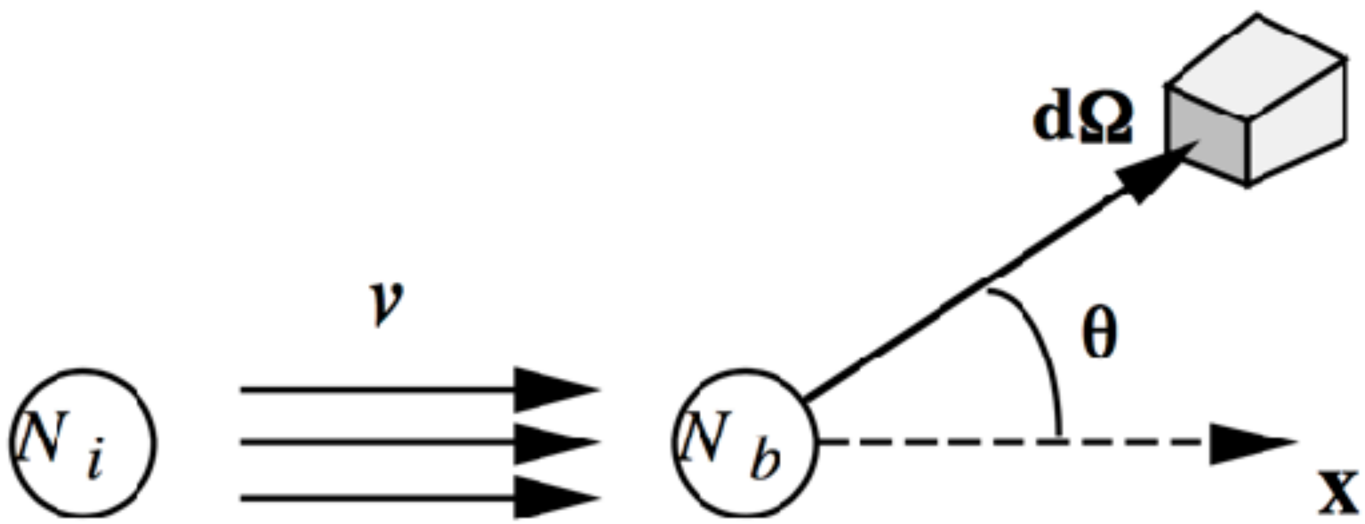

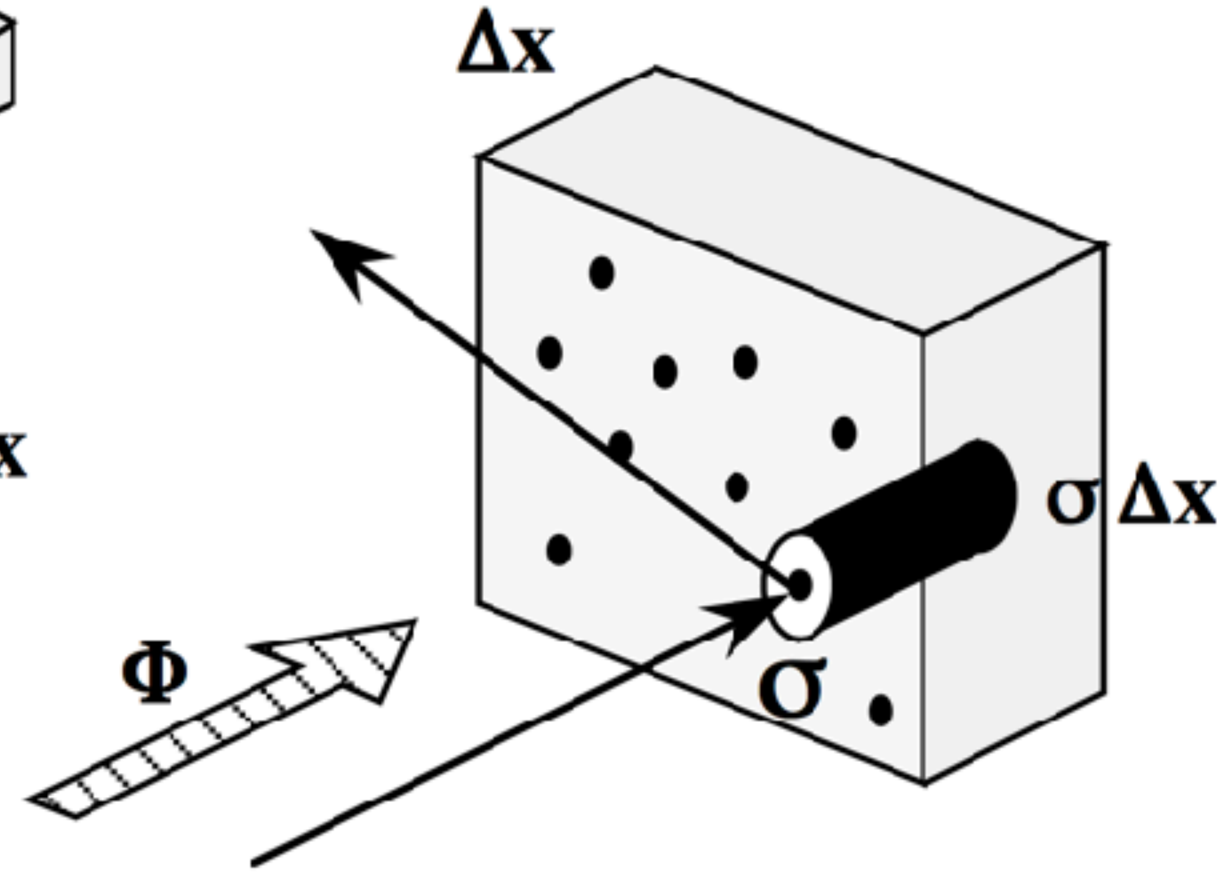

Sezione d'urto differenziale

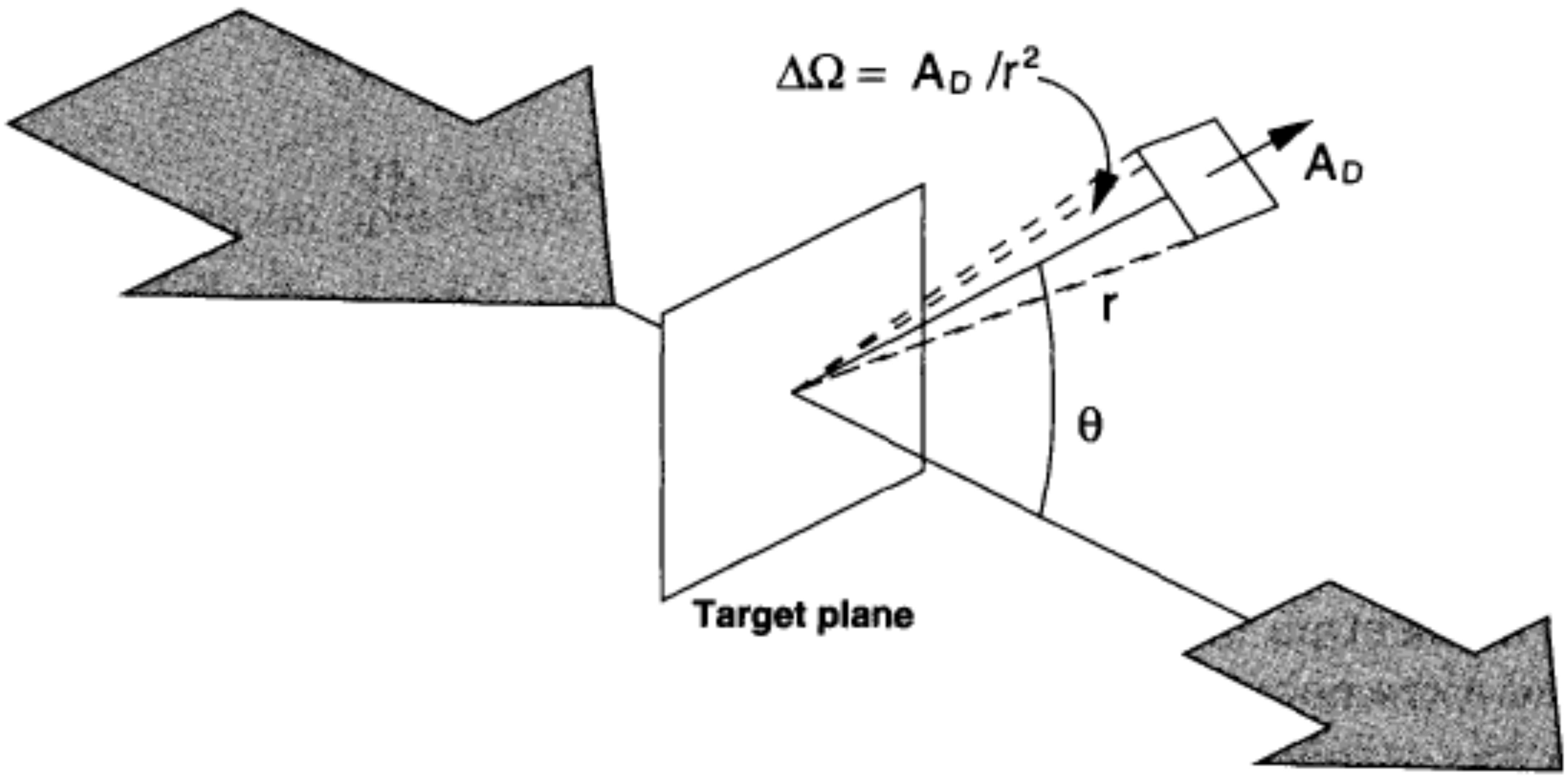

Catene di decadimento

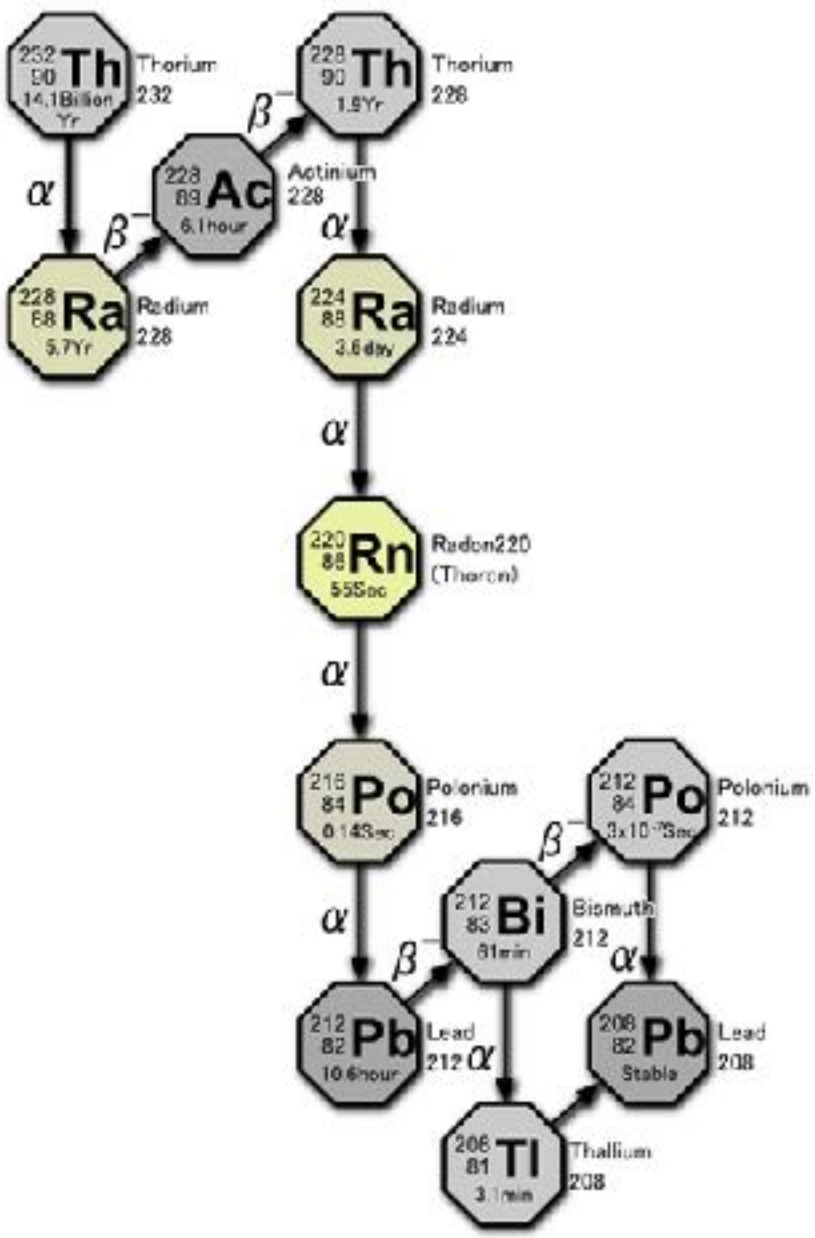

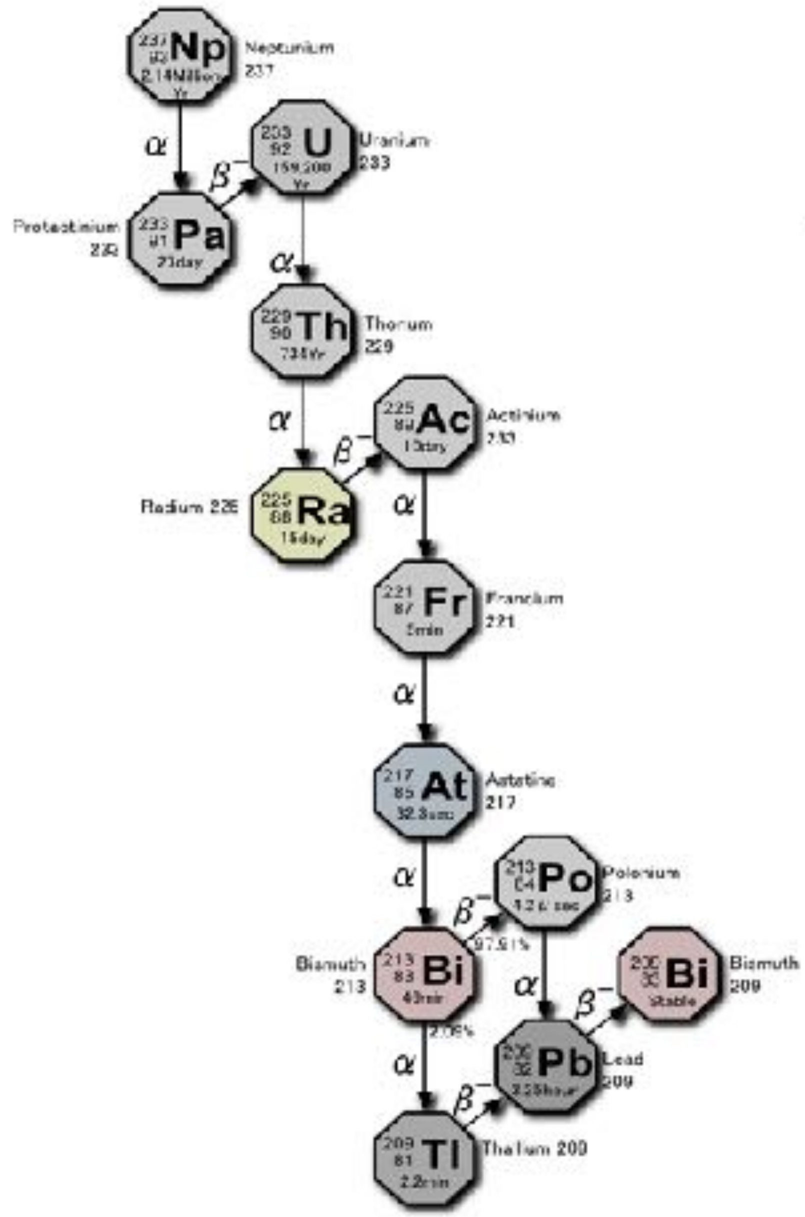

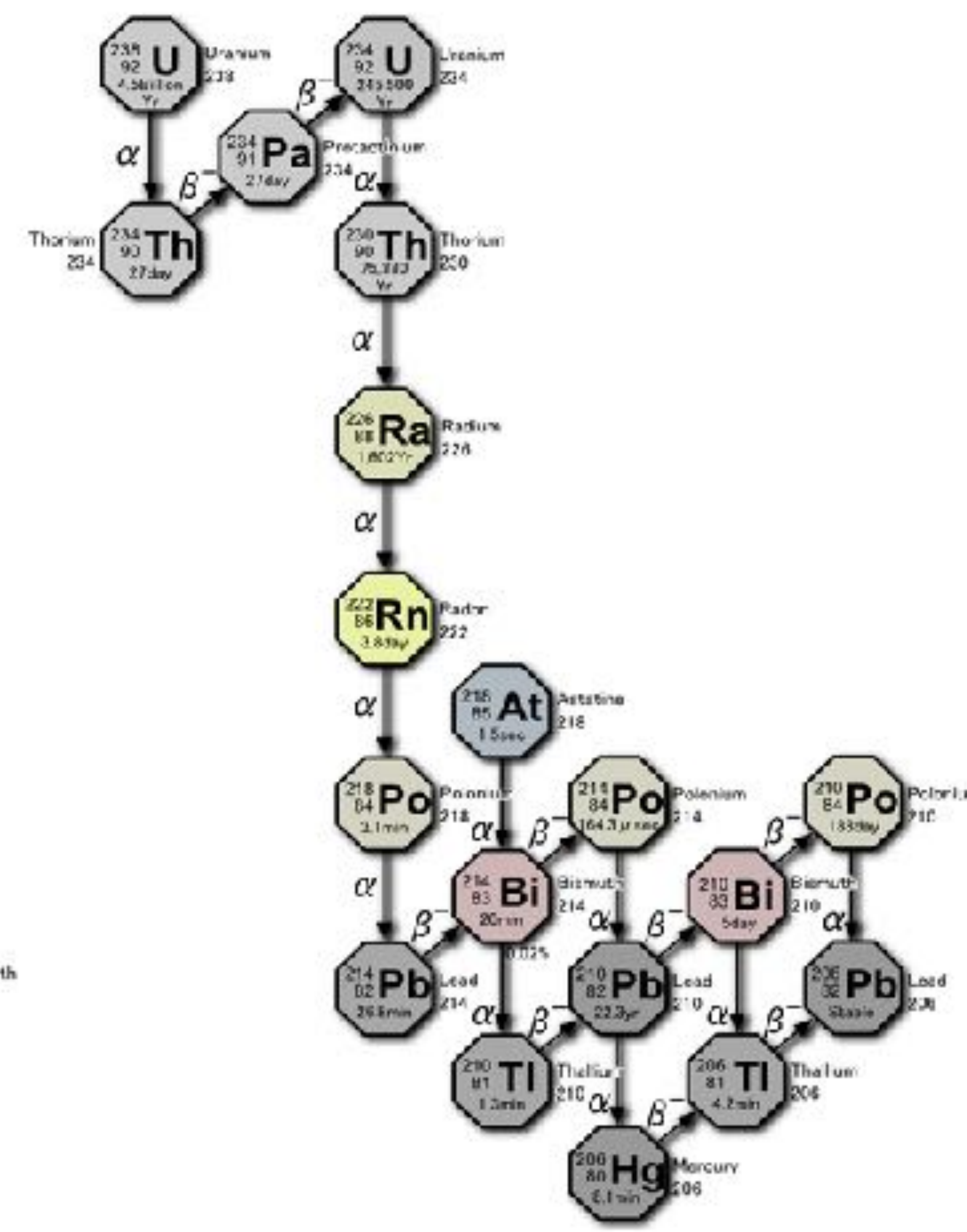

Modelli Nucleari

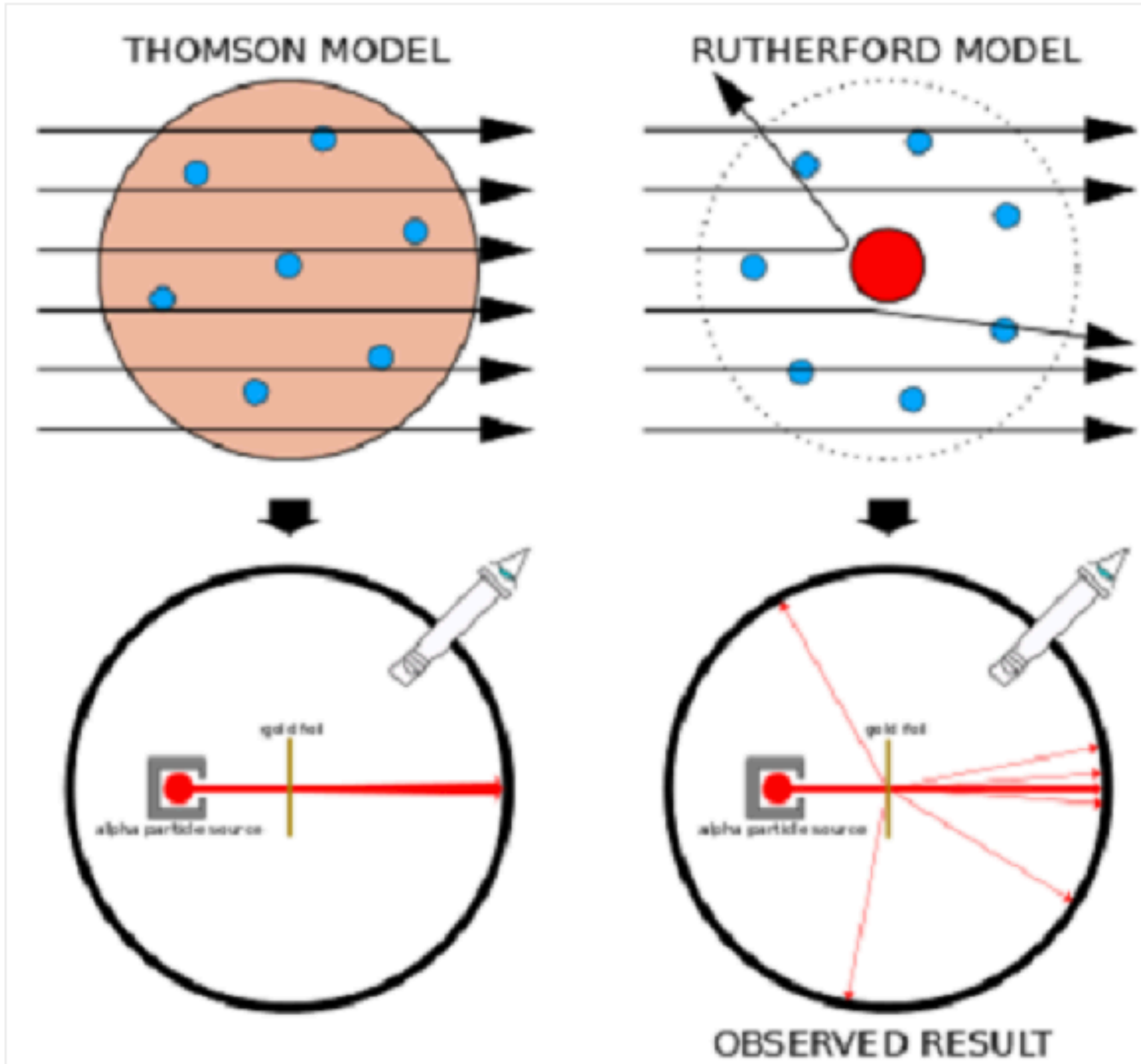

Scattering Rutherford

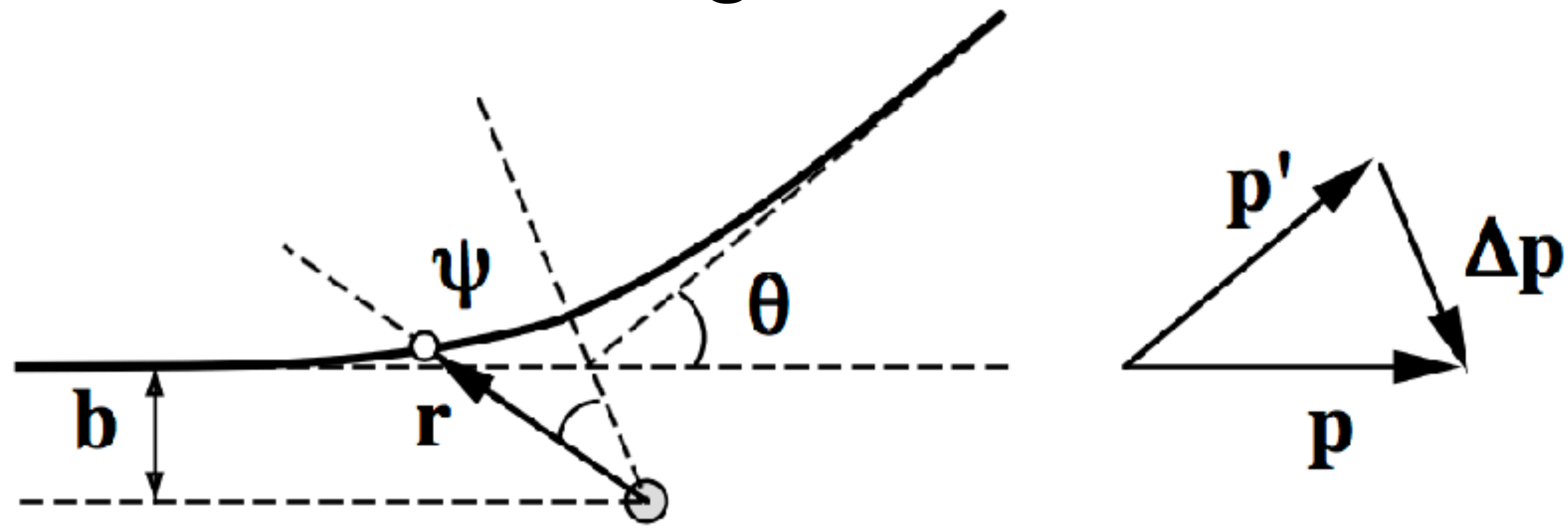

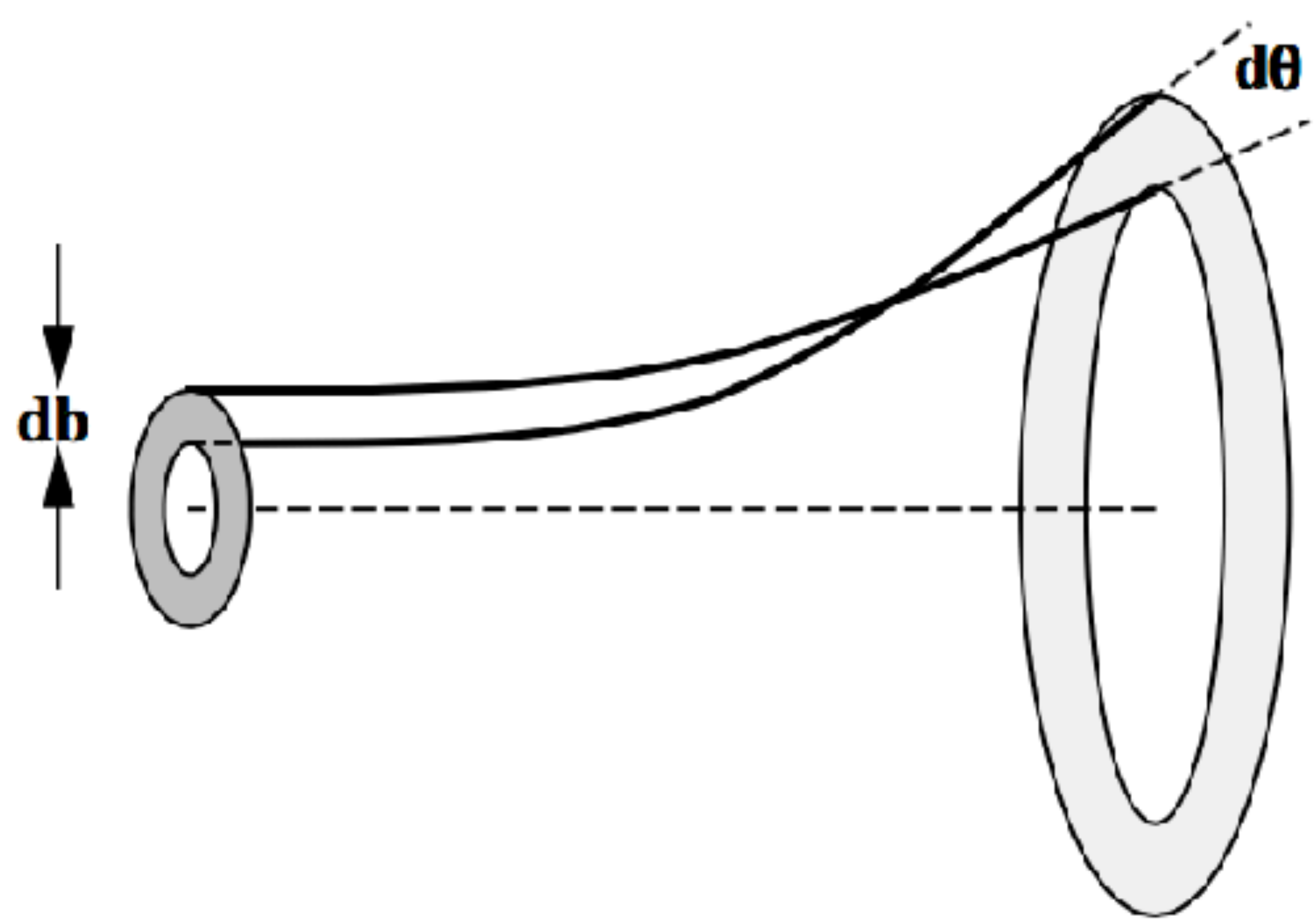

Scattering Rutherford

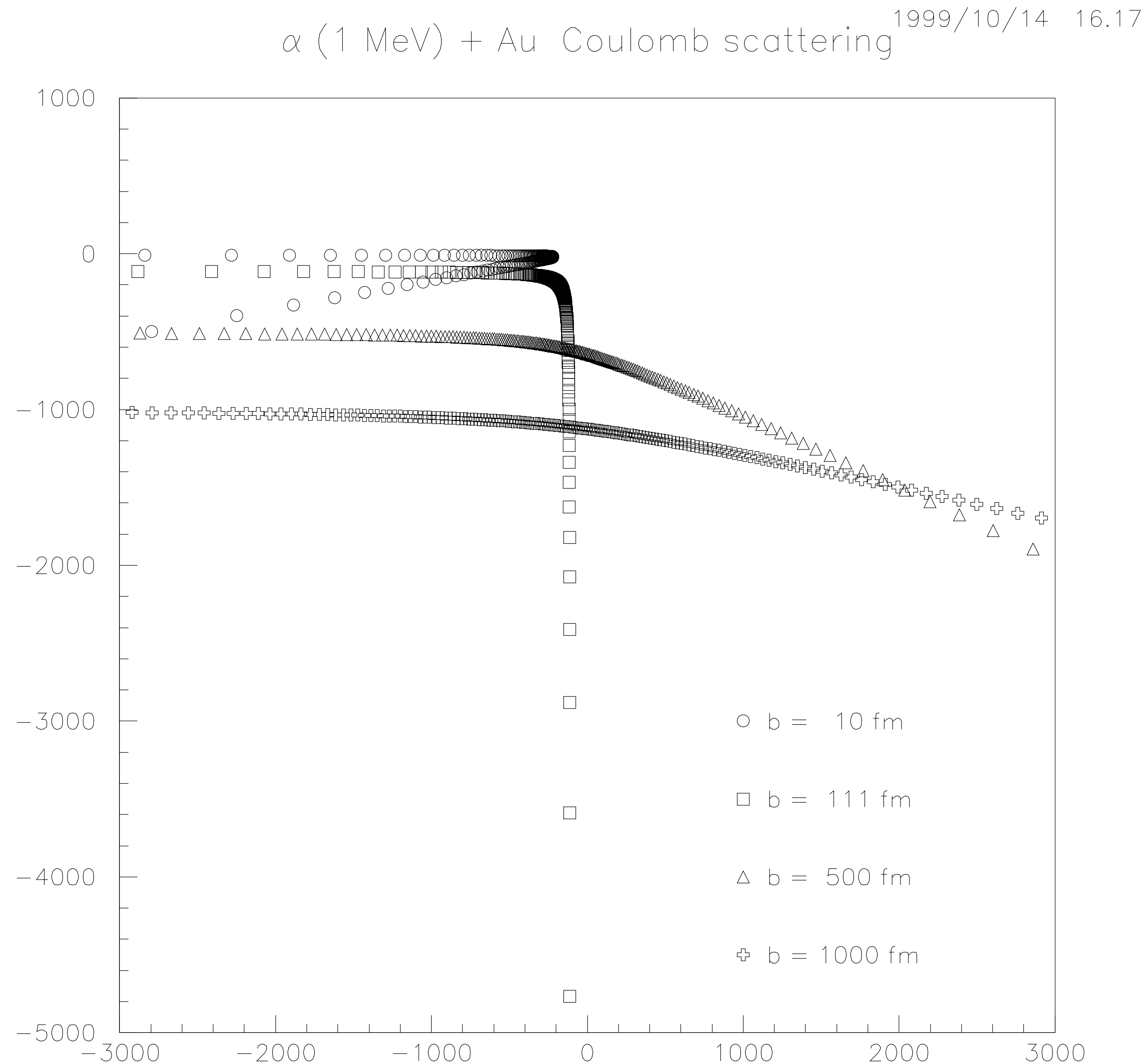

Esperimento di Geiger e Marsden

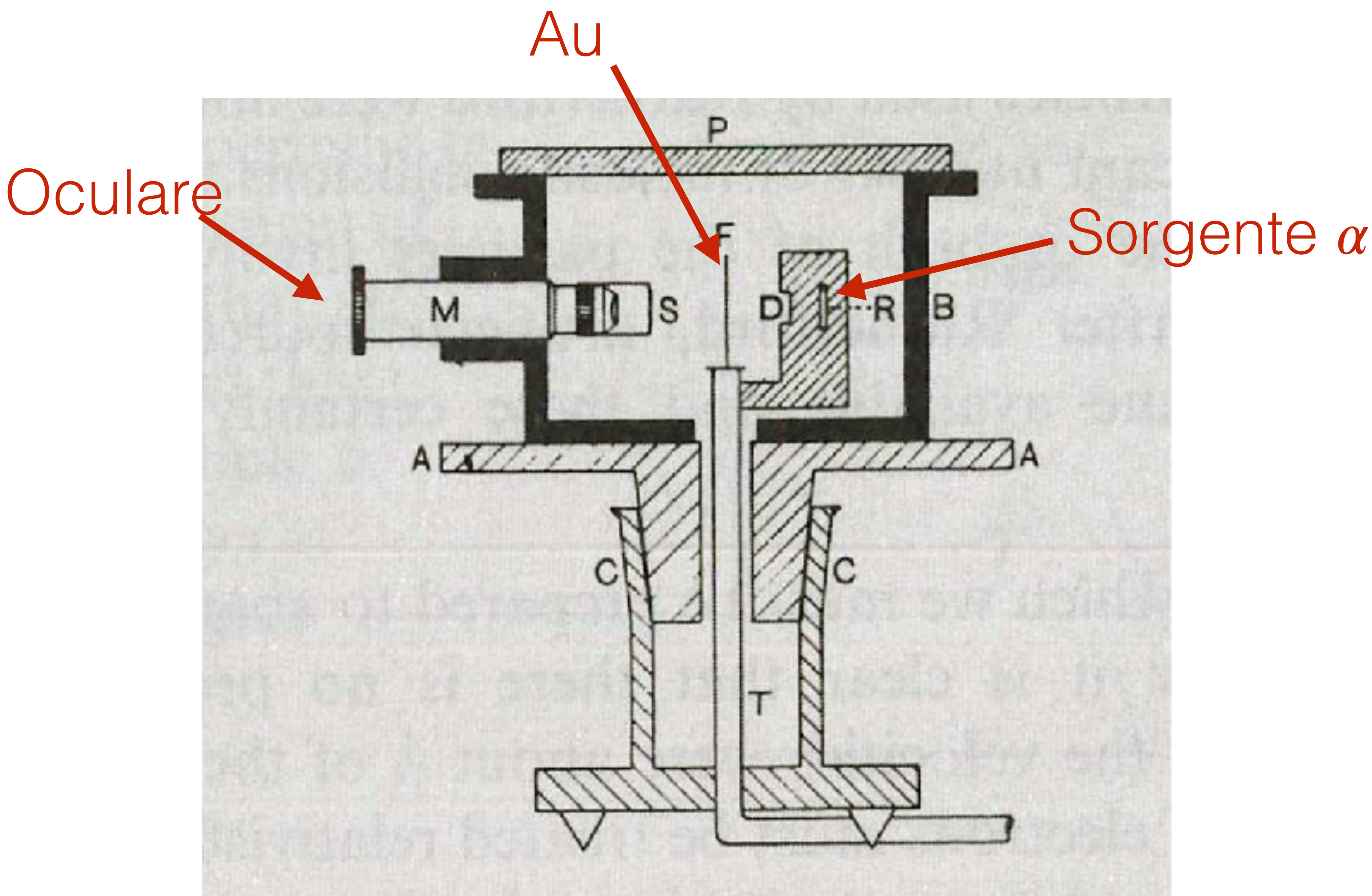

Esperimento di Geiger e Marsden

Variation of scattering with angle.

I	II	III	IV	V	VI
		Silver		Gold	
Angle of deflection, ϕ	$\operatorname{cosec}^4 \frac{1}{2}\phi$	Number of scintillations, N	$\frac{N}{\operatorname{cosec}^4 \frac{1}{2}\phi}$	Number of scintillations, N	$\frac{N}{\operatorname{cosec}^4 \frac{1}{2}\phi}$
150°	1·15	22·2	19·3	33·1	28·8
135	1·38	27·4	19·8	43·0	31·2
120	1·79	33·0	18·4	51·9	29·0
105	2·53	47·3	18·7	69·5	27·5
75	7·25	136	18·8	211	29·1
60	16·0	320	20·0	477	29·8
45	46·6	989	21·2	1435	30·8
37·5	93·7	1760	18·8	3300	35·3
30	223	5260	23·6	7800	35·0
22·5	690	20300	29·4	27300	39·6
15	3445	105400	30·6	132000	38·4
30	223	5·3	0·024	3·1	0·014
22·5	690	16·6	0·024	8·4	0·012
15	3445	93·0	0·027	48·2	0·014
10	17330	508	0·029	200	0·0115
7·5	54650	1710	0·031	607	0·011
5	276300	—	—	3320	0·012

Sezione d'urto di Mott

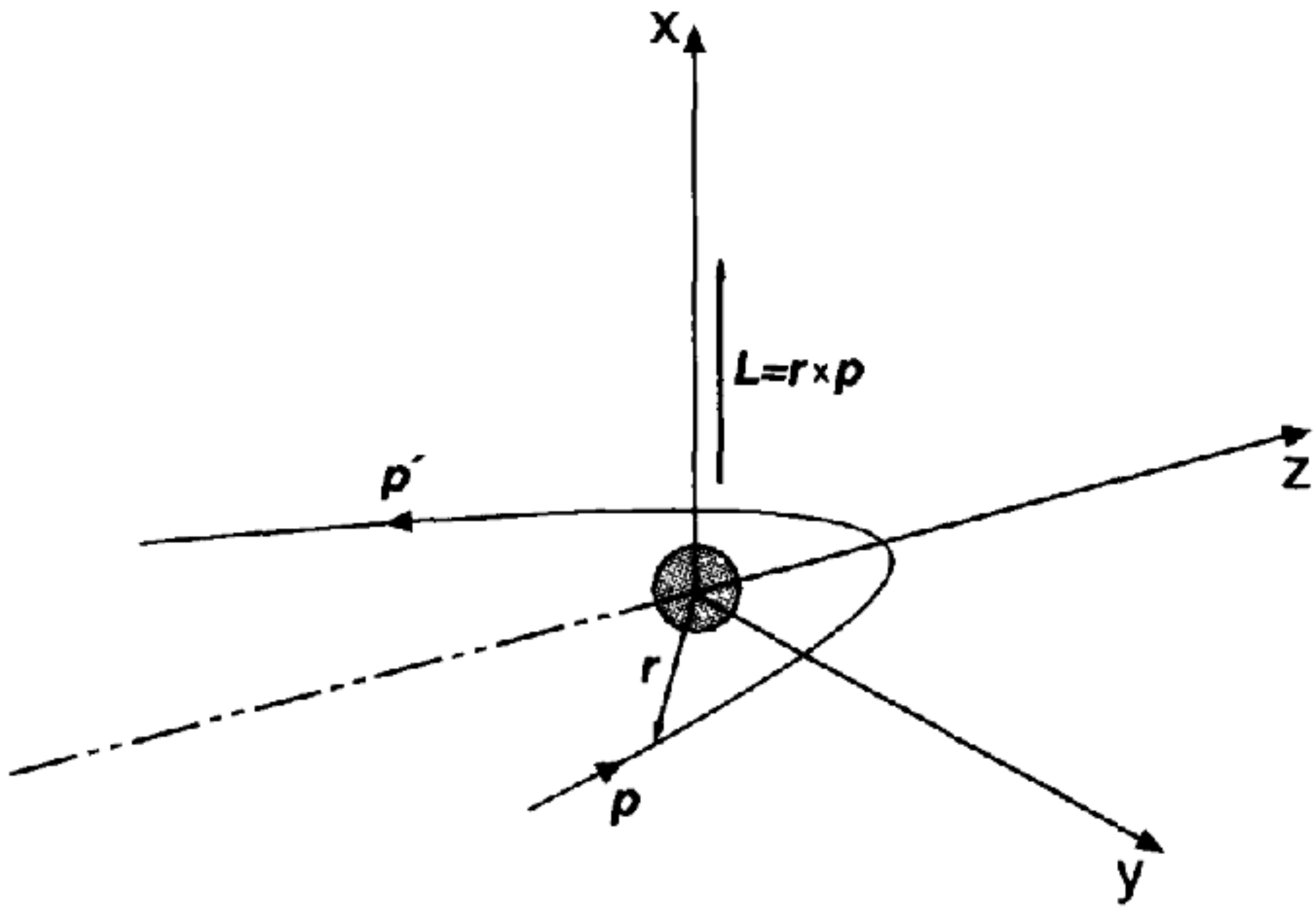

Fig. 5.3. Helicity, $h = \boldsymbol{s} \cdot \boldsymbol{p}/(|\boldsymbol{s}| \cdot |\boldsymbol{p}|)$, is conserved in the $\beta \rightarrow 1$ limit. This means that the spin projection on the z-axis would have to change its sign in scattering through 180°. This is impossible if the target is spinless, because of conservation of angular momentum.

Fattori di Forma

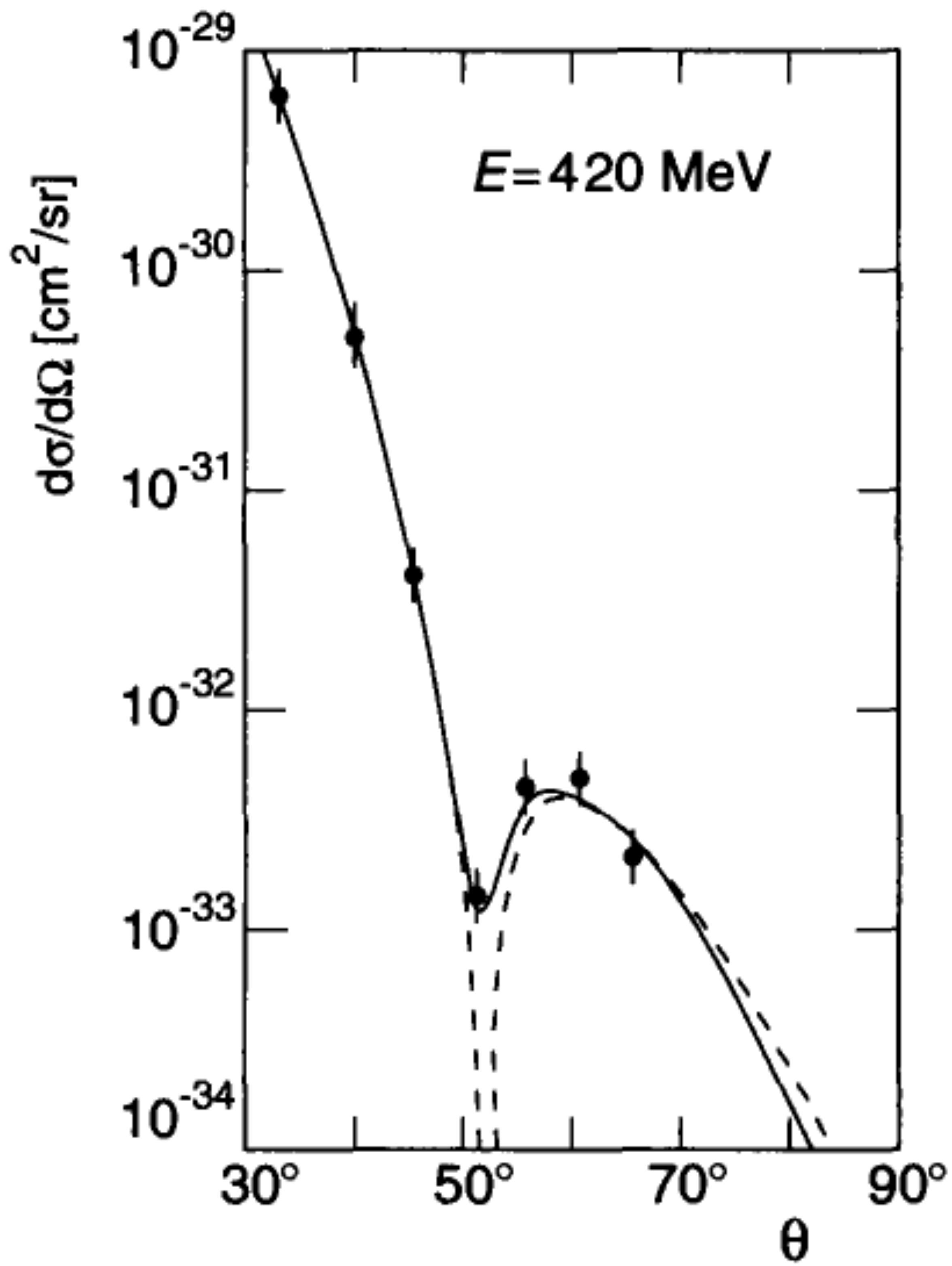

Fig. 5.5. Measurement of the form factor of ^{12}C by electron scattering (from [Ho57]). The figure shows the differential cross-section measured at a fixed beam energy of 420 MeV, at 7 different scattering angles. The dashed line corresponds to scattering of a plane wave off an homogeneous sphere with a diffuse surface (Born approximation). The solid line corresponds to an exact phase shift analysis which was fitted to the experimental data.

Fattori di Forma

Table 5.1. Connection between charge distributions and form factors for some spherically symmetric charge distributions in Born approximation.

Charge distribution $f(r)$		Form Factor $F(\boldsymbol{q}^2)$	
point	$\delta(r)/4\pi$	1	constant
exponential	$(a^3/8\pi)\cdot\exp(-ar)$	$\left(1+\boldsymbol{q}^2/a^2\hbar^2\right)^{-2}$	dipole
Gaussian	$\left(a^2/2\pi\right)^{3/2}\cdot\exp\left(-a^2r^2/2\right)$	$\exp\left(-\boldsymbol{q}^2/2a^2\hbar^2\right)$	Gaussian
homogeneous sphere	$\begin{cases} 3/4\pi R^3 & \text{for } r\le R \\ 0 & \text{for } r>R \end{cases}$	$3\,\alpha^{-3}(\sin\alpha-\alpha\cos\alpha)$ with $\alpha=\lvert\boldsymbol{q}\rvert R/\hbar$	oscillating

Fattori di Forma

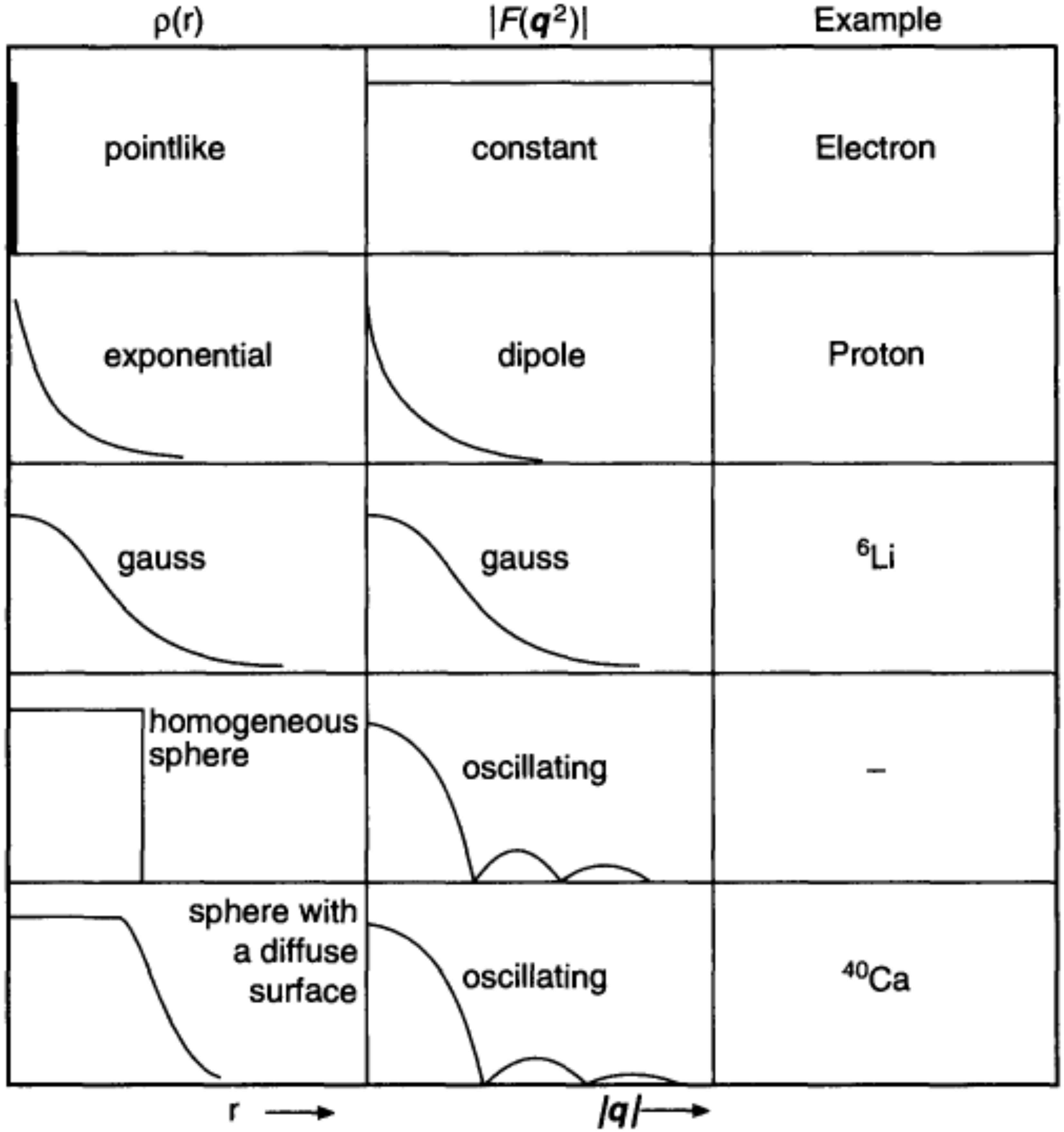

Fattori di Forma

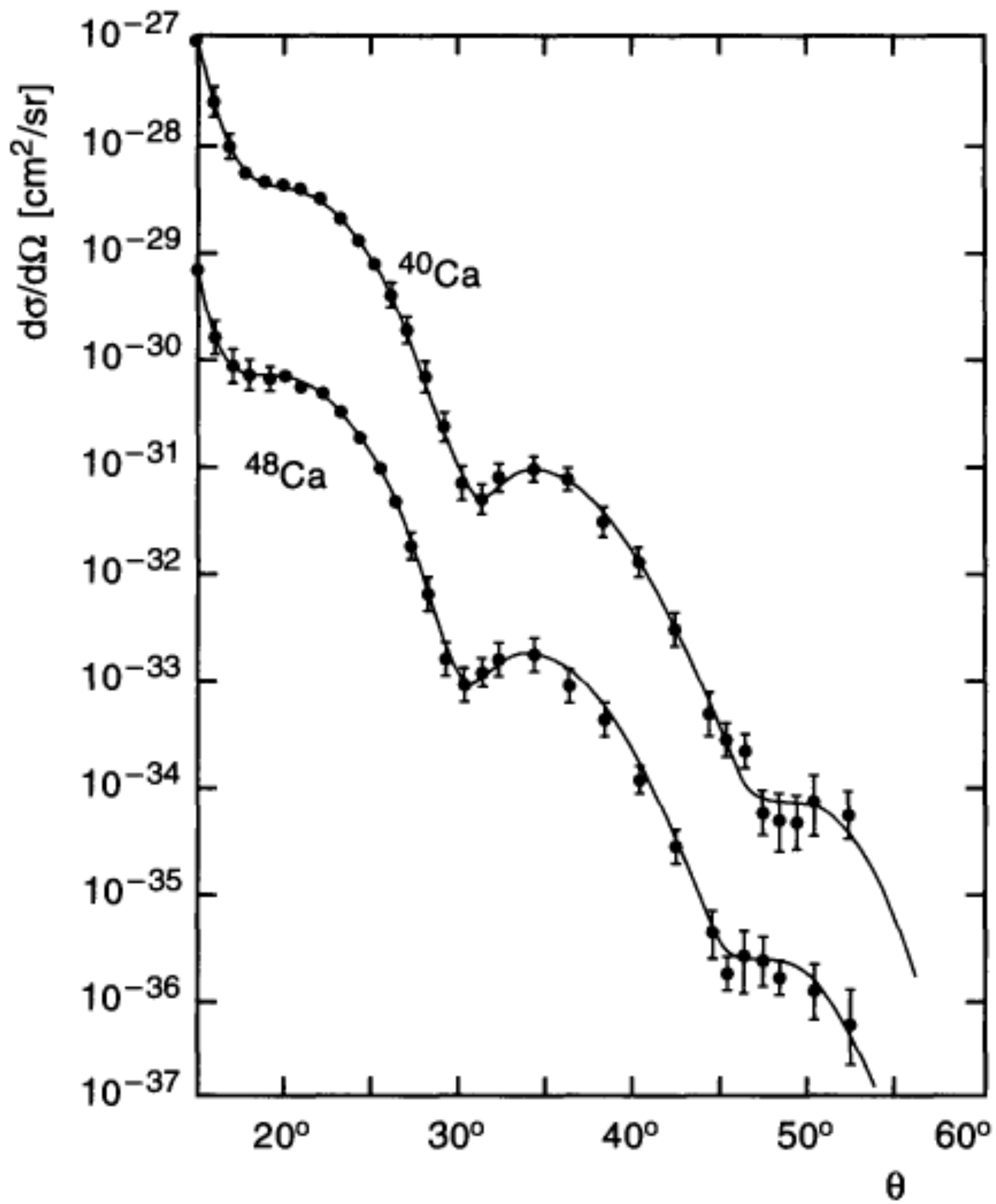

Fig. 5.7. Differential cross-sections for electron scattering off the calcium isotopes ^{40}Ca and ^{48}Ca [Be67]. For clarity, the cross-sections of ^{40}Ca and ^{48}Ca have been multiplied by factors of 10 and 10^{-1}, respectively. The solid lines are the charge distributions obtained from a fit to the data. The location of the minima shows that the radius of ^{48}Ca is larger than that of ^{40}Ca.

Fattori di Forma

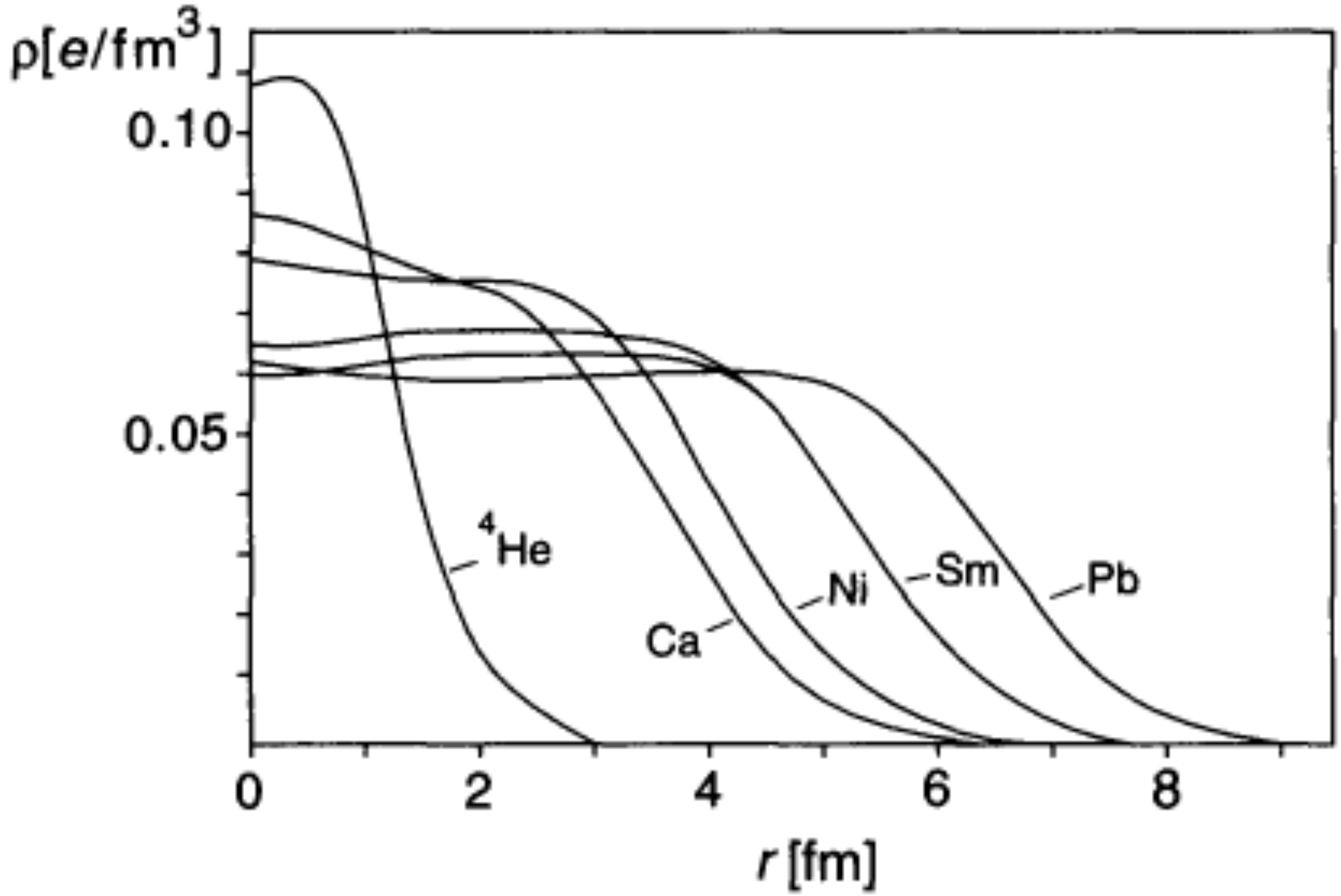

Fig. 5.8. Radial charge distributions of various nuclei. These charge distributions can be approximately described by the Fermi distribution (5.52), i. e., as spheres with diffuse surfaces.

Fattori di Forma

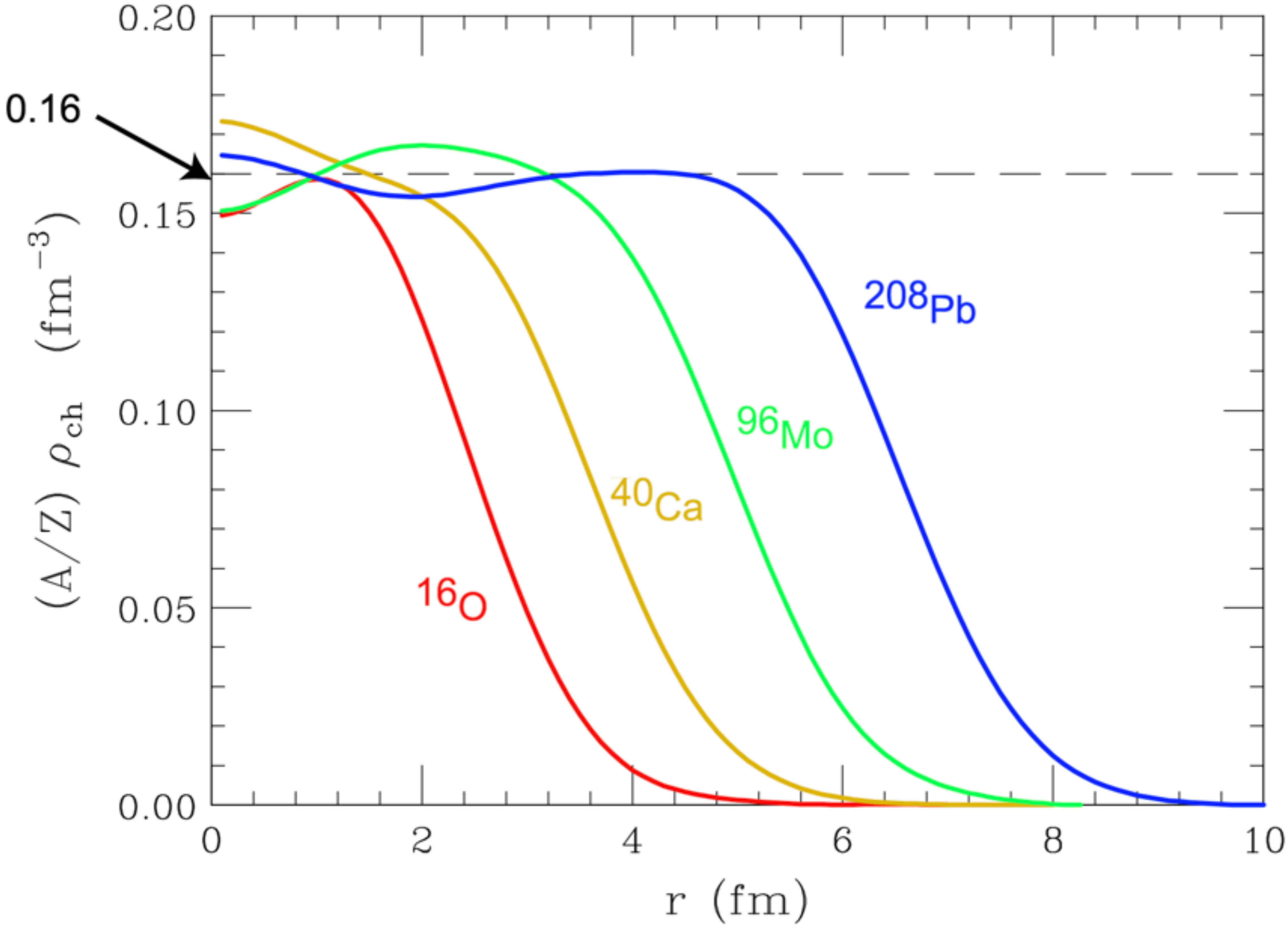

Nuclei stabili

Fig. 4.1 The stable odd-A nuclei. Each dot represents a stable nucleus plotted with coordinates (Z,N). We shall show in Section 5.4 that there is only one stable isobar for each value of A for nuclei with odd A and therefore this plot is particularly simple. It demonstrates the increase in the number of neutrons relative to the number of protons as A increases. The same increase occurs for even-A nuclei but since many such A have two stable isobars (and three in a few cases) the figure would be very much more crowded with dots if these nuclei were included in the plot. These extra dots would crowd around the line of dots for the odd-A nuclei. The line which passes through the average position of the dots on the Z,N plane is called the **line of stability**.

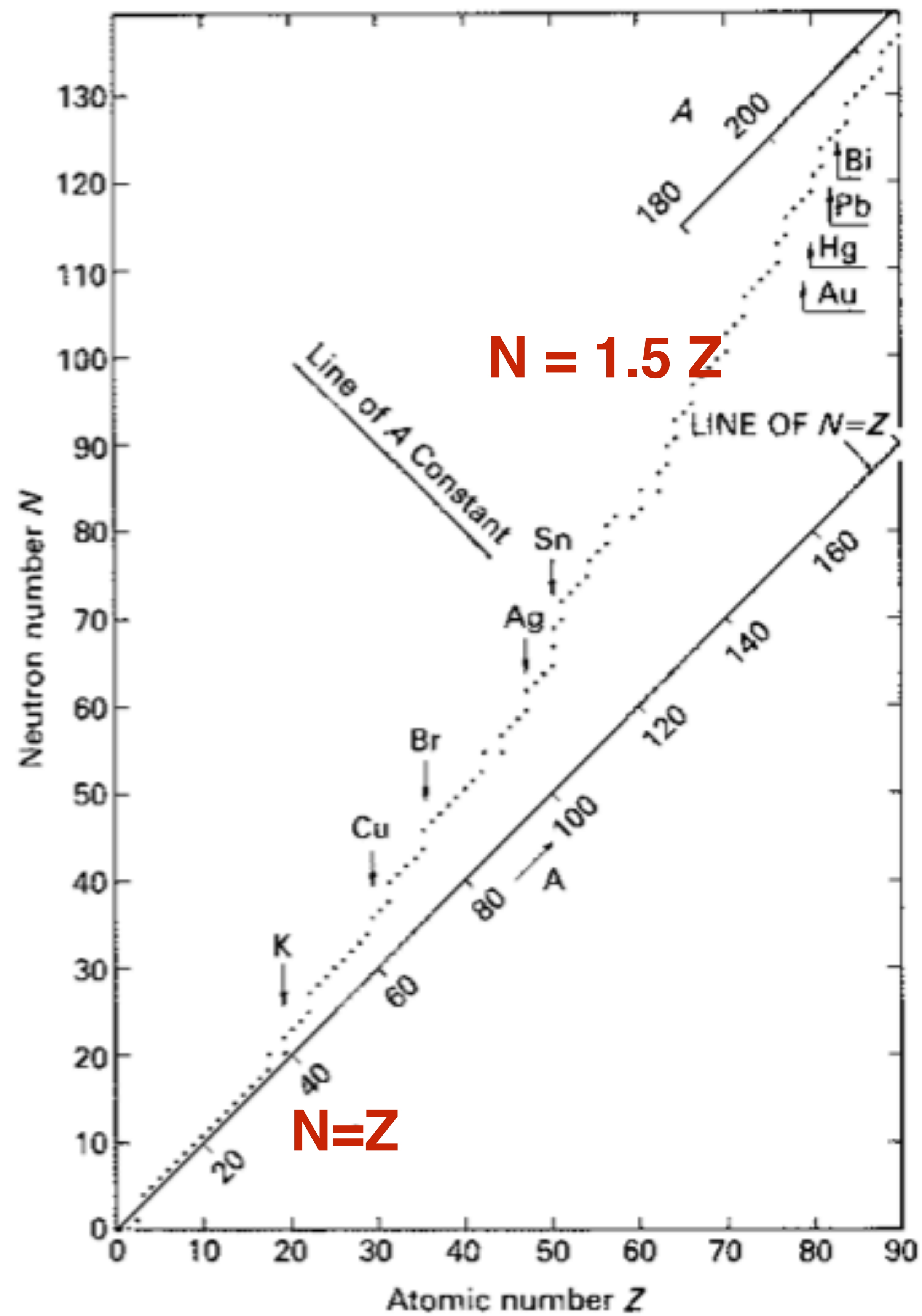

Spettrometro di massa

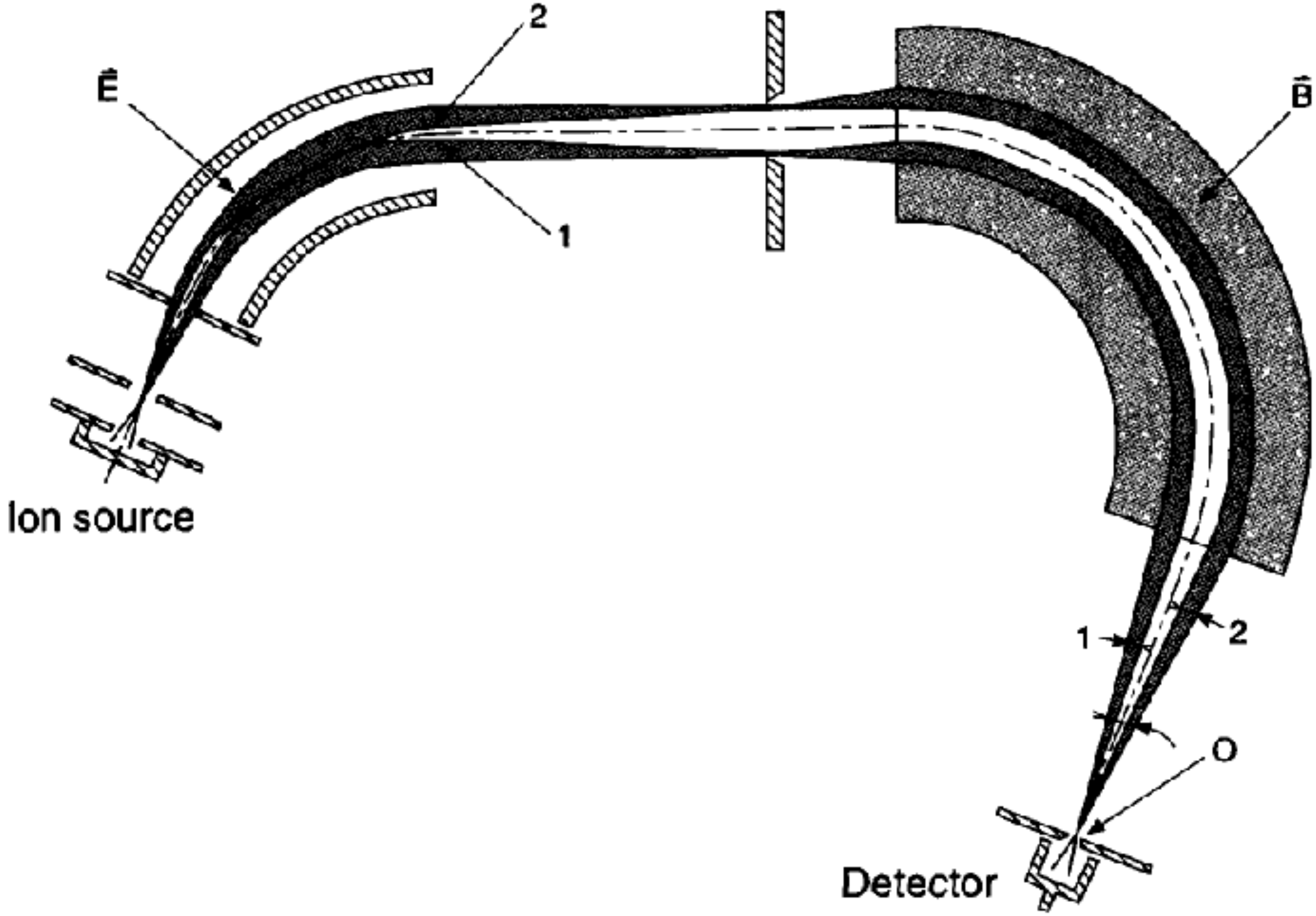

Fig. 2.1. Doubly focusing mass spectrometer [Br64]. The spectrometer focuses ions of a certain specific charge to mass ratio Q/M. For clarity, only the trajectories of particles at the edges of the beam are drawn (*1 and 2*). The electric and magnetic sector fields draw the ions from the ion source into the collector. Ions with a different Q/M ratio are separated from the beam in the magnetic field and do not pass through the slit O.

Abbondanze isotopiche dei nuclidi

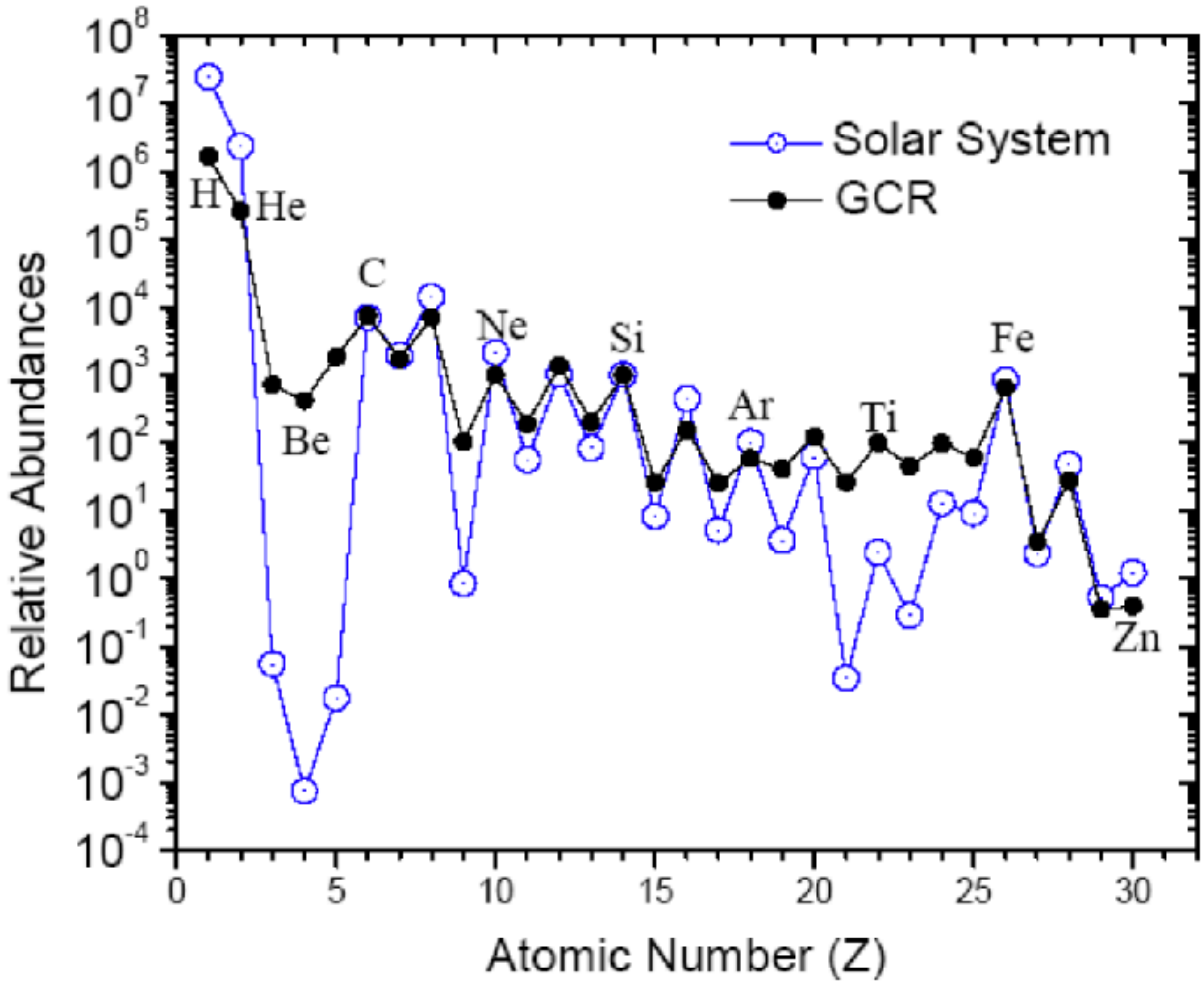

Binding energy

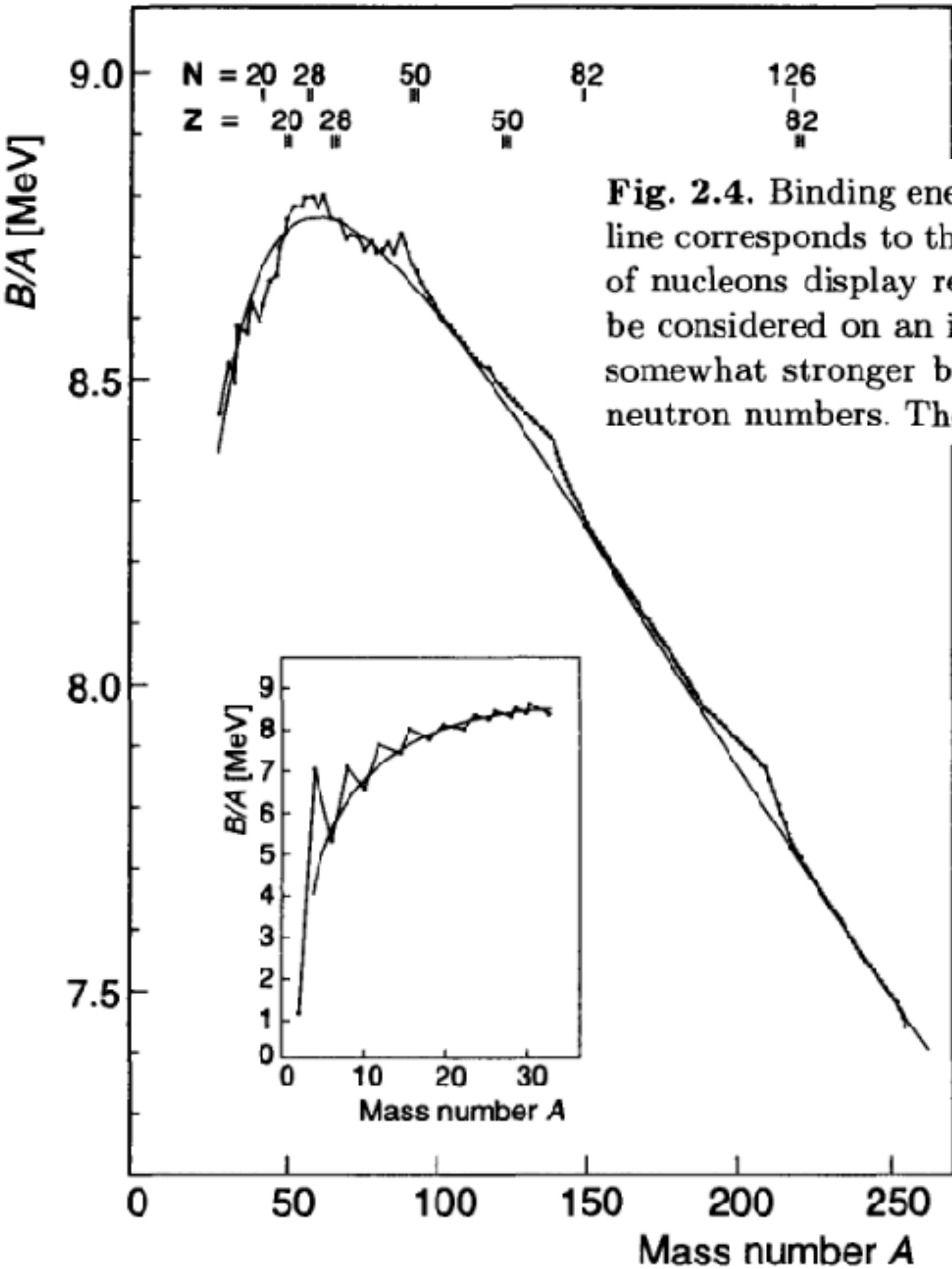

Fig. 2.4. Binding energy per nucleon of nuclei with even mass number A. The solid line corresponds to the Weizsäcker mass formula (2.8). Nuclei with a small number of nucleons display relatively large deviations from the general trend, and should be considered on an individual basis. For heavy nuclei deviations in the form of a somewhat stronger binding per nucleon are also observed for certain proton and neutron numbers. These so-called "magic numbers" will be discussed in Sect. 17.3.

Stabilità dei nuclei

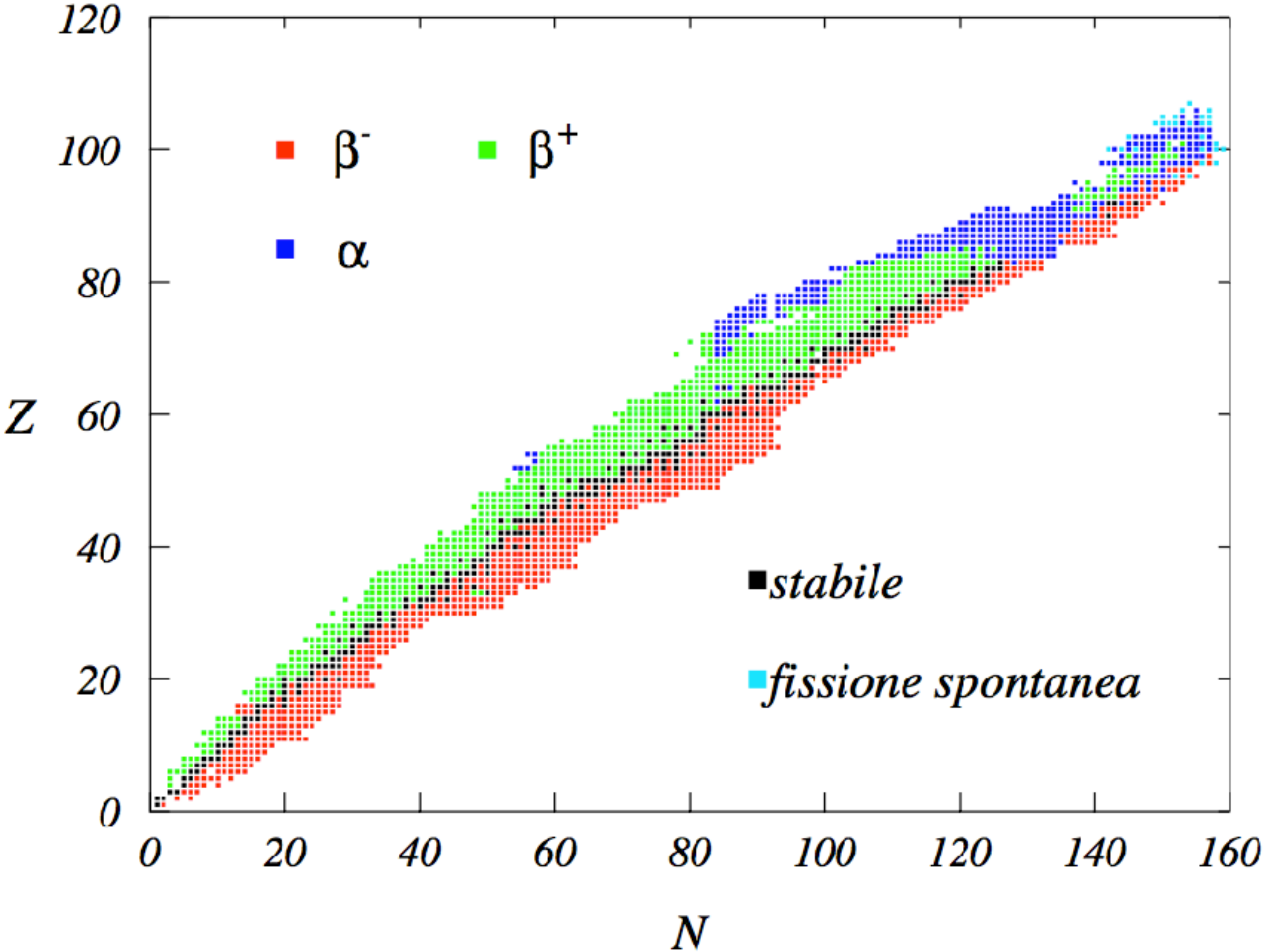

Decadimento β

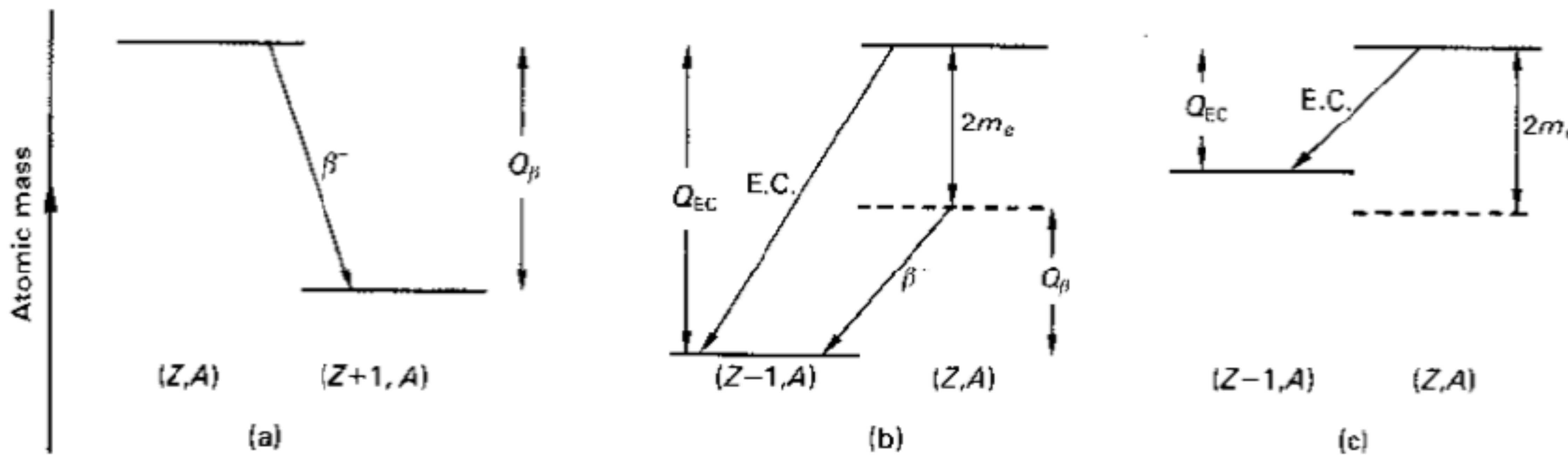

Fig. 5.5 The energy-level diagrams for β^-- β^+-decays and for electron capture (E.C.). Here it is most convenient to use a vertical scale which gives the atomic masses of the levels involved. In (a) the parent level has to be above the level of the daughter for β-decay to be possible, the level difference, Q_β, being the energy available to share among the products as kinetic energy, which, neglecting nuclear recoil, will be the maximum kinetic energy the electron can have. In (b) electron capture can occur and the mass difference (Q_{EC}) goes into total energy of the neutrino and recoil of the daughter atom (branch labelled E.C.). For β^+-decay to occur the mass difference must be greater than $2m_e$; what is left is available for kinetic energy (Q_β). This situation is represented by the right-hand branch of (b), labelled β^+. For an atomic mass difference less than $2m_e$, β^+-decay is impossible and only electron capture can occur, as shown in (c).

Decadimento β

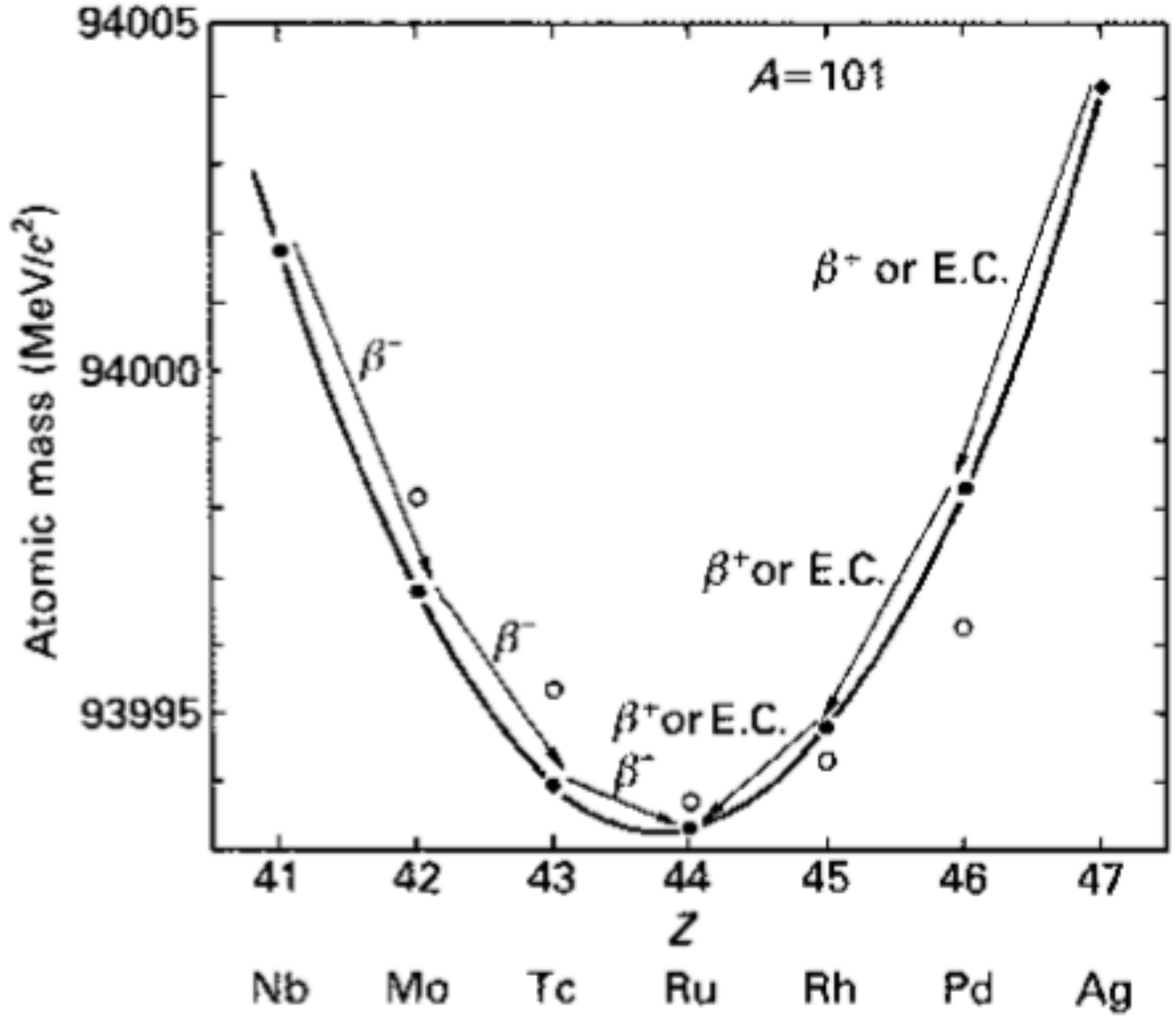

Fig. 5.6 The atomic mass of the isobars of $A = 101$ as a function of Z in the region of the line of stability. The solid points are calculated using the semi-empirical mass formula (Table 4.2); the line drawn through the points has no physical significance. The energy changes in β-decay given in Table 5.1 permit the transitions indicated so that the lowest atomic mass is thereby expected to be the only stable isobar, ruthenium in this case. This is the situation in all odd-A nuclei and the conclusion is that there is only one stable isobar for odd-A nuclei. The actual atomic masses are given by open points: the conclusion is the same. However, it is clear that even the relatively small errors in the result of the semi-empirical mass formula may not permit, in all cases, a prediction of which Z has the lowest atomic mass at the bottom of a shallow curve. For the real nuclei the transition from $A = 45$ to $A = 44$ can occur only by electron capture.

Decadimento β

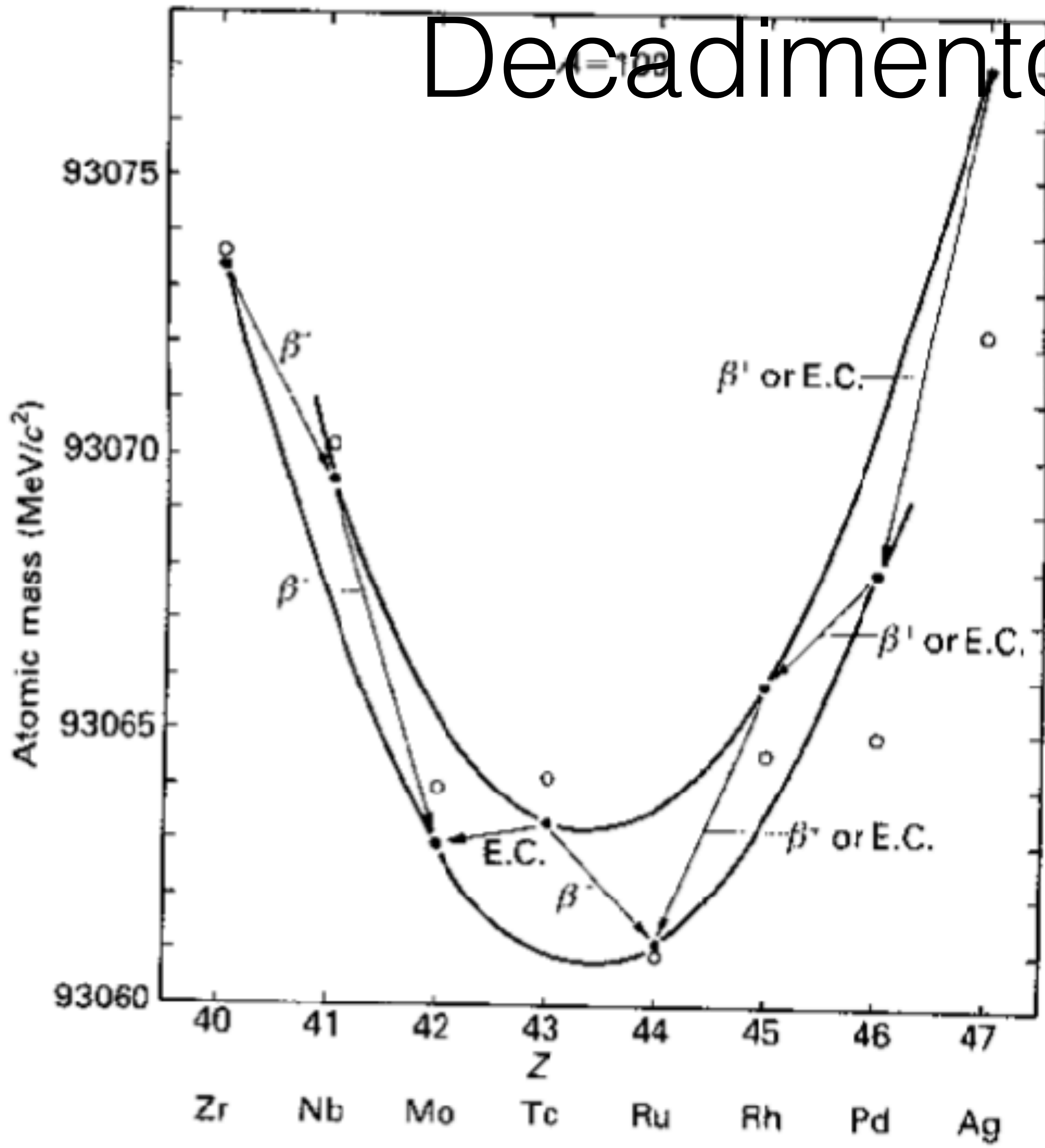

Fig. 5.7 The atomic mass of the isobars of $A = 100$ as a function of Z in the region of the line of stability. The solid points are calculated using the semi-empirical mass formula (Table 4.2). The pairing term contributes an opposite amount to the even- and odd-Z masses with the result that alternate mass points lie on different parabolae. The energy changes in β-decay given in Table 5.1 predict that the transitions indicated will occur and that molybdenum and ruthenium will be stable. As in Fig. 5.6 the actual masses are indicated by the open points. The conclusions are not changed in this case. The general conclusion is that even-A nuclei can have two or more stable isobars.

Decadimento β

Fig. 5.8 The energy levels involved in the decay of the oo nucleus $^{40}_{19}K$ (potassium). This is an example of a nuclide with a trimodal decay: β^+, β^-, and electron capture.

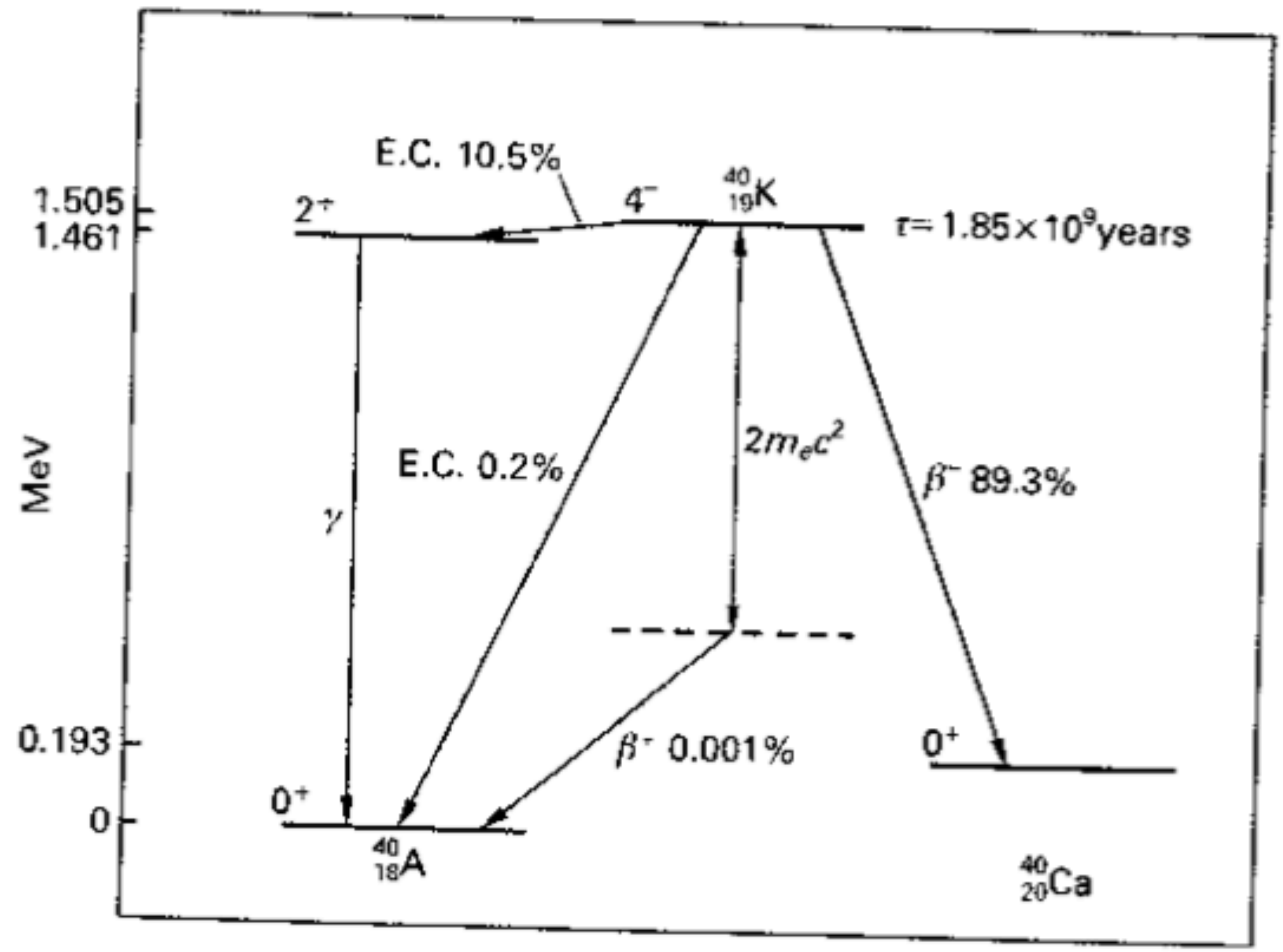

Table 5.2 The decay steps for the naturally occurring radioactive series with A(modulo 4)=2. Of particular interest are the α-decay Q_α-values and the mean lives. There is clearly a strong correlation between increasing Q_α and decreasing mean life.

A	Decay series A (modulo 4)=2	Q_α (MeV)	Mean life†
238	$_{92}U \xrightarrow{\alpha}$	4.27	6.45×10^9y
234	$_{90}Th \xrightarrow{\beta^-} {}_{91}Pa \xrightarrow{\beta^-} {}_{92}U$		
	$_{92}U \xrightarrow{\alpha}$	4.86	3.53×10^5y
230	$_{90}Th \xrightarrow{\alpha}$	4.77	1.12×10^5y
226	$_{88}Ra \xrightarrow{\alpha}$	4.87	2.31×10^3y
222	$_{86}Rn \xrightarrow{\alpha}$	5.59	5.51 d
218	$_{84}Po \xrightarrow{\alpha}$	6.11	4.40 m
214	$_{82}Pb \xrightarrow{\beta^-} {}_{83}Bi \xrightarrow{\beta^-} {}_{84}Po$		
	$_{83}Bi \xrightarrow{\alpha}$ (a)	(a) 5.62	94 d
	$_{84}Po \xrightarrow{\alpha}$ (b)	(b) 7.83	2.37×10^{-4}s
210	$_{81}Tl \xrightarrow{\beta^-} {}_{82}Pb \xrightarrow{\beta^-} {}_{83}Bi \xrightarrow{\beta} {}_{84}Po$		
	$_{84}Po \xrightarrow{\alpha}$	5.41	200 d
206	$_{82}Pb$		

The mean life given for $^{214}_{83}Bi \Rightarrow {}^{210}_{81}Tl + \alpha$ is the reciprocal of the transition rate for this particular decay. The decay of this nuclide is bimodal so that its actual mean life is less than this value due to the effect of the competition from the β^--decay mode to $^{214}_{84}Po$.

† y=years, d=days, m=minutes, s=seconds.

Decadimento β

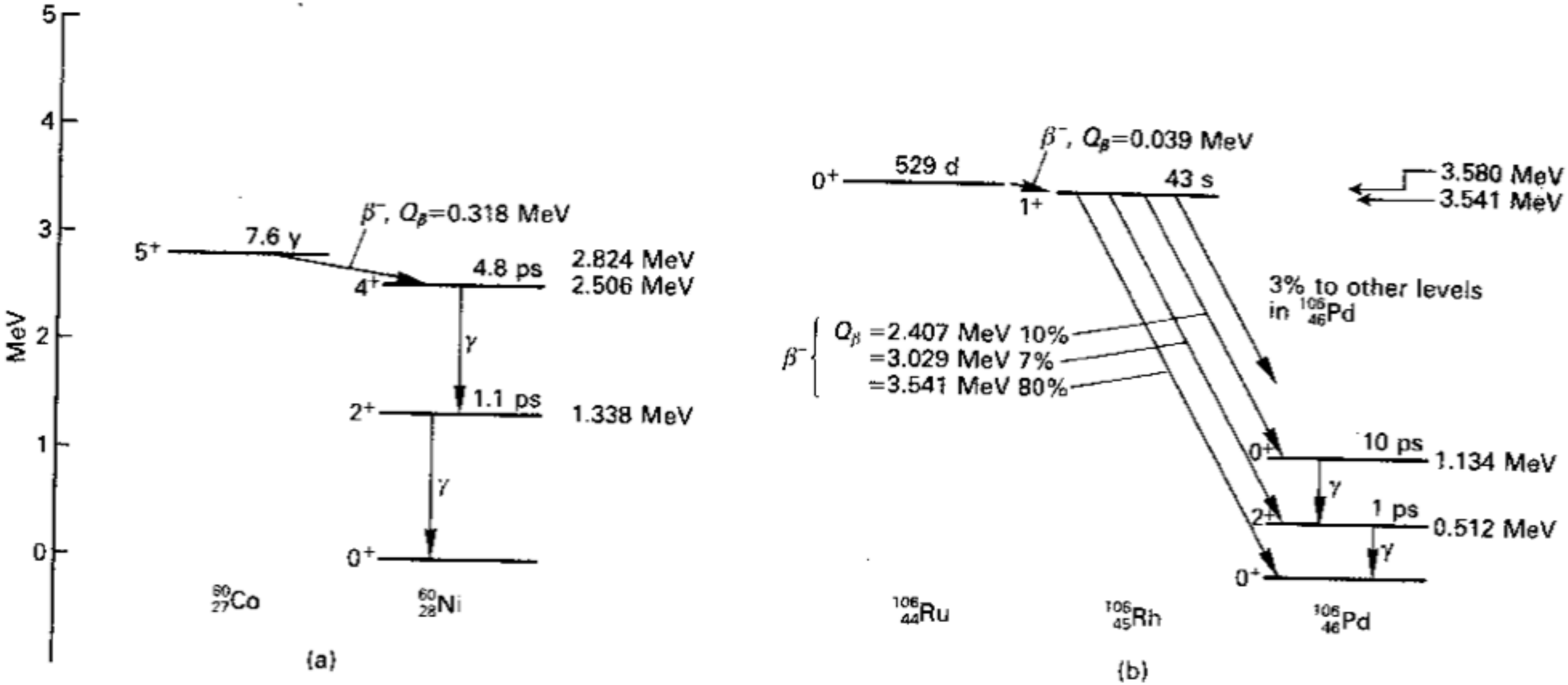

Fig. 5.9 (a) The energy-level diagram for the atomic masses of $^{60}_{27}$Co and $^{60}_{28}$Ni showing the transitions that make the former a source of γ-rays near 1 MeV with a useful life. (b) The energy levels of $^{106}_{44}$Ru, $^{106}_{45}$Rh and $^{106}_{46}$Pd showing the arrangement of levels that makes the first a source of β-particles with kinetic energies up to 3.5 MeV and a useful life. These diagrams show the atomic masses in MeV above the lowest mass in each case. The symbol 'y' stands for years and 'd' for days: ps is the SI system picosecond = 10^{-12} seconds.

Decadimento alpha

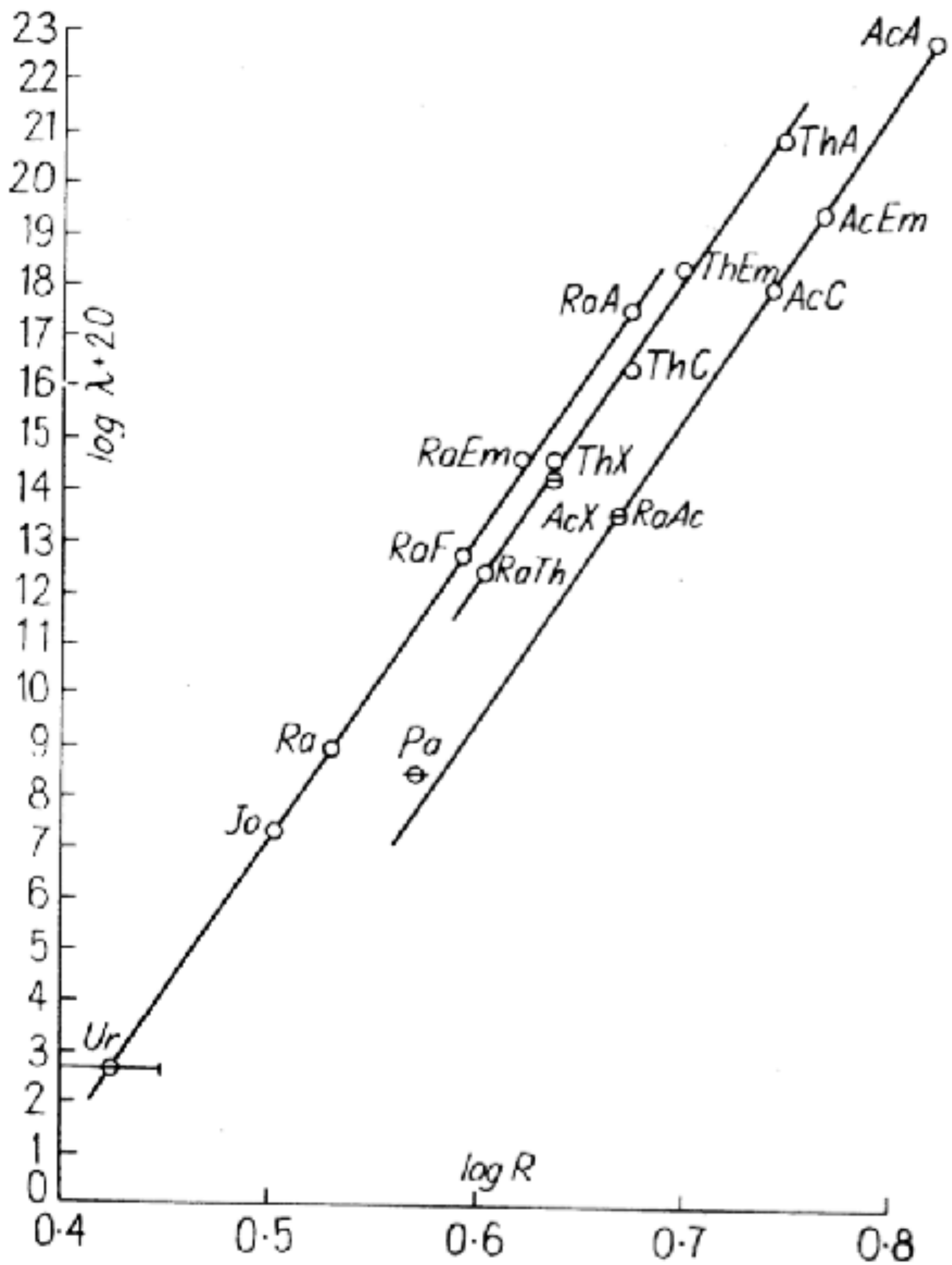

Diagramma di Geiger e Nuttal

Decadimento alpha

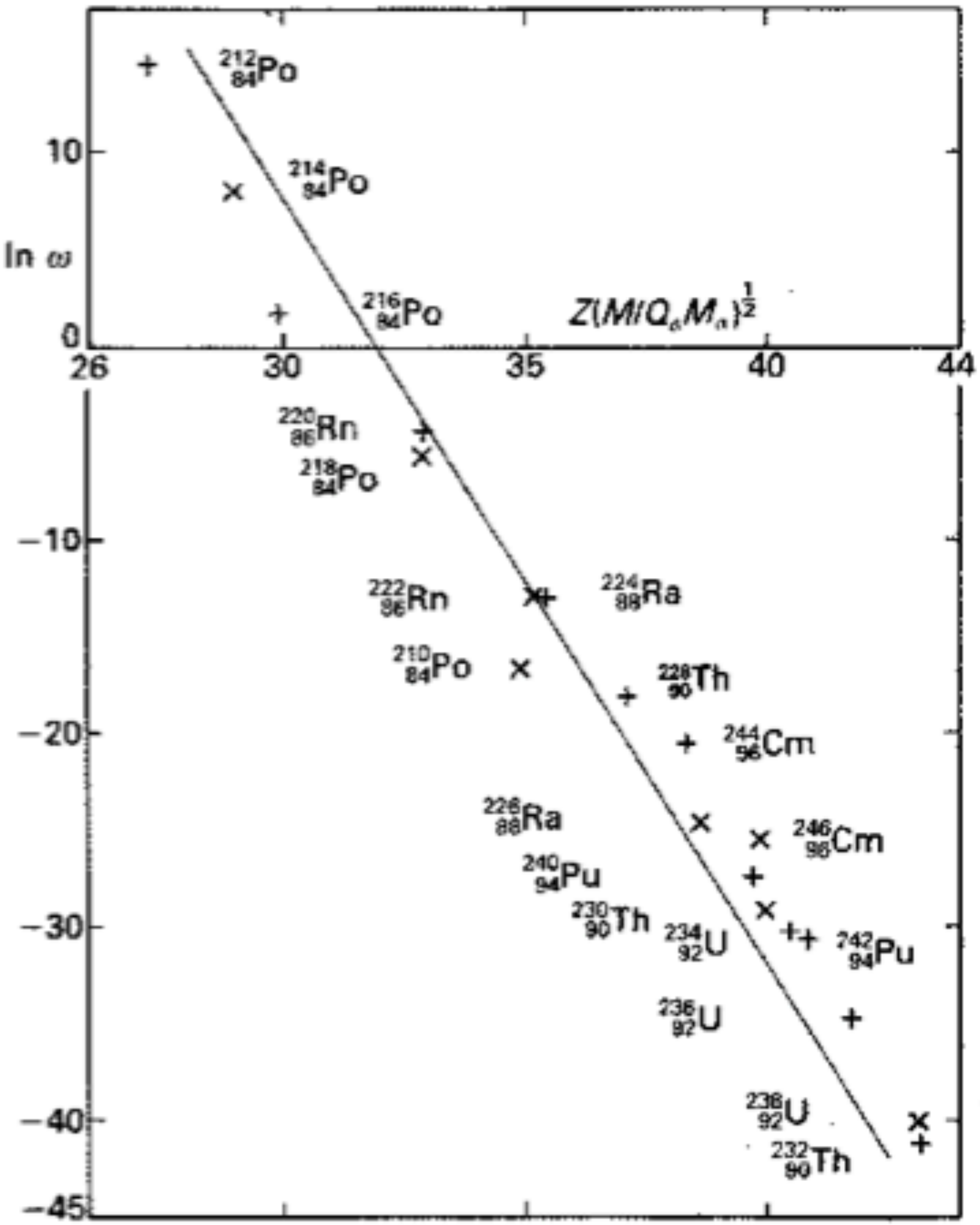

- Spiega abbastanza bene l'andamento su diversi ordini di grandezza
- Th(Z=90,A=232) , $\boldsymbol{\omega}=1.2\cdot 10^{-18}$ s^{-1} e $Q\alpha=4.08$ MeV
- Po(Z=84,A=212): $\boldsymbol{\omega}=2.3\cdot 10^{6}$ s^{-1} e $Q\alpha=8.95$ MeV
- Per Z=80 e $Q\alpha<3$ MeV la vita media > tempo dell'Universo. Il decadimento pur essendo energicamente possibile e' inosservabile

Modello a Shell

Potenziali di prima ionizzazione

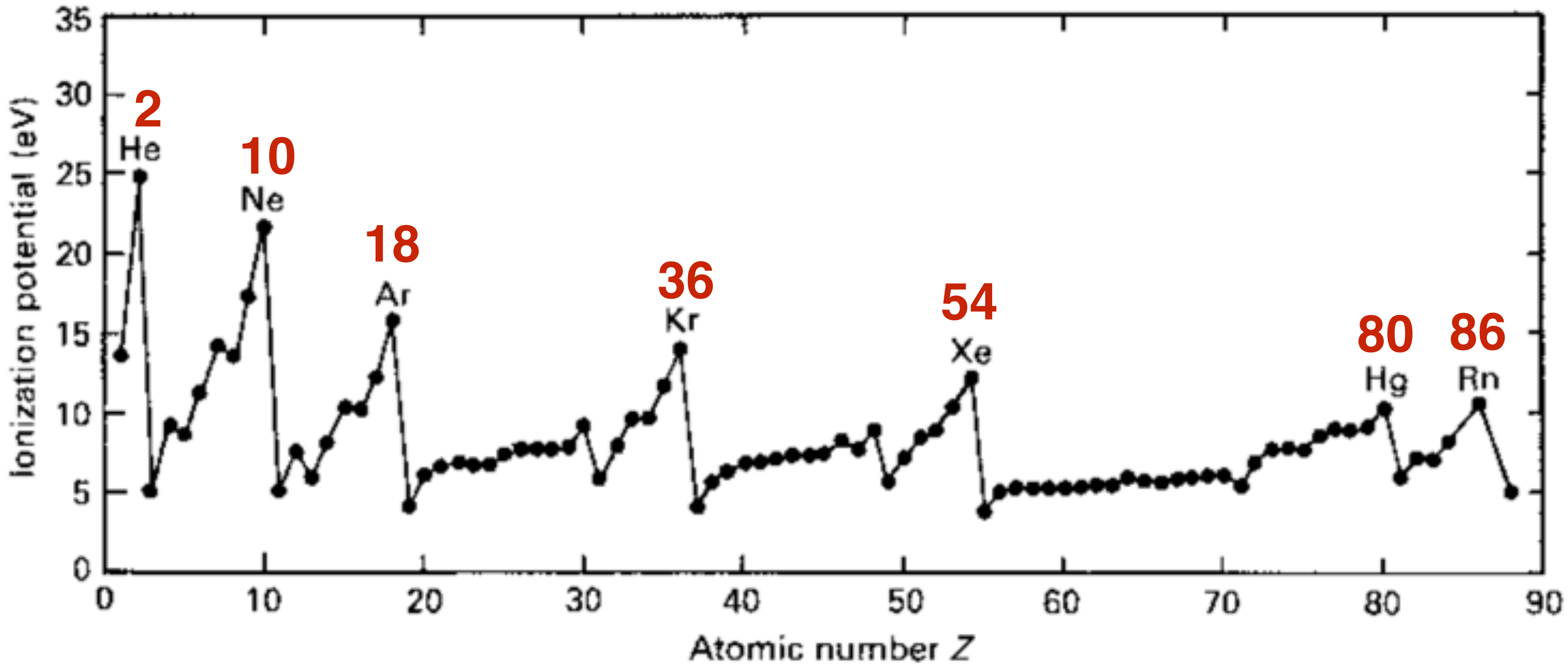

Fig. 8.1 The first ionization potential (electron separation energy) against atomic number for the elements. The well-known 'magic numbers' are $Z=2$, 10, 18, 36, 54, 80, 86. Helium is the element for which two electrons fill the $1s$ level: mercury at $Z=80$ is the element for which the last two electrons fill the $6s$ level. The remainder are the other noble gases for which electrons fill the levels so that the configuration of the last eight electrons is $(ns)^2(np)^6$, $n=2, \ldots\ldots 6$. The occurrence of magic numbers in neutron and proton separation energies for nuclei is one of the pieces of evidence which pointed the way to the nuclear shell model.

Modello a Shell

Energie di separazione

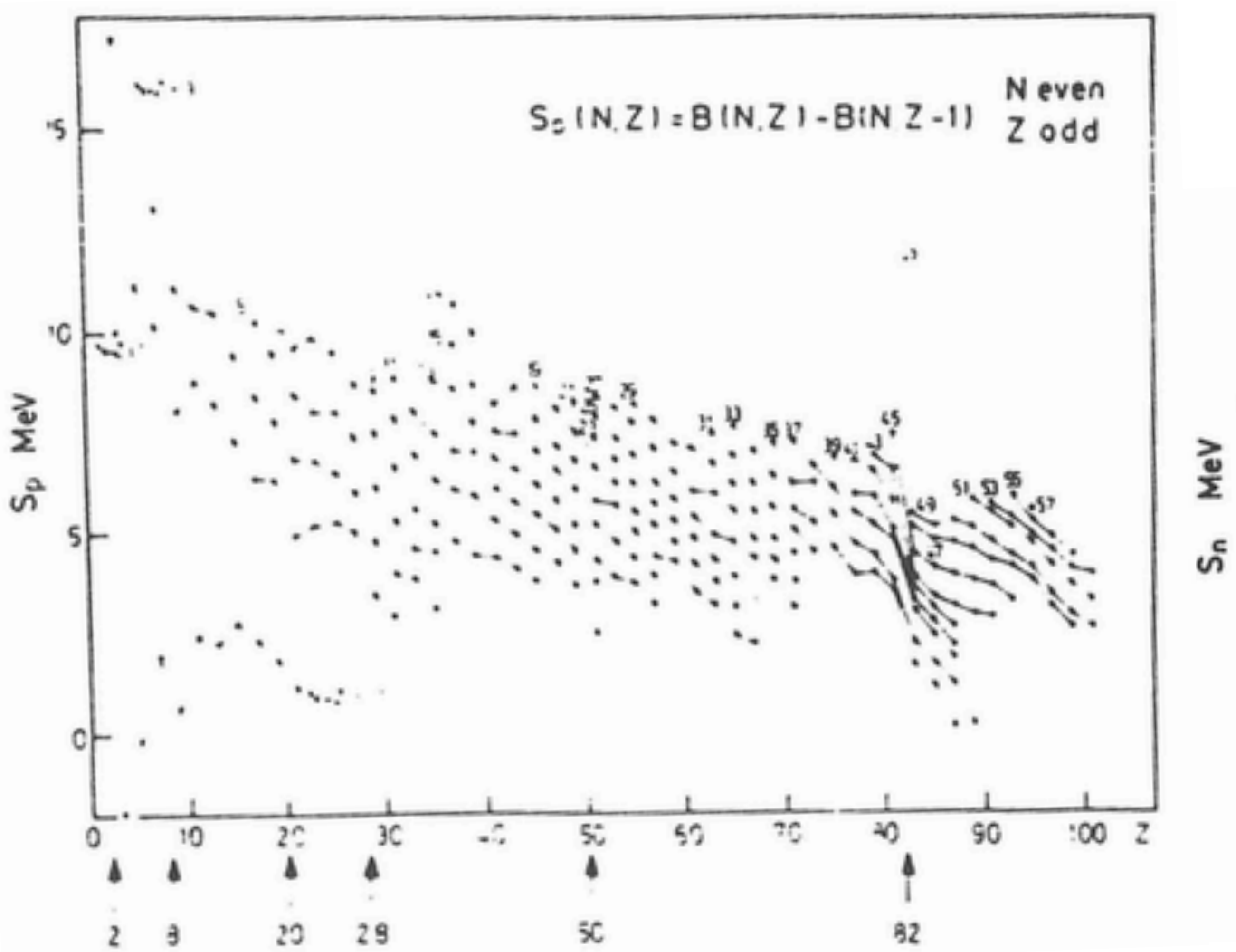

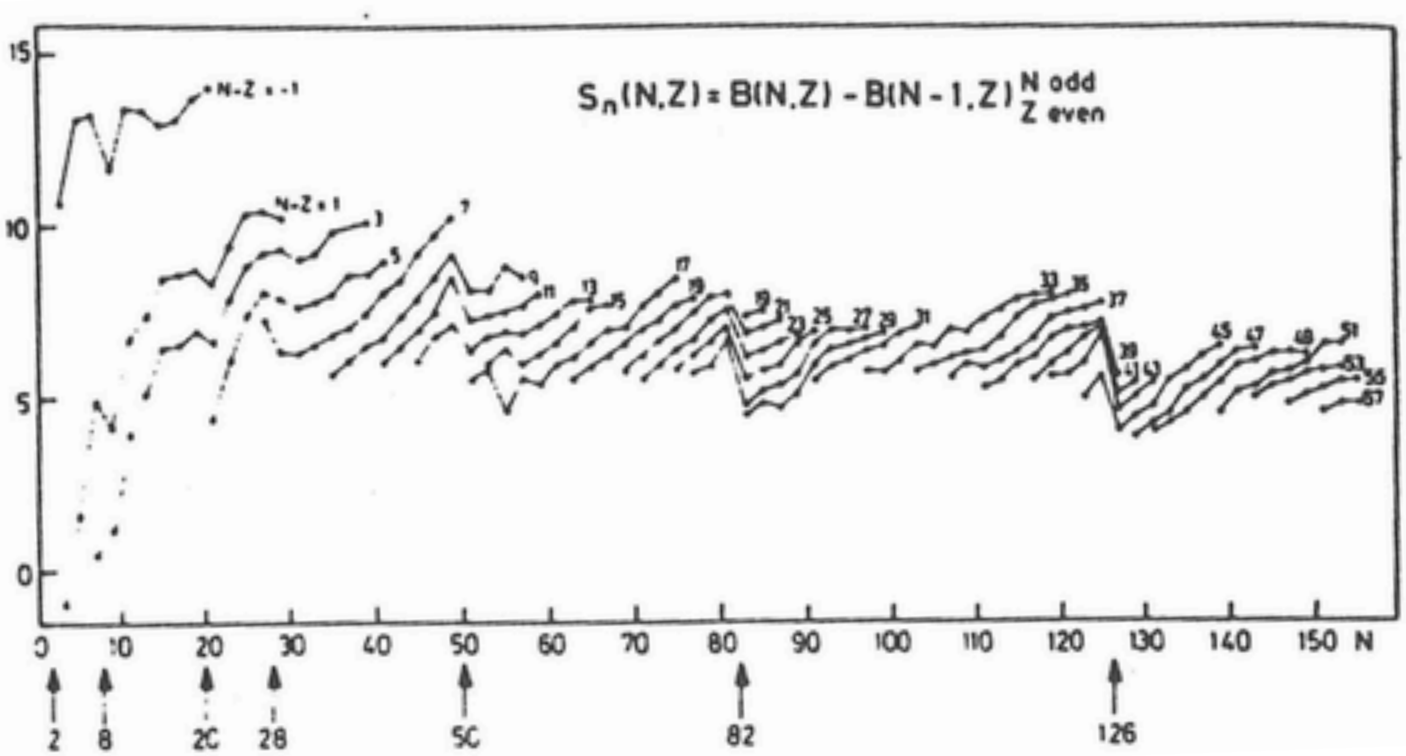

Figura 7.5 Energie di separazione per neutroni (Right) e protoni (Left) in nuclei pari–dispari. In corrispondenza di numeri magici+1 l'energia di separazione è minima, L'ultimo nucleone spaiato è debolmente legato al nucleo.

Modello a Shell

energie di legame

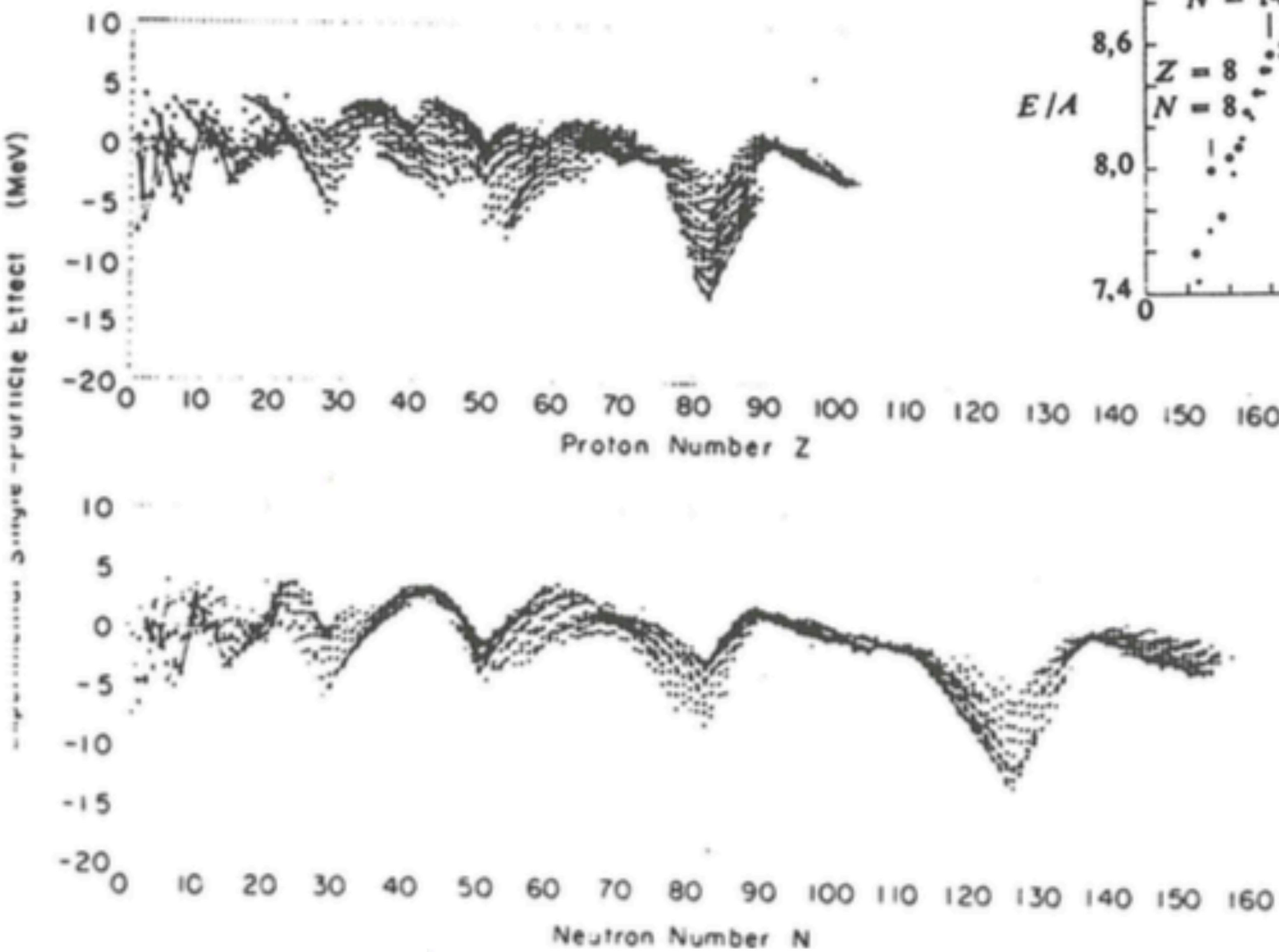

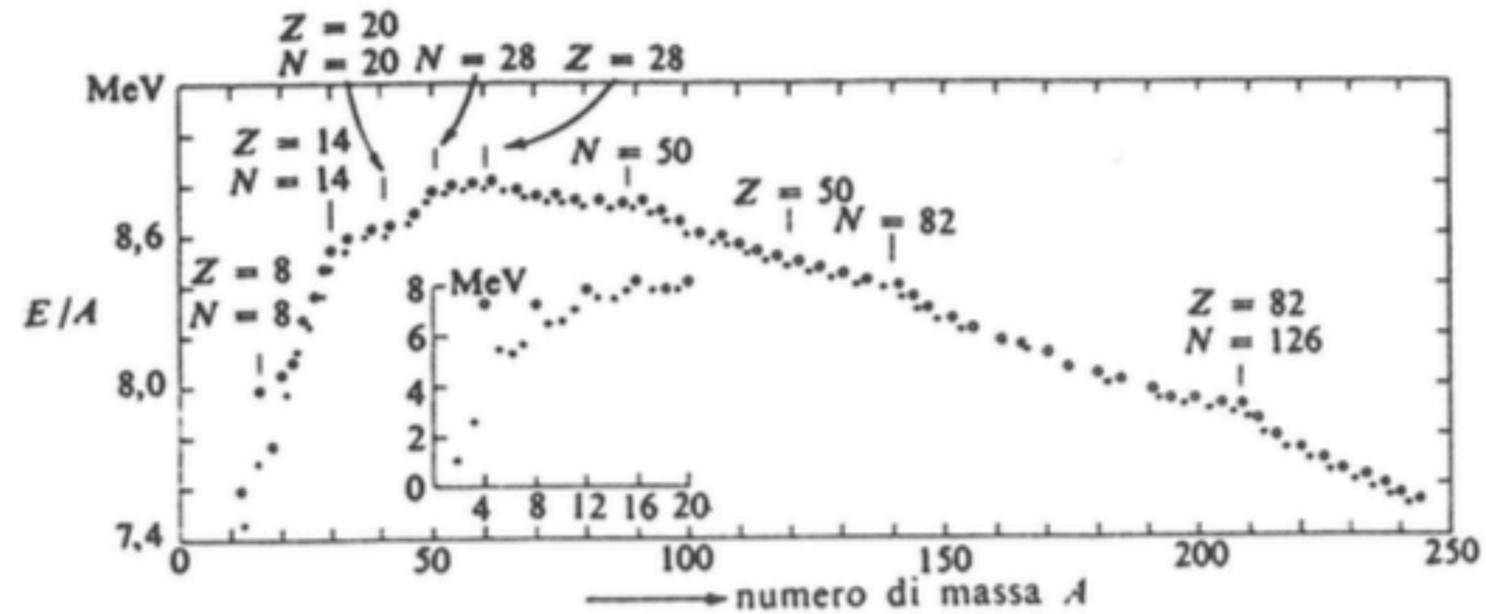

Figura 7.1 Nella figura superiore sono presentate le energie di legame per nucleone e sono evidenziati i valori corrisondenti ai numeri magici. L'effetto di maggior legame di nuclei doppio magici è meglio evidenziato dalla figura inferiore dove sono presentate le deviazioni delle masse nucleari dai valori medi calcolati con la formula semi–empirica della massa. In corrispondenza dei numeri magici ci sono le deviazioni maggiori.

Modello a Shell

Abbondanze Relative

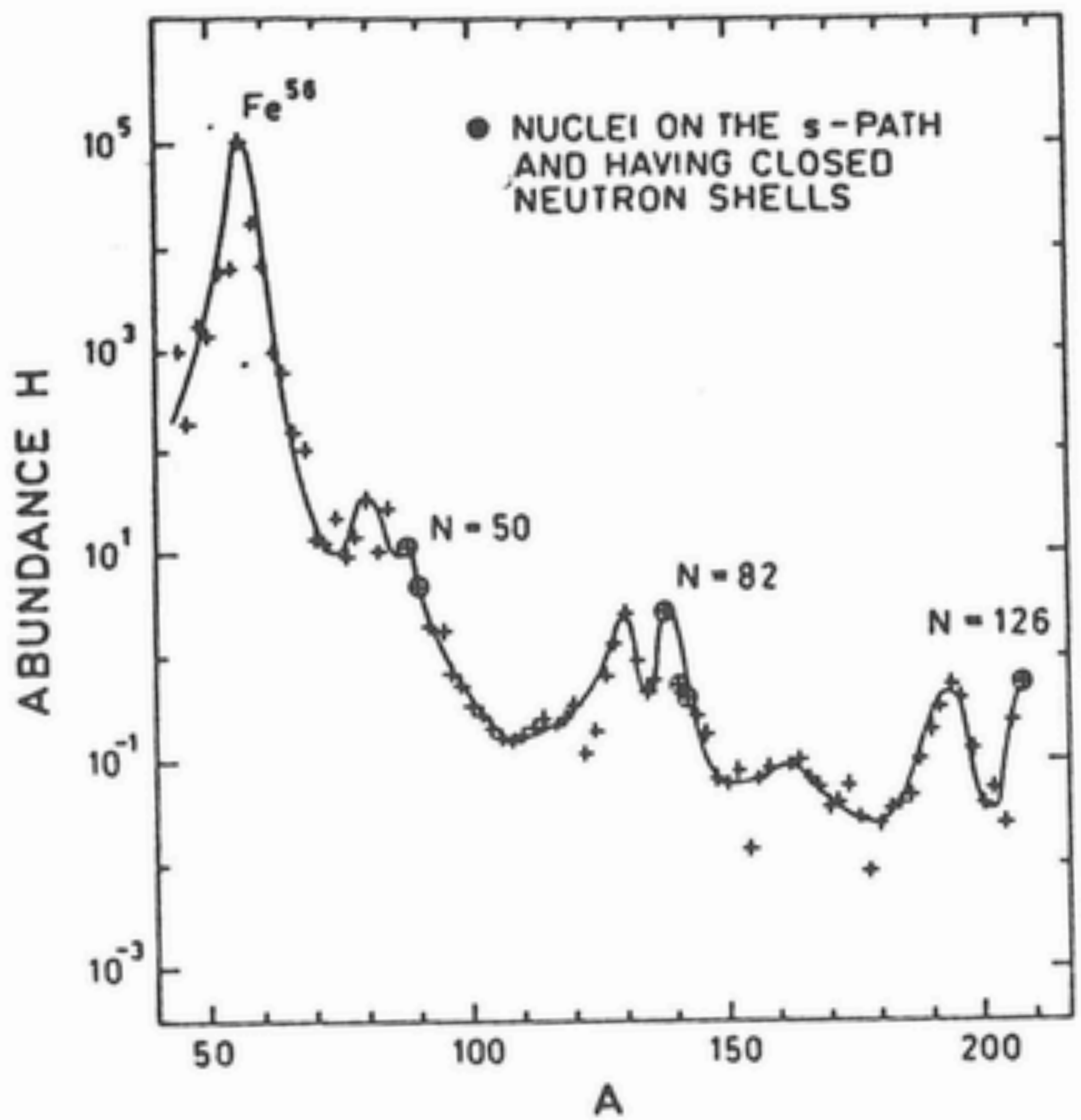

Figura 7.2 L'abbondanza relativa, H, in termini di numero di atomi, per diverse specie di nuclei pari–pari, è presenatata in funzione del numero atomico A ($A > 50$). Sono state utilizzate unità convenzionali in cui le abbondanze sono misurate relativamente al Si ($H(Si) = 10^6$).

Modello a Shell

Sezioni d'urto di cattura di neutroni

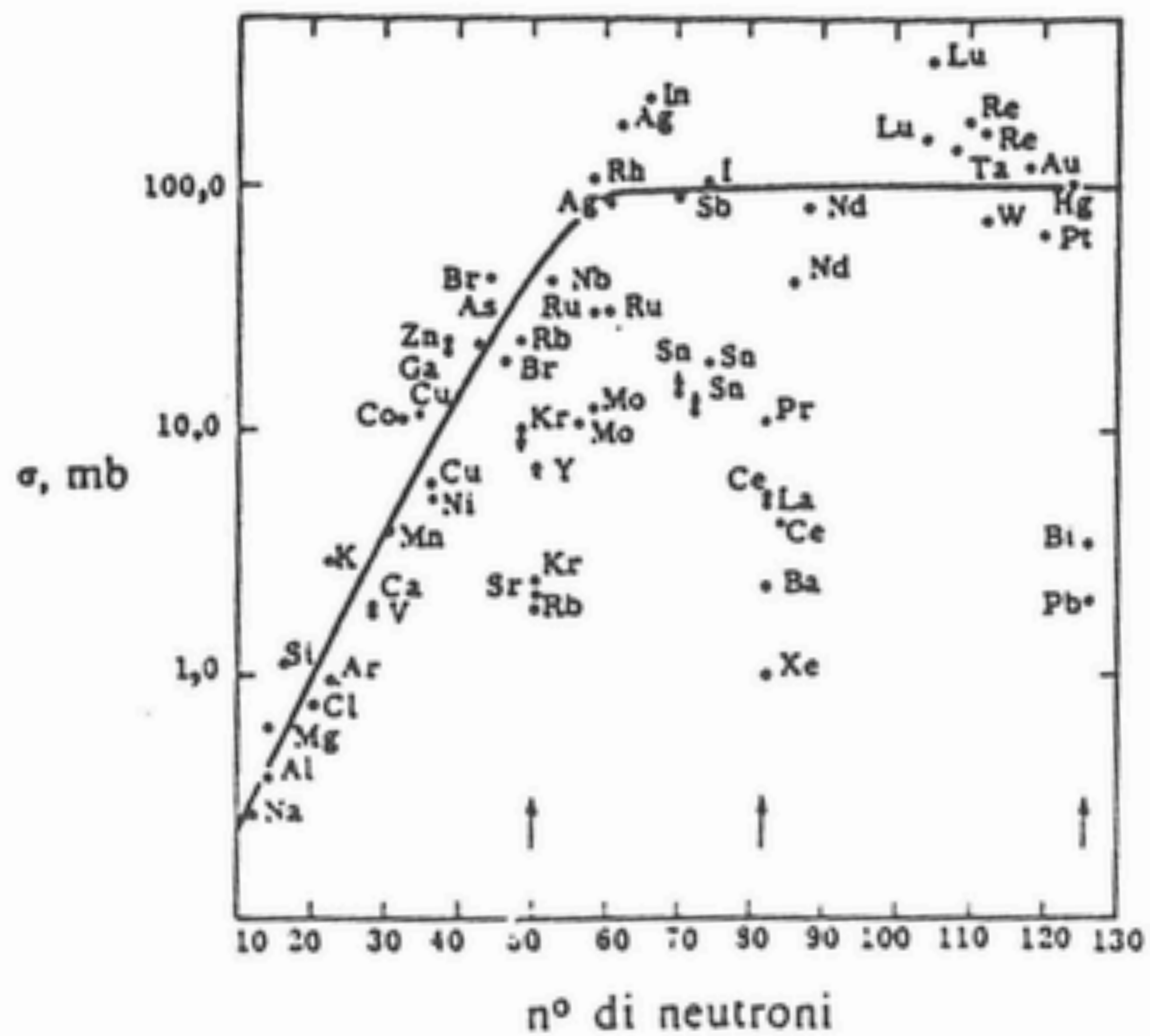

Figura 7.4 Sezione d'urto di cattura di neutroni in funzione del numero di neutroni del nucleo bersaglio. In corrispondenza dei numeri magici c'è una riduzione della sezione d'urto

Modello a Shell

Potenziali

Fig. 8.3 Three spherical potential wells. The harmonic oscillator can be solved analytically and the finite square well has well-understood solutions. However, the Saxon–Woods shape (Section 3.7) provides a more reasonable model for the nuclear potential. By examining the solutions for the harmonic oscillator and for the square well we can obtain a good idea of the level ordering for a realistic nuclear potential.

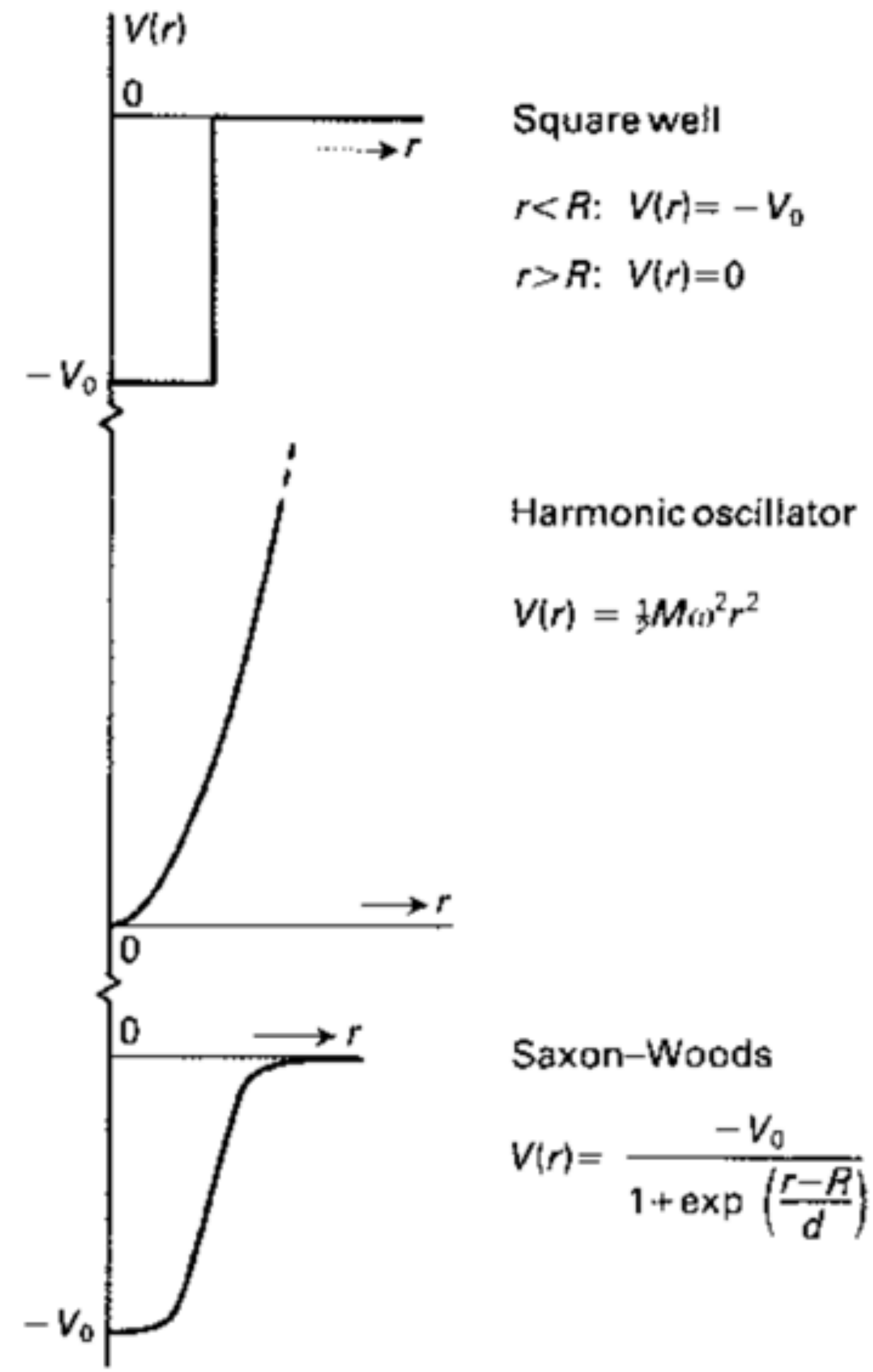

Modello a Shell

Wave Functions

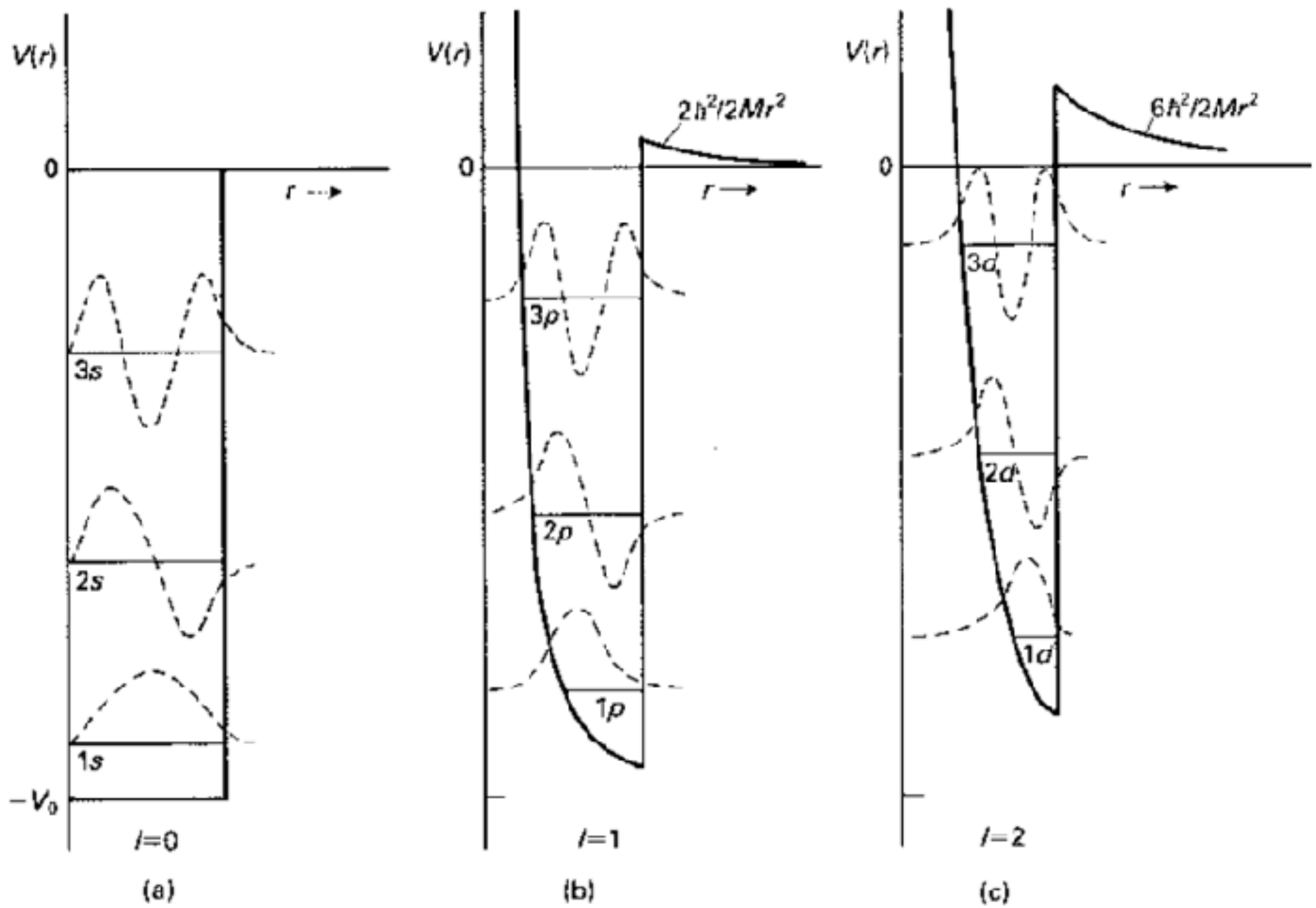

Fig. 8.4 A square-well spherical potential as a function of radius r is shown in (a). It is modified by the angular momentum barrier and the new shapes are given in (b) for $l = 1$ and in (c) for $l = 2$. The single particle energy levels are shown by horizontal lines for the states nl, $n = 1, 2, 3$, and $l = 0, 1, 2$ (s, p, d respectively), where n is the principal quantum number and l is the orbital angular momentum quantum number. The broken line shows the form of $rR(r)$ for the appropriate wavefunction, plotted about its energy level line as zero. Remember that the probability density distribution as a function of radius for the particle is proportional to $(rR(r))^2$.

Modello a Shell

Livelli

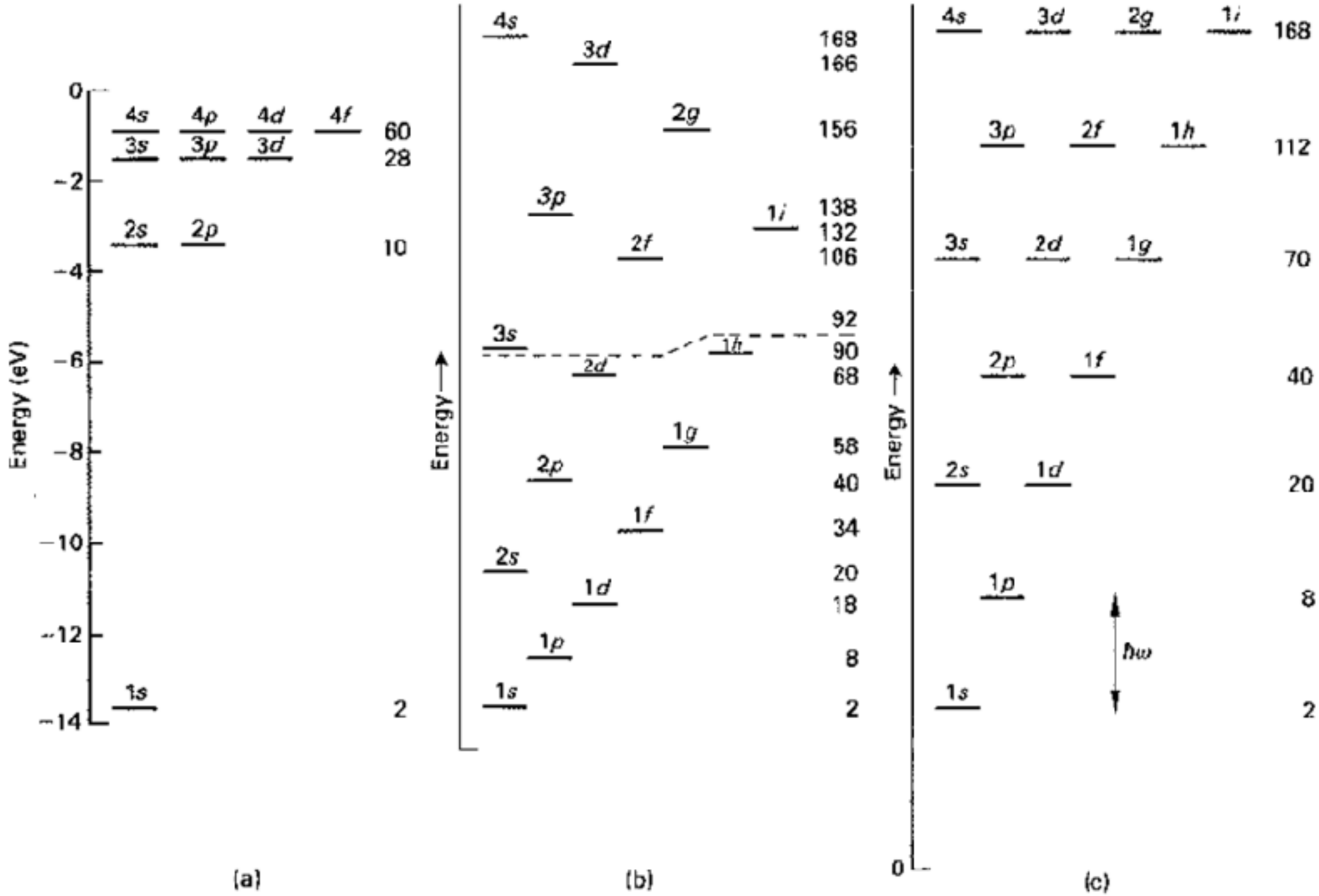

Fig. 8.5 The single-particle energy levels in three spherical potential wells: (a) the Coulomb, (b) the infinite square well, and (c) the harmonic oscillator. In (a) the ordinate gives the actual energies. In (b) and (c) the energy scale is arbitrary but the relative energies above zero at the well bottom in each case are shown correctly. On the right of each we show the accumulated occupancy starting with the 1s level and working upwards in energy. The magic numbers 2, 8, 20 occur for (b) and (c).

Modello a Shell

Livelli e Numeri Magici

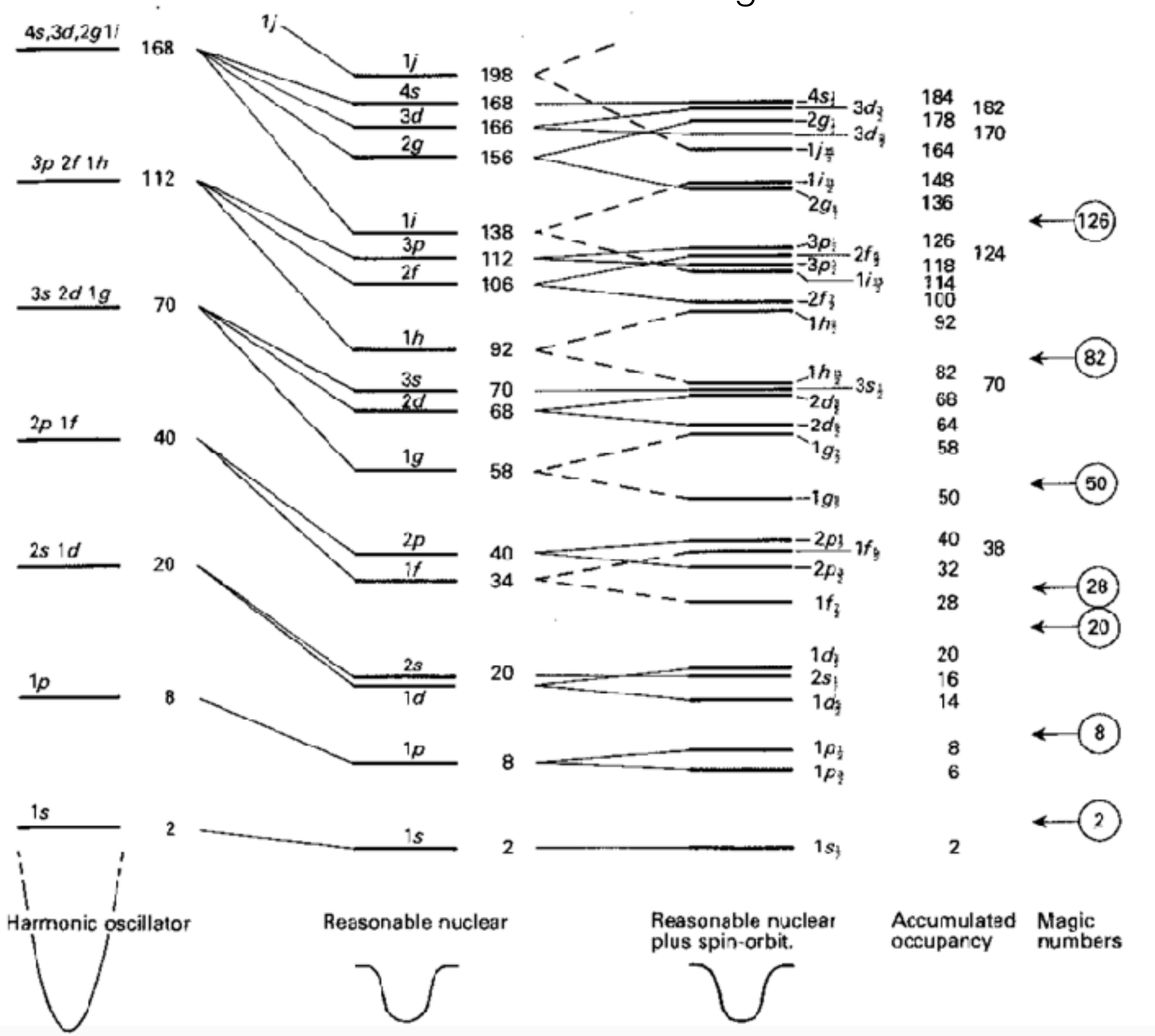

Modello a Shell

Spin Nucleari

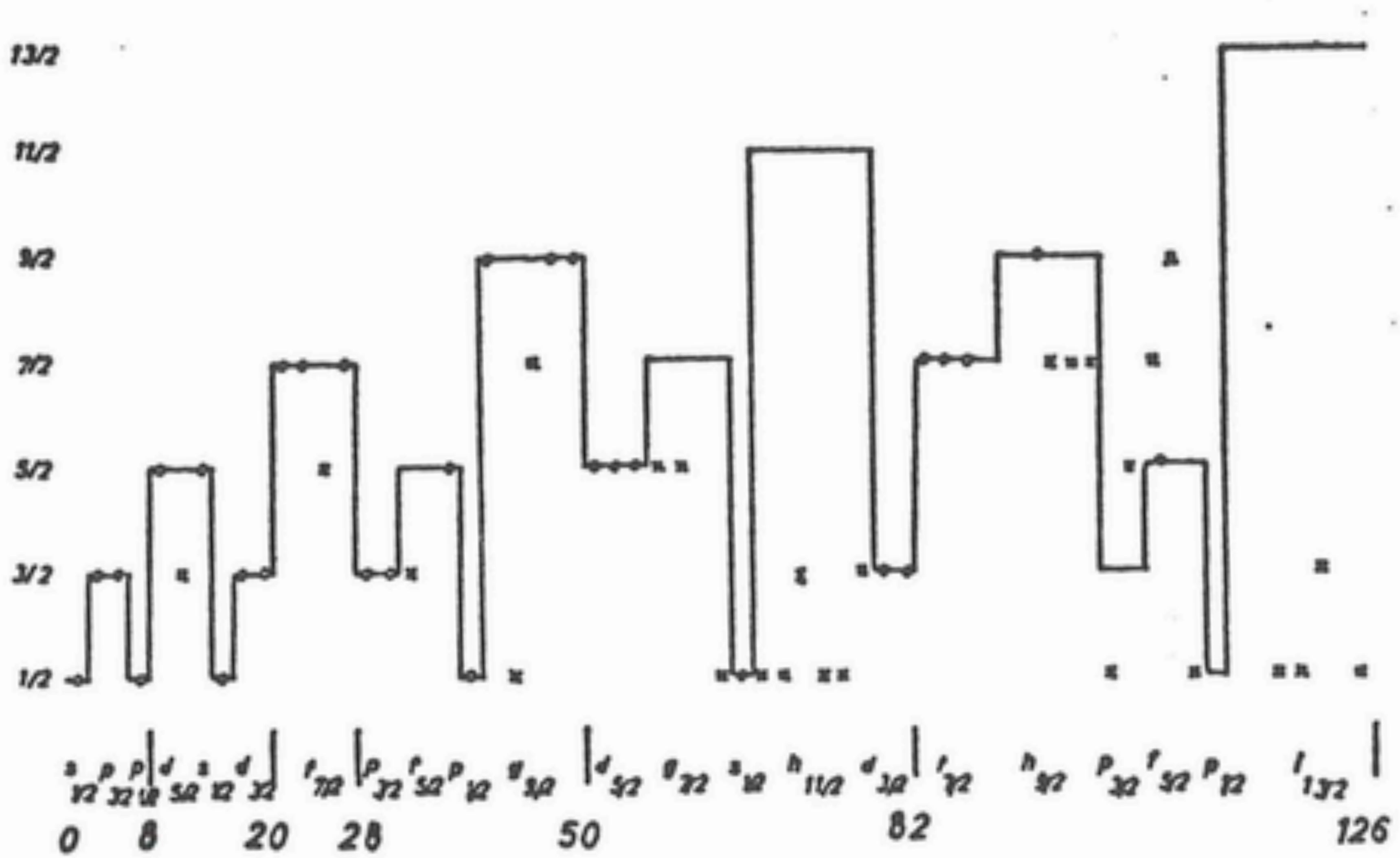

Figura 7.8 Spin dei nuclei con un numero dispari di neutroni e previsioni del modello a shell.

Modello a Shell

Momenti magnetici

numero dispari
di neutroni

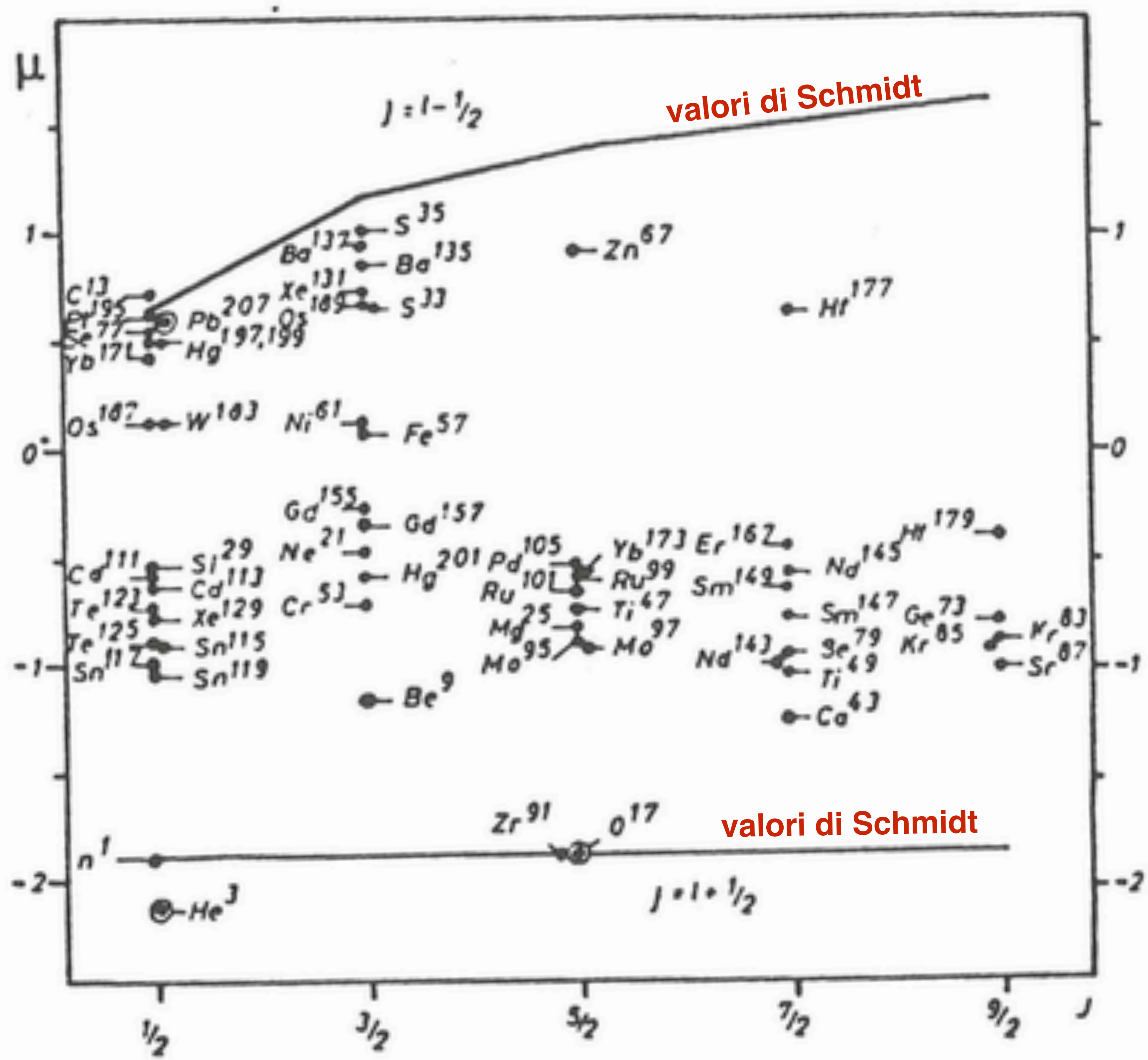

Modello a Shell

Momenti magnetici

numero dispari
di protoni

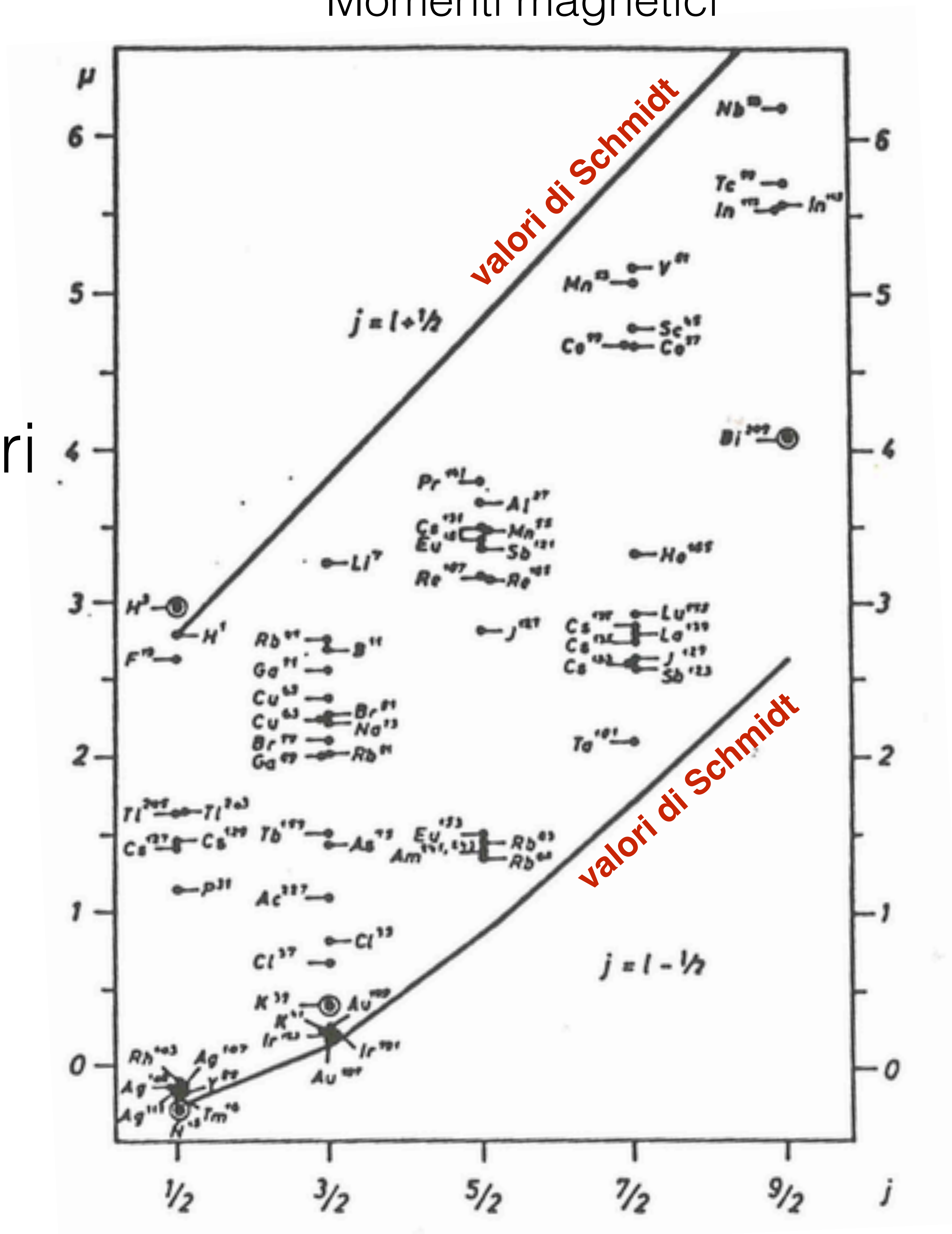

Modello a Shell

Momenti Magnetici, Spin e Parità

Nucleus	Odd nucleon type and configuration	Nuclear spin-parity	Magnetic dipole moment nuclear magnetons Calculated	Measured
^3_1H	n $(1s_{1/2})^1$	$1/2^+$	2.79	2.9788
^3_2He	p $(1s_{1/2})^1$	$1/2^+$	-1.91	−2.1276
^7_3Li	p $(1s_{1/2})^2 (1p_{3/2})^2$	$3/2^-$	3.79	3.2564
^9_4Be				−1.1776
$^{11}_5B$				2.6885
$^{11}_6C$				−1.0300
$^{13}_6C$				0.7024
$^{13}_7N$				−0.3221
$^{15}_7N$				−0.2831
$^{15}_8O$	n $(1s_{1/2})^1 (1p_{3/2})^4 (1p_{1/2})^1$	$1/2^-$	0.64	0.7189
$^{17}_8O$				−1.8937
$^{17}_9F$	p $(1s_{1/2})^1 (1p_{3/2})^4 (1p_{1/2})^2 (1d_{5/2})^1$	$5/2^+$	4.79	4.7224
$^{19}_9F$				2.6288